



NATIONAL TECHNICAL UNIVERSITY OF ATHENS

SCHOOL OF NAVAL ARCHITECTURE & MARINE ENGINEERING

DIVISION OF MARINE ENGINEERING

DIPLOMA THESIS

Anastassios Charitopoulos

Thermohydrodynamic Analysis of Thrust Bearings Using
Computational Fluid Dynamics

Examination Committee

SUPERVISOR: C.I. Papadopoulos, Assistant Professor NTUA

MEMBERS: L. Kaiktsis, Associate Professor NTUA

G. Papalambrou, Assistant Professor NTUA

Acknowledgments

First, I would like to thank my supervisor, Assist. Prof. Christos Papadopoulos, for his support during my years at NTUA. Also, I need to thank Prof. Ioannis Prousalidis and Prof. Lambros Kaiktsis, for their support and counselling whenever needed.

Special thanks go to Dr. Dimitrios Fouflias for the excellent cooperation we had over the course of almost three years.

Last but not least I would like to thank Mr. Marios Mastrokalos, Mr. Andreas Skoufis and Dr. Kostas Aivalis, for helping me through the course of my Diploma Thesis.

Abstract

Thrust bearings are vital parts of mechanical systems. The present work is concerned with the investigation of thrust bearing performance using Computational Fluid Dynamics. Recent literature results have demonstrated that different geometry patterns implemented on the surface of thrust bearings can be beneficial in terms of the main bearing performance indices, load carrying capacity and friction coefficient.

In the first part of the present study, different types of geometry patterns have been cross-evaluated, for a representative sector-pad parallel thrust bearing configuration, corresponding to: (a) an open pocket bearing, (b) a closed pocket bearing, (c) a tapered-land bearing, and (d) a bearing partially textured with rectangular dimples. Bearing performance has been computed by means of Computational Fluid Dynamics simulations based on the numerical solution of the Navier-Stokes and energy equations for incompressible non-isothermal flow. Conjugate heat transfer at the bearing pad and rotor has been taken into account. Initially, for a reference design of each bearing, the effects of varying rotational speed and minimum film thickness have been investigated. Further, characterization of each bearing for a constant level of thrust load has been performed. Finally, the effects of varying the depth of each geometry pattern have been studied. The present results illustrate a superior performance of the open pocket bearing in comparison to the other bearing types.

To assess the effects of the development of high levels of pressure on the deformations of the solid parts of a representative thrust bearing, a thermoelastohydrodynamic (TEHD) analysis has been performed for the bearing textured with rectangular dimples. Here, the CFD-based thermohydrodynamic modeling approach has been extended to account for deformations of the bearing mechanical parts. The bearing has been modelled as a sector-shaped channel, consisting of a smooth rotating wall (thrust collar) and a partially textured stationary wall (bearing pad). The bearing performance characteristics have been computed by means of numerical simulations, based on the numerical solution of the Navier-Stokes and energy equations for incompressible flow, as well as on the solution of the elasticity equations for the bearing solid parts. Here, one texture geometry has been considered, while proper thermal and structural boundary conditions have been implemented. For representative film thickness values, the effect of rotational speed and collar thickness on bearing performance is quantified, and the resulting pad and rotor deformation fields are computed. It is found that, due to oil heating, the load carrying capacity decreases with rotational speed for values higher than approximately 2000 RPM. The computed rotor deformation field is representative of a fixed support beam, characterized by substantially higher levels than those of the bearing pad. Rotor deformations increase substantially at low values of collar thickness.

The actual performance of thrust bearings may be affected significantly by manufacturing errors. Thus, to quantify such effects, a detailed study has been performed for a representative parallel slider, whose stator is textured with periodic grooves of an optimized geometry. Several types of representative manufacturing errors have been considered. In particular, discrepancies in the size and shape of the texture geometry, as well as macroscopic errors in the stator surface (concavity/convexity and waviness) have been modelled parametrically. Bearing operation has been simulated by means of the numerical solution of the Navier-Stokes equations for incompressible isothermal flow. By processing the simulation results, the effects of manufacturing errors on the bearing load carrying capacity and friction coefficient are analyzed, for representative width-to-length ratios. The effects on these global parameters are interpreted by means of pressure distributions and visualization of the flow fields. It is found that, in a number of cases, manufacturing errors result in improved performance of textured thrust bearings.

Σύνοψη

Τα ωστικά έδρανα αποτελούν σημαντικά εξαρτήματα των σύγχρονων μηχανολογικών συστημάτων. Στην παρούσα εργασία μελετώνται τα τριβολογικά χαρακτηριστικά αντιπροσωπευτικών ωστικών εδράνων με χρήση μεθόδων Υπολογιστικής Ρευστοδυναμικής. Πρόσφατες ερευνητικές εργασίες έχουν καταδείξει ότι, σε εφαρμογές ωστικών εδράνων, η χρήση τεχνητής τραχύτητας σε τμήμα της επιφάνειας του στάτορα μπορεί να οδηγήσει σε σημαντική βελτίωση της τριβολογικής απόδοσης, η οποία συνήθως ποσοτικοποιείται με βάση την ικανότητα παραλαβής φορτίου και τη ροπή τριβής.

Στο πρώτο τμήμα της παρούσας εργασίας παρουσιάζεται μια υπολογιστική μελέτη ωστικών εδράνων με διαφορετικούς τύπους τεχνητής τραχύτητας, με σκοπό τη συσχέτιση των λειτουργικών χαρακτηριστικών με τα γεωμετρικά χαρακτηριστικά των εδράνων. Συγκεκριμένα, μελετώνται και συγκρίνονται οι ακόλουθοι τύποι εδράνων: (α,β) παράλληλα έδρανα με ορθογωνική κοιλότητα, ανοικτή ή κλειστή, σε τμήμα του στάτορα, (γ) παράλληλα έδρανα με επιφανειακή τραχύτητα σε τμήμα του στάτορα, αποτελούμενη από μικρο-κοιλότητες ορθογωνικής διατομής, και (δ) έδρανα με κεκλιμένη επιφάνεια του στάτορα ως προς αυτήν του ρότορα στην περιοχή της αναρρόφησης του λιπαντικού ελαίου, και παράλληλη στην περιοχή της κατάθλιψης του λιπαντικού ελαίου (επικλινή έδρανα). Η λειτουργία των εδράνων προσομοιώνεται και αξιολογείται με χρήση μεθόδων Υπολογιστικής Ρευστοδυναμικής, βασισμένων στην αριθμητική επίλυση των εξισώσεων Navier-Stokes και ενέργειας για ασυμπίεστη μη-ισόθερμη ροή. Εδώ, λαμβάνεται υπόψη το σύνθετο φαινόμενο της σκέδασης ενέργειας προς θερμική εντός του λιπαντικού μέσου, και της μεταφοράς της στο περιβάλλον διαμέσου των τμημάτων του εδράνου (στάτορα και ρότορα). Αρχικά, για μια σχεδίαση αναφοράς του κάθε εδράνου, μελετάται η επίδραση της ταχύτητας περιστροφής του ρότορα και του ελάχιστου πάχους του λιπαντικού φιλμ στα τριβολογικά λειτουργικά χαρακτηριστικά του εδράνου. Ακολούθως, πραγματοποιείται λεπτομερής παραμετρική ανάλυση, με σκοπό την ανάδειξη της επίδρασης των κύριων παραμέτρων σχεδίασης στη λειτουργία των εδράνων. Τα παρόντα αποτελέσματα καταδεικνύουν την υπεροχή του εδράνου με ανοικτή ορθογωνική κοιλότητα έναντι των άλλων τύπων εδράνων.

Για να αξιολογηθεί η επίδραση της ανάπτυξης υψηλών πιέσεων στις επιφάνειες του εδράνου, και να προσδιοριστούν οι σχετικές παραμορφώσεις των στερεών τμημάτων του εδράνου, πραγματοποιήθηκε θερμοελαστοϋδροδυναμική (TEHD) ανάλυση για έδρανο αναφοράς με επιφανειακή τραχύτητα σε τμήμα του στάτορα, αποτελούμενη από

μικρο-κοιλότητες ορθογωνικής διατομής. Για το παρόν πρόβλημα, έγινε επέκταση του θερμοϋδροδυναμικού μοντέλου, ώστε να συμπεριληφθούν οι μηχανικές παραμορφώσεις των στερεών τμημάτων του εδράνου. Συγκεκριμένα, εκτός των εξισώσεων Navier-Stokes και ενέργειας, επιλύθηκαν αριθμητικά και οι εξισώσεις ελαστικότητας για τα στερεά τμήματα του εδράνου. Τα πεδία παραμόρφωσης στον στάτορα και στον ρότορα υπολογίστηκαν για διαφορετικές τιμές της περιστροφικής ταχύτητας του εδράνου και του ελάχιστου πάχους του λιπαντικού φιλμ. Διαπιστώθηκε ότι, λόγω της αύξησης της θερμοκρασίας, η ικανότητα παραλαβής φορτίου του εδράνου μειώνεται με αύξηση της περιστροφικής ταχύτητας του εδράνου πάνω από 2000 RPM. Διαπιστώθηκε επιπλέον ότι ο ρότορας παρουσιάζει χαρακτηριστικά παραμόρφωσης αντίστοιχα ενός προβόλου σε κάμψη, ενώ, σε απόλυτες τιμές, χαρακτηρίζεται από αρκετά μεγαλύτερες παραμορφώσεις σε σχέση με τις αντίστοιχες του στάτορα. Τέλος, επιβεβαιώθηκε ότι οι παραμορφώσεις του ρότορα αυξάνονται σημαντικά με μείωση του πάχους του.

Η τριβολογική απόδοση των ωστικών εδράνων μπορεί να επηρεαστεί σημαντικά εξαιτίας κατασκευαστικών σφαλμάτων. Για την ποσοτικοποίηση τέτοιων επιδράσεων, πραγματοποιήθηκε λεπτομερής ανάλυση για ένα τυπικό παράλληλο έδρανο με περιοδική ορθογωνική τεχνητή τραχύτητα. Εδώ, εξετάστηκαν διαφορετικοί τύποι κατασκευαστικών σφαλμάτων, συγκεκριμένα, διαφοροποιήσεις στο μέγεθος και το σχήμα της ορθογωνικής τραχύτητας, καθώς και μακροσκοπικές αποκλίσεις της επιφάνειας του στάτορα. Για αυτά τα κατασκευαστικά σφάλματα, πραγματοποιήθηκε λεπτομερής παραμετρική ανάλυση, και αξιολογήθηκε η επίδρασή τους στην ικανότητα παραλαβής φορτίου και στον συντελεστή τριβής, για διαφορετικές τιμές του λόγου μήκους - πλάτους του εδράνου. Η επίδραση των γενικών αυτών παραμέτρων αναλύθηκε, μέσω οπτικοποίησης των πεδίων ροής και πίεσης. Διαπιστώθηκε ότι, σε κάποιες περιπτώσεις, η ύπαρξη κατασκευαστικών λαθών μπορεί να βελτιώσει τα τριβολογικά χαρακτηριστικά των εδράνων με τεχνητή τραχύτητα.

Table of Contents

Acknowledgments.....	i
Abstract.....	ii
Σύνοψη	iv
Table of Contents	vi
List of Figures	viii
List of Tables	xiii
Nomenclature	xiv
1. Introduction.....	1
1.1. Bearings and applications.....	1
1.2. Literature review.....	4
1.3. Goals of present study.....	6
2. Comparison between different bearing configurations.	8
2.1. Introduction.....	8
2.2. Bearing Geometries.....	8
2.2.1 Taper-land bearing geometry	9
2.2.2 Open and closed pocket bearing geometry	10
2.2.3 Textured bearing geometry	11
2.3. Computational model	11
2.4. Computational results.....	14
2.5. Conclusions	33
3. Computational Investigation of Thermoelastohydrodynamic (TEHD) Lubrication in a Textured Sector-Pad Thrust Bearing	34
3.1. Introduction.....	34
3.2. Bearing geometry	34
3.3. Computational model	35
3.4. Computational results.....	38
3.5. Conclusions	43

4.	Effects of manufacturing errors on tribological characteristics of 3-D textured thrust bearings	44
4.1.	Introduction.....	44
4.2.	Bearing geometry	44
4.3.	Computational model	46
4.4.	Geometry parameters of optimized reference textured bearings.....	47
4.5.	Computational results.....	48
4.6.	Conclusions	67
5.	Conclusions and future study	68
6.	Literature	70

List of Figures

Figure 1. Sketch of basic stator arrangement.....	8
Figure 2. Tapered-land bearing geometry.....	9
Figure 3. Closed pocket bearing geometry.....	10
Figure 4. Open pocket bearing geometry.....	10
Figure 5. Textured bearing geometry.....	11
Figure 6. (a) Tapered-land bearing: computational grid in the fluid domain, (b) Closed pocket bearing: computational grid in the stator domain, (c) Open pocket bearing: computational grid in the stator domain, and (d) Textured bearing: details of computational grid in the fluid domain.....	13
Figure 7. Computed values of (a) load carrying capacity, (b) friction torque, (c) maximum fluid temperature, and (d) maximum pad temperature versus minimum film thickness, for the reference design of the four types of thrust bearing of the present study, at $N=1000$ RPM.....	16
Figure 8. Computed values of (a) load carrying capacity, (b) friction torque, (c) maximum fluid temperature, and (d) maximum pad temperature versus minimum film thickness, for the reference design of the four types of thrust bearing of the present study, at $N=2000$ RPM.....	17
Figure 9. Computed values of (a) load carrying capacity, (b) friction torque, (c) maximum fluid temperature, and (d) maximum pad temperature versus minimum film thickness, for the reference design of the four types of thrust bearing of the present study, at $N=4000$ RPM.....	18
Figure 10. Computed values of (a) load carrying capacity, (b) friction torque, (c) maximum fluid temperature, and (d) maximum pad temperature versus minimum film thickness, for the reference design of the four types of thrust bearing of the present study, at $N=6000$ RPM.....	19
Figure 11. Computed values of (a) load carrying capacity, (b) friction torque, (c) maximum fluid temperature, and (d) maximum pad temperature versus minimum film thickness, for the reference design of the four types of thrust bearing of the present study, at $N=8000$ RPM.....	20
Figure 12. Computed values of (a) load carrying capacity, (b) friction torque, (c) maximum fluid temperature, and (d) maximum pad temperature versus minimum film thickness, for the reference design of the four types of thrust bearing of the present study, at $N=10000$ RPM.....	21
Figure 13. Distributions of computed fields for the reference design of the four types of thrust bearings of the present study, at $N=4000$ RPM, $H_{min}=15$ μm . Left column: pressure	

	distributions on the rotor surface; middle column: temperature distributions on the stator surface; right column: temperature distributions on the bearing mid-plane. .	22
Figure 14.	Open pocket bearing: computed values of load carrying capacity versus pocket depth, for different values of minimum film thickness. The six graphs presented correspond to rotational speeds from 1000 to 10000 RPM.....	24
Figure 15.	Closed pocket bearing: computed values of load carrying capacity versus pocket depth, for different values of minimum film thickness. The six graphs presented correspond to rotational speeds from 1000 to 10000 RPM.....	25
Figure 16.	Tapered-land bearing: computed values of load carrying capacity versus taper depth, for different values of minimum film thickness. The six graphs presented correspond to rotational speeds from 1000 to 10000 RPM.....	26
Figure 17.	Textured bearing: computed values of load carrying capacity versus dimple depth, for different values of minimum film thickness. The six graphs presented correspond to rotational speeds from 1000 to 10000 RPM.....	27
Figure 18.	Distributions of computed fields for four types of thrust bearings, at $N=4000$ RPM, for a constant axial load of 2000 N. Left column: pressure distribution on the rotor surface; right column: temperature distribution on the stator surface. For each case, the values of minimum film thickness, friction torque and max. stator temperature are also included.....	29
Figure 19.	Distributions of computed fields for four types of thrust bearings, at $N=8000$ RPM, for a constant axial load of 2000 N. Left column: pressure distribution on the rotor surface; right column: temperature distribution on the stator surface. For each case, the values of minimum film thickness, friction torque and max. stator temperature are also included.....	30
Figure 20.	Distributions of computed fields for four types of thrust bearings, at $N=4000$ RPM, for a constant axial load of 4000 N. Left column: pressure distribution on the rotor surface; right column: temperature distribution on the stator surface. For each case, the values of minimum film thickness, friction torque and max. stator temperature are also included.....	31
Figure 21.	Distributions of computed fields for four types of thrust bearings, at $N=8000$ RPM, for a constant axial load of 4000 N. Left column: pressure distribution on the rotor surface; right column: temperature distribution on the stator surface. For each case, the values of minimum film thickness, friction torque and max. stator temperature are also included.....	32
Figure 22.	Geometry of computational model.....	34
Figure 23.	Sketch of the bearing of the present study and top view of the bearing pad.....	35

Figure 24. Reference case (N=4000 RPM, Hmin =15 μm, resulting in a load W=2934 N): (a) Computed pressure distribution at the fluid-rotor interface and temperature distribution at the pad surface. (b) Temperature distribution at the pad and the collar, at a vertical cross section at the mean pad radius.....	39
Figure 25. Reference case (N=4000 RPM, Hmin =15 μm, resulting in a load W=2934 N): Plots of elastic displacement at the collar and the pad domains.....	39
Figure 26. Load capacity, maximum fluid temperature and maximum rotor/pad displacement versus rotational speed, for four different values of minimum film thickness.....	40
Figure 27. Load capacity, maximum fluid temperature and maximum rotor/pad displacement versus rotor thickness, for different values of minimum film thickness.	41
Figure 28. Rotor thickness of 15 mm, N=4000 RPM: Computed pressure distribution at the fluid-rotor interface, for minimum film thickness value of (a) 5 μm, (b) 10 μm, and (c) 15 μm.	42
Figure 29. Profiles of rotor/pad displacement along (a) the circumferential, and (b) the radial direction, for different values of minimum film thickness. The corresponding locations are depicted in the left column sketches.....	42
Figure 30. (a) Three-dimensional textured converging slider geometry (parallel slider for H1=H0, diverging slider for H1<H0). (b) Geometry of dimples. (c) Typical thrust bearing application with partial texturing. (Papadopoulos et al. [4]).....	45
Figure 31. Sketch of textured sliders with manufacturing errors in the stator: (a) discrepancy in convergence ratio, (b) discrepancy in dimple depth, (c) discrepancy in dimple shape from orthogonal, (d) stator concavity, (e) stator convexity, (f) stator waviness with wavenumber n=1, and (g) stator waviness with wavenumber n=3.....	46
Figure 32. B/L = inf, k = 0: Normalized values of load carrying capacity W / Wopt and friction coefficient f / fopt for different parameters expressing manufacturing errors: (a),(f) discrepancy in convergence ratio; (b),(g) discrepancy in normalized dimple depth; (c),(h) concavity (+) / convexity (-); (d),(i) waviness; (e),(j) discrepancy from orthogonal dimple shape.	52
Figure 33. - B/L = inf, k = k_{opt} =0.75. Normalized values of load carrying capacity W / Wopt and friction coefficient f / fopt for different parameters expressing manufacturing errors: (a),(f) discrepancy in convergence ratio; (b),(g) discrepancy in normalized dimple depth; (c),(h) concavity (+) / convexity (-); (d),(i) waviness; (e),(j) discrepancy from orthogonal dimple shape.....	54
Figure 34. B/L = 1.0, k = 0. Normalized values of load carrying capacity W / Wopt and friction coefficient f / fopt for different parameters expressing manufacturing errors: (a),(f) discrepancy in convergence ratio; (b),(g) discrepancy in normalized dimple depth;	

	(c),(h) concavity (+) / convexity (-); (d),(i) waviness; (e),(j) discrepancy from orthogonal dimple shape.	56
Figure 35.	$B/L = 1.0, k = k_{opt} = 1.1$. Normalized values of load carrying capacity W / W_{opt} and friction coefficient f / f_{opt} for different parameters expressing manufacturing errors: (a),(f) discrepancy in convergence ratio; (b),(g) discrepancy in normalized dimple depth; (c),(h) concavity (+) / convexity (-); (d),(i) waviness; (e),(j) discrepancy from orthogonal dimple shape.....	58
Figure 36.	$B/L = 0.5, k = 0$. Normalized values of load carrying capacity W / W_{opt} and friction coefficient f / f_{opt} for different parameters expressing manufacturing errors: (a),(f) discrepancy in convergence ratio; (b),(g) discrepancy in normalized dimple depth; (c),(h) concavity (+) / convexity (-); (d),(i) waviness; (e),(j) discrepancy from orthogonal dimple shape.	60
Figure 37.	$B/L = 0.5, k = k_{opt} = 1.31$. Normalized values of load carrying capacity W / W_{opt} and friction coefficient f / f_{opt} for different parameters expressing manufacturing errors: (a),(f) discrepancy in convergence ratio; (b),(g) discrepancy in normalized dimple depth; (c),(h) concavity (+) / convexity (-); (d),(i) waviness; (e),(j) discrepancy from orthogonal dimple shape.....	62
Figure 38.	$B/L = \text{inf}$: Distributions of non-dimensional pressure on the moving wall, and color-coded contours of non-dimensional streamwise velocity, for: (a) a parallel bearing, and (b) a converging bearing with $k = k_{opt} = 0.75$, for nominal designs ($c=0$), convex sliders with $c=0.3$, and concave sliders with $c=0.3$	62
Figure 39.	$B/L = \text{inf}$: Distributions of non-dimensional pressure on the moving wall, and color-coded contours of non-dimensional streamwise velocity, for: (a) a parallel bearing, and (b) a converging bearing with $k = k_{opt} = 0.75$, for nominal designs ($a=0$), and wavy sliders with different wave number and non-dimensional amplitude values...	63
Figure 40.	$B/L = \text{inf}, k=0$: (a) Distributions of non-dimensional pressure on the moving wall for different values of parameters b_s and b_b . (b) Corresponding streamlines in the region of the first dimple, coded with velocity magnitude.....	63
Figure 41.	$B/L = 0.5, k = k_{opt} = 1.31$: Color-coded contours of non-dimensional pressure on the moving wall of the slider, for: (a) nominal optimal slider; (b) a concave slider with $c=0.3$; (c) a wavy slider with $n=1$ and $a=0.3$. (d) Corresponding distributions of non-dimensional pressure on the moving wall symmetry line (A-A).	64
Figure 42.	$B/L = \text{inf}$: Normalized values of load carrying capacity and friction coefficient, versus waviness phase angle, ϕ , for optimally textured sliders with: (a) $k=0$, (b) $k=0.75$	64
Figure 43.	$B/L = \text{inf}$: Distributions of non-dimensional pressure on the moving wall, and color-coded contours of non-dimensional streamwise velocity, for: (a) a parallel bearing,	

and (b) a converging bearing with $k = k_{opt} = 0.75$. Here, nominal designs ($a=0$), and wavy sliders with $a=0.2$ and different waviness phase angles, ϕ , are considered.

..... 65

List of Tables

Table 1. Parameters of optimal texture geometry reported in Papadopoulos et al. [4]: values of l_w and s , for different values of k and B/L . These values are derived for constant values of dimple number and dimple density, $N=5$ and $\rho=0.83$. For a given value of B/L , a convergence ratio of $k = k_{opt}$ corresponds to the global maximum in load carrying capacity.....	48
---	----

Nomenclature

A	Pad area (m ²)
A_w	Waviness amplitude (m)
B_a	Bottom left length of dimple (m)
B_b	Bottom right length of dimple (m)
B_d	Dimple width (mm)
D_i	Inner pad diameter (mm)
D_m	Mean diameter (mm)
D_o	Outer pad diameter (mm)
D_{st}	Stiffness matrix
F_f	Friction force (N)
F_p	Vertical pressure force (Pa)
H_0	Outlet height (mm)
H_1	Inlet height (mm)
H_d	Texture depth (μm)
H_g	Groove depth (mm)
H_{min}	Minimum film thickness (μm)
L_c	Texture cell length (m) $L_c = L(1 - l_{ui} - l_{uo}) / (N + \rho_T - 1)$
L_d	Dimple length (mm,m)
L_g	Groove length (mm)
L_{tap}	Taper length (mm)
L_{ui}	Untextured inlet length (mm)
L_{uo}	Untextured outlet length (mm)
M_t	Friction torque (Nm)
N_p	Number of pads
P_r	Prandtl number
W^*	Non-dimensional load carrying capacity $W^* = W / \mu UB (H_{min} / L)^2$
a_{conv}	Convention coefficient (W/m ² .K)
a^{se}	Coefficient of thermal expansion
a_w	Non-dimensional waviness amplitude $a_w = A_w / H_{min}$
b_a	Non-dimensional bottom left length of dimple $b_a = B_a / L_d$

b_b	Non-dimensional bottom right length of dimple $b_b = B_b / (L_d - B_a)$
c_p	Specific heat capacity (J/kg.K)
l_{ui}	Non-dimensional untextured inlet length $l_{ui} = L_{ui} / H_{min}$
l_{uo}	Non-dimensional untextured outlet length $l_{uo} = L_{uo} / H_{min}$
p^*	Non-dimensional pressure $p^* = p / \rho U^2 \cdot Re \cdot H_{min} / L$
x^*	Non-dimensional x coordinate $x^* = x / L$
ε^{el}	Elastic strain
ε^{th}	Thermal strain
λ_f	Oil thermal conductivity (W/m.K)
λ_{sp}	Pad thermal conductivity (W/m.K)
λ_{sr}	Rotor thermal conductivity (W/m.K)
ρ_T	Texture density $\rho_T = L_d / L_c$
σ^{el}	Elastic stress (Pa)
ϕ_w	Waviness phase angle (deg)
B	Slider width
C	Concavity/convexity amplitude (m)
E	Young's modulus (Pa)
G	Shear modulus (Pa)
H	Film thickness (μm)
L	Pad length at bearing mid-sector (mm)
N	Rotational speed (RPM)
Re	Reynolds number
T	Temperature (K)
U	Rotor speed at pad mid-sector (m/s)
V	Fluid velocity vector
W	Bearing load capacity (N)
c	Non-dimensional concavity/convexity amplitude $c = C / A_{min}$
f	Friction coefficient $f = F_{fr} / W$
k	Convergence ratio $k = (H_1 - H_0) / H_0$
l	Non-dimensional slider length $l = L / H_{min}$
n	Wave number
p	Pressure (Pa)

r	Radial coordinate (mm)
s	Relative dimple depth $s = H_d / H_{min}$
ν	Kinematic viscosity (m ² /s)
ε	Total strain
μ	Fluid dynamic viscosity (Pa.s)
ρ	Fluid density (kg/m ³)
τ	Shear stress (Pa)
ω	Rotor angular velocity (rad/s)

1. Introduction

1.1. Bearings and applications

Bearings are mechanical components used in almost every application associated with moving parts. According to Hamrock [1] “a bearing is a support or guide that locates one machine component with respect to others in such a way that prescribed relative motion can occur while forces associated with machine operation are transmitted smoothly and efficiently”.

There are many kinds of bearings. They have commonly been categorized with respect to their working principles. The main categories are (i) rolling element bearings, (ii) hydrodynamic bearings, and (iii) hydrostatic bearings. Bearing with different working principles such as magnetic bearings, foil bearings, or hybrid bearings, which combine different working principles, do also exist, and are used in specialized applications.

Tribology is the scientific field confronted with the study of friction, wear and lubrication in frictional pairs. Friction is an endogenous problem of all bearings. Solutions of tribological problems quantifying performance parameters and improving design have been of central importance for engineers. The rise of computational power and the improvement of available Computational Fluid Dynamics (CFD) codes has allowed detailed investigation of complex bearing problems and design optimization. Friction between the moving parts of mechanical components leads to heat generation and power loss. A mild estimation is that one third of the global energy consumption is spent in an attempt to overcome friction in the various forms that it occurs. A substantial reduction of friction losses (e.g. by 20%-40%) would have an economic impact of utmost significance, and an environmental impact corresponding to a reduction in CO₂ emissions per year measured in billions of tons. In industry, there are countless applications which involve moving parts with surfaces in close proximity to each other, varying in scale from tiny micro-turbines to enormous mechanical systems as hydro-generators.

In marine applications, friction plays a decisive role in the overall ship performance. Apart from the hydrodynamic friction losses of the ship hull, a significant percentage of the fuel power is expended due to friction within the main and auxiliary engines and in the propulsion shafting system, totaling approximately 6%-10% of the engine break horse power (BHP).

The three main categories of bearings are briefly presented hereinafter.

Rolling element bearings

These bearings consist of two racers which roll over each other with the aid of several rolling elements, which keep the surfaces of the racers separated. The rolling elements can have spherical, cylindrical, barrel or conical shape. Radial or axial forces are transferred from one to

the other racer through the rolling elements; in general, very small friction forces are exhibited in the roller-racer interfaces.

Rolling element bearings can be very efficient in almost every small and medium scale application. Apart from very low values of friction losses, they also provide good dynamic behavior, whereas their mass production leads to a low acquisition cost. However, in more demanding, heavy-duty, applications, rolling element bearings are usually not selected, because of their large size and increased cost. In specialized designs, the cost of rolling element bearings increases rapidly, whereas their life-span is smaller in comparison to that of hydrodynamic and hydrostatic bearings. Also, rolling element bearings usually do not prove functional after occurrence of damage, whereas repair costs are usually prohibitive.

Hydrodynamic bearings

In hydrodynamic bearings, the bearing rotor and stator are separated by a thin film of lubricating oil. In particular, when a relative motion between the two racers is imposed, the lubricant that is present in the clearance between the bearing rotor and stator acquires motion from the moving part, and is forced to enter a wedge geometry, which gives rise to pressure build-up. Pressurized oil keeps the surfaces of the rotor and the stator separated, minimizing friction losses and wear. This oil wedge is central to the phenomenon of hydrodynamic lubrication; bearing operation is strongly dependent on wedge geometry and physical properties of the lubricant film.

- i. The minimum distance between the rotor and the stator is defined as the **minimum film thickness** (H_{min}):
 - For a given bearing geometry, increased loads lead to decreased values of H_{min} (leading to a steeper wedge geometry).
 - Pressure in the lubricant domain attains a maximum value in the vicinity of the region corresponding to H_{min} , whereas low pressure values are typically attained in the region of maximum oil film thickness.
- ii. **Load carrying capacity** of a bearing (W) is the force corresponding to the integral of oil pressure over the surface of the bearing rotor. For given bearing dimensions and oil properties, bearing designs exhibiting increased load carrying capacity for a given value of H_{min} are favorable. Generally, bearing designers are confronted with designing bearings that maximize load carrying capacity for given values of H_{min} .
- iii. **Friction force** of a bearing (F) is the force corresponding to the integral of oil shear stress over the surface of the bearing rotor. Friction coefficient (f) is defined as the ratio of friction force to load carrying capacity, and is a typical metric of bearing performance.

- iv. The **dynamic viscosity** of the lubricant (μ) is of utmost importance regarding bearing performance. For given bearing dimensions and external load, utilization of a more viscous fluid leads to increased values of H_{min} , but also of friction force.
- v. An important parameter regarding bearing performance is the **relative speed** of the bearing rotor and stator. For given bearing geometry and load, increase in relative speed leads to a steeper pressure build-up in the lubricant domain, and to an increased value of H_{min} . However, as relative speed increases further, viscous dissipation in the fluid domain becomes dominant, i.e. thermal energy in the lubricant domain generated due to shear forces leads to a substantial increase of oil temperature, which, in turn, substantially decreases the value of oil viscosity. Therefore, the initial increase of minimum film thickness with increasing relative speed can be followed by a gradual decrease at higher values of relative speed.

Hydrodynamic bearings are used in numerous applications, offering stable performance and design simplicity. A main disadvantage of hydrodynamic bearings is their poor behavior during start-up and shut-down, where mixed lubrication conditions prevail, leading to increased friction forces and surface wear. In marine applications, hydrodynamic journal and thrust bearings are commonly utilized in the propulsion shafting system, providing excellent static and dynamic properties, durability and reliability.

Hydrostatic bearings

In hydrostatic bearings, an external supply of pressurized oil is continuously feeding the clearance between the stator and the rotor with lubricant, through appropriate supply holes at the bearing stator. The pressurized lubricant separates the two surfaces; a thick fluid film can be sustained even without relative motion between the rotor and stator. Thus, hydrostatic bearings exhibit extremely low friction characteristics during start-up and shut-down, making them excellent candidates for applications where frequent start-ups and shut-downs are required. This technology is practically wear-free and high-precision, since external pressure can be used to stabilize the rotor by controlling the minimum film thickness of the lubricant. On the other hand, the construction and operational costs of hydrostatic bearings are higher in comparison to those of hydrodynamic bearings, and thus their use is quite limited. Hybrid bearing designs, combining hydrostatic lift during start-up and hydrodynamic lubrication at normal operation are used in several applications (e.g. in hydro-power systems, to support the axial loads) to exploit the positive characteristics of both designs.

1.2. Literature review

Thrust bearings are important components of industrial and propulsion applications. Over the past years, extensive research activity has aimed at improving the performance of thrust bearings, quantified in terms of the load carrying capacity and the friction coefficient.

In several of these studies, improvement of thrust bearing performance has been attempted by implementing texture patterns on the stator surface. In particular, studies [2]-[7] have considered rectangular texture patterns, and have demonstrated the potential of improving bearing performance over that of simple smooth converging sliders. This improvement is, evidently, maximized in the limit of parallel textured bearings. Currently, CFD thermohydrodynamic studies can account for heat transfer effects in complex geometry applications. In particular, detailed simulations reported in [8] have quantified the effects of oil heating on the performance of a parallel thrust bearing textured with rectangular dimples, and representative cases have demonstrated a good agreement against corresponding experiments [9].

Other studies have investigated the effects of texture design, within the frame of a general texture pattern, on temperature levels, and thus bearing performance. In [10], it was shown that, in a parallel thrust bearing textured with rectangular dimples, a sufficiently high texture density (higher than approximately 50%) is necessary to maintain a proper (low) level of oil temperature. Further, the same study has shown that a proper positioning of the dimples, in particular placing the first row immediately after the entrance groove, reduces temperature, thus affecting positively bearing performance, an effect also reported in the computational study of [11]. A similar conclusion is arrived at in the analytical study of [12], which concerns a centrally pivoted slider with one groove on its stator. The results of [12] demonstrate that bearing performance improves for positions of the groove approaching the slider entrance. In [13], the potential of non-conventional texture patterns, in particular of a large elliptical recess, in improving bearing performance was demonstrated. In [14], the effect of groove depth was studied in the frame of a model geometry characterized by a stator with one groove; an improving effect of increasing the dimple depth of a properly placed dimple on the friction coefficient was demonstrated. For small values of convergence ratio, this was due to the increased levels of load capacity, while for high convergence ratios due to a reduction of shear stresses. In the experimental study of [15], the performance of a textured unidirectional (texture placed adjacent to the leading edge) parallel thrust bearing was compared to that of a corresponding bi-directional one (with two equal textured parts on each of the pad ends); the superiority of the unidirectional bearing, in terms of the friction coefficient, was demonstrated. The potential of texture patterns in improving the performance of different tribological applications is illustrated in [16].

Textured bearings can be characterized by a large number of small geometry recesses or by a small number of large geometry recesses. In the limit of one large recess, a pocket bearing is obtained. A computational study of the effects of positioning the recess region on the stator surface is reported in [17], and results are compared against a reference case of a smooth converging bearing. It is shown that the effects of the recess are in general positive, however performance may deteriorate in the limit of high oil viscosity and bearing speed. In [18], a 3-D computational study of an open pocket parallel bearing (rectangular groove adjacent to the leading edge) is presented, based on the solution of the Reynolds and energy equations. The results demonstrate that performance is comparable to that of smooth converging sliders.

Tapered-land thrust bearings appear as an attractive alternative of thrust bearing design, due to their relative simple geometry pattern. The potential of tapered-land bearings is demonstrated in the experimental study of [19], which includes a detailed investigation of the effects of rotational speed and thrust load on oil temperature. The trends in [19] were justified in the computational study presented in [20], in which it was also demonstrated that approximately 80 to 90% of the dissipation power is convected out by the oil flow, and the rest is transferred through the solid interfaces.

New concepts related to sliders capable of operating in environments other than lubricating oils, under severe loading conditions corresponding to elasto-hydrodynamic operation, have been recently analyzed, mainly in terms of parametric computational studies [25]-[29].

Under high loading, a revisit of common assumptions regarding bearing heat transfer (and corresponding boundary conditions implemented in simulations) may be essential. In this context, the combined experimental and theoretical investigation in [20] has shown that, in a highly loaded thrust bearing, over 80% of the internal heat generation due to friction is removed by the oil itself, and the rest is transferred through the solids, which is in overall agreement with previous estimates of [30]. Further, the effects of solid deformation on bearing performance may also be essential. For a highly loaded fixed geometry thrust bearing, these effects were investigated in the computational study of Ahmed et al. [31]. The results of the TEHD study reported in [31] show that, for low values of rotor thickness and high rotational speeds, a high mechanical deformation of the runner is attained, resulting in a substantial reduction of film thickness in the inner radius regime, of order 60%. This results in significant differences in the values of global bearing parameters (load capacity, friction coefficient), in comparison to those of the thermohydrodynamic (THD) analysis. In another TEHD [32] study concerning a fixed-geometry thrust bearing, it was shown that performance indices are affected mainly by the pad thermal deformation, and, to a lower extent, by the pad mechanical deformation.

Although mechanical and thermal deformations change the designed fluid film geometry, in untextured bearings, manufacturing errors of the bearing surface, such as waviness, tilt, concavity or convexity, are known to also affect bearing performance (load-carrying capacity and friction coefficient), see e.g., [34], [46], and [47]. In particular, bearings with convex or waved pad surface may, in certain cases, be characterized by improved performance, in comparison to that of flat surface bearings [34].

Detailed analyses of the effects of manufacturing errors have been reported in the recent literature for aerostatic bearings. This type of bearings provides full performance at zero speed, increased positioning accuracy, and practically frictionless operation. Aerostatic bearings are widely used in metrology, in ultra-precision machining and in coordinate measuring machines. The effect of manufacturing errors on Pareto optimal flat pad aerostatic bearing designs has been investigated in [36]; their results show that multi-orifice aerostatic flat pad bearings are highly sensitive to surface profile variations. The study [38] presented a design methodology for externally pressurized journal bearings, which includes issues related to manufacturing and the specification of tolerances.

The sensitivity of journal bearing performance to deviations from the ideal cylindrical surface is demonstrated in the combined experimental-theoretical work of Stout and Pink [48]. Further, in [41], the effects of manufacturing errors on a single type of multi-orifice rectangular flat pad aerostatic bearings are considered; it was found that deviations of the bearing surface from the ideal plane had a significant effect on bearing load capacity and stiffness coefficient. In [42] the influence of the geometrical parameters of a pocketed type orifice restrictor on the performance of an aerostatic thrust bearing is studied. For a similar bearing geometry [39] the effects of the recess shape, orifice diameter and gas film thickness, on performance parameters are investigated. Sharma and Pandey [25] compared the performance of surface profiled hydrodynamic thrust bearings to that of conventional plane thrust bearings; they showed that an increase in load carrying capacity of approximately 30% can be achieved by proper surface profile selection.

1.3. Goals of present study

Following previous literature studies, the present work attempts a cross-evaluation of different types of thrust bearings, in particular an open- and a closed pocket bearing, a tapered-land bearing and a representative textured one (with rectangular dimples), of the same principal dimensions. Bearing performance is computed by solving the Navier-Stokes and energy equations, for representative values of rotational speed and film thickness. Further, variations of geometry pattern depth, as well as operation at constant load levels, are considered.

Furthermore, recent studies have shown that both thermal and mechanical deformation of a bearing stator and rotor may significantly affect its performance. The present study includes a first

investigation accounting for the effects of mechanical deformation, for the case of a complex thrust bearing textured with square dimples. The present work follows the recent THD study of Papadopoulos et al. [9], extending it by considering solid deformations. The texture configuration considered here is planned to be tested experimentally at the University of Poitiers. Thus, a goal of the present computations is to guide the experiments currently under preparation.

Finally, following the work of Papadopoulos et al. [4], in the present study the effects of manufacturing errors in textured thrust bearings are investigated. Here, 3-D thrust bearings of different width-to-length and convergence ratios, with optimal texturing patterns, are considered. A parametric CAD model is utilized, accounting for different types of manufacturing errors of the stator, in particular convergence ratio value, convexity / concavity, waviness, and dimensioning and shape of the texture cell pattern. Computational Fluid Dynamics simulations (CFD) simulations are performed, in which the thrust bearings are modelled as 3-D micro-channels with a moving and a stationary wall. Processing of the simulation results yields the bearing performance parameters. The results demonstrate that manufacturing errors may, in several cases, lead to improved bearing performance.

2. Comparison between different bearing configurations.

2.1. Introduction

Extensive research activity has been recently reported aiming at improving the performance of thrust bearings. In order to reduce friction forces and to increase load carrying capacity, different pad geometries have been introduced. In this chapter, four bearing designs, in particular an open and a closed pocket bearing, a tapered-land bearing and a representative textured one (with rectangular dimples), of the same principal dimensions, are studied.

2.2. Bearing Geometries

The thrust bearing configurations investigated here comprise eight pads (see Figure 1). The basic configuration and dimensions of Figure 1 are maintained for all four bearings of the present study, namely: a tapered-land bearing, a closed pocket bearing, an open pocket bearing and a bearing partially textured with square dimples. Each pad is constrained between two grooves. The oil convects from the leading edge to the trailing edge of the pad, and builds up pressure due to either the wedge effect (tapered-land bearing) or the presence of the pocket/dimples. The inner pad diameter is $D_i = 50\text{mm}$ and the outer diameter is $D_o = 90\text{mm}$. The pad and the rotor thickness are 10 and 20 mm, respectively. The length of the groove is $L_g = 3\text{mm}$ and the depth of the groove is $h_g = 4\text{mm}$. For all bearings, the rotor is planar and smooth.

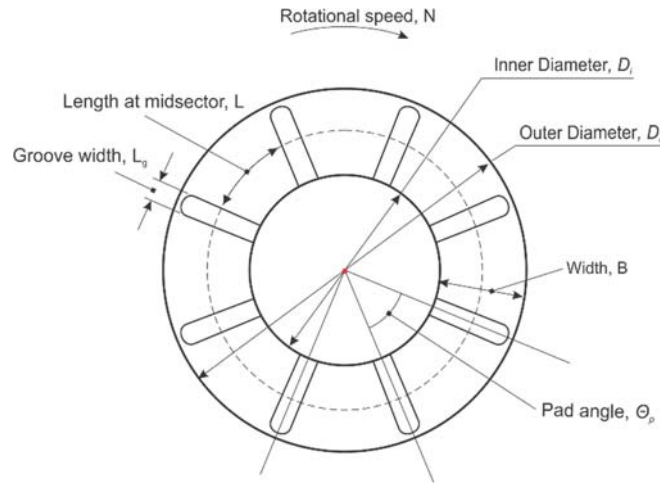


Figure 1. Sketch of basic stator arrangement.

2.2.1 Taper-land bearing geometry

The tapered-land bearing, illustrated in Figure 2, is characterized by a taper length of $L_{tap} = 15mm$. Here, values of minimum film thickness from 10 to 80 μm are considered, with a taper (wedge) depth from 10 to 100 μm .

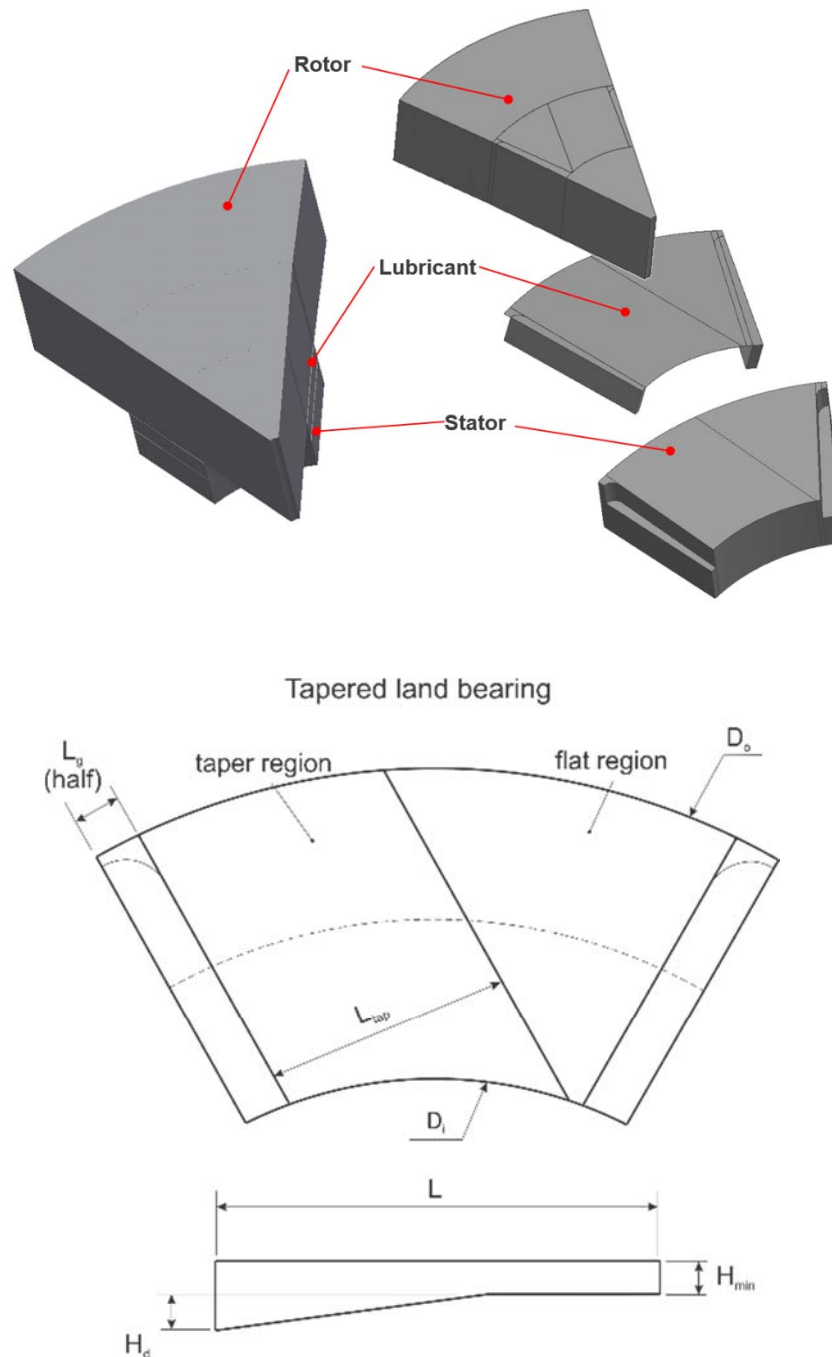


Figure 2. Tapered-land bearing geometry.

2.2.2 Open and closed pocket bearing geometry

The closed pocket and the open pocket bearings (figures 3 and 4, respectively) contain a stator pocket whose depth is varied, getting values from 10 to 100 μm . The minimum film thickness values considered range from 10 to 80 μm . The inner and outer pocket diameters are 55 mm and 85 mm, respectively, with the pocket extending in the circumferential direction: (a) for the closed pocket bearing, from 1 mm after the leading edge up to an angle of 29° ; for the open pocket bearing, from the leading edge up to an angle of 29° .

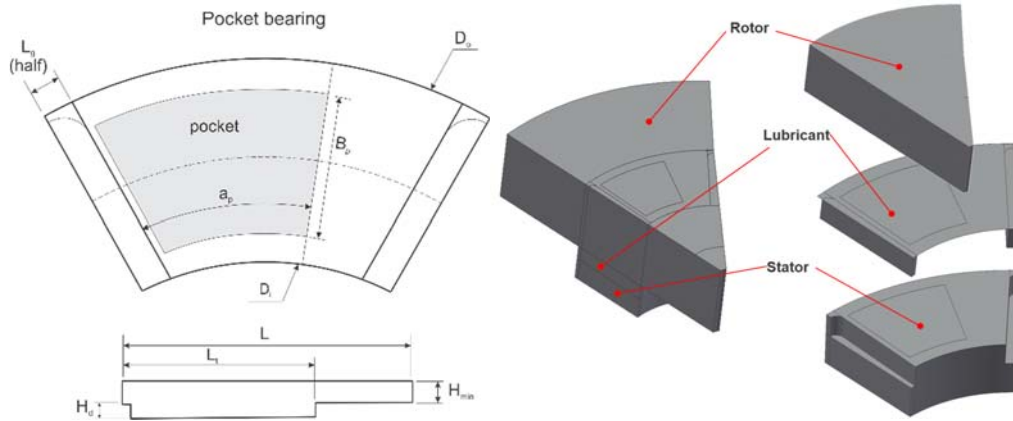


Figure 3. Closed pocket bearing geometry

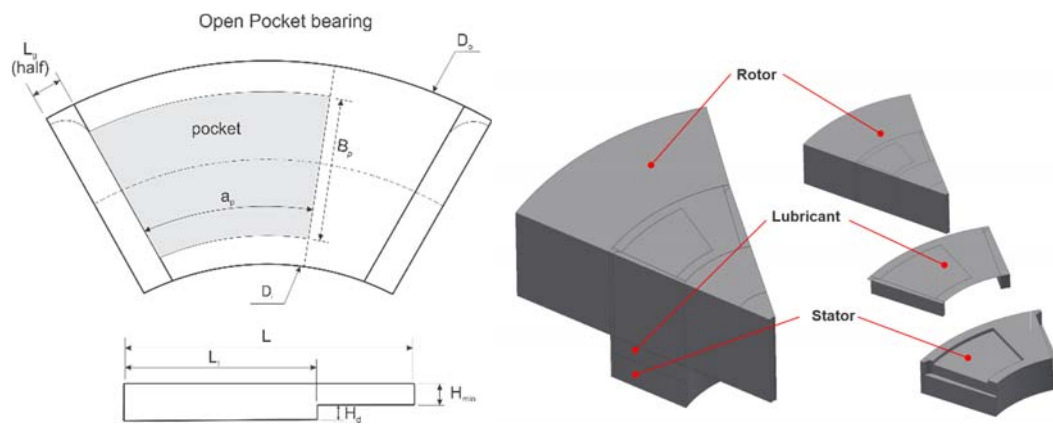


Figure 4. Open pocket bearing geometry

2.2.3 Textured bearing geometry

The textured bearing (see Figure 5) contains textured cells of side $a = 1\text{mm}$; each cell contains a square dimple, of a side of 0.75mm , thus resulting in a texture density (texture area to cell area) of 0.5625 . Dimples have a depth of $H_d = 20\mu\text{m}$, and extend from the leading groove edge up to an angle of 29° . In the radial direction, the texture is symmetric with respect to the pad mid-sector, with a width of 15mm .

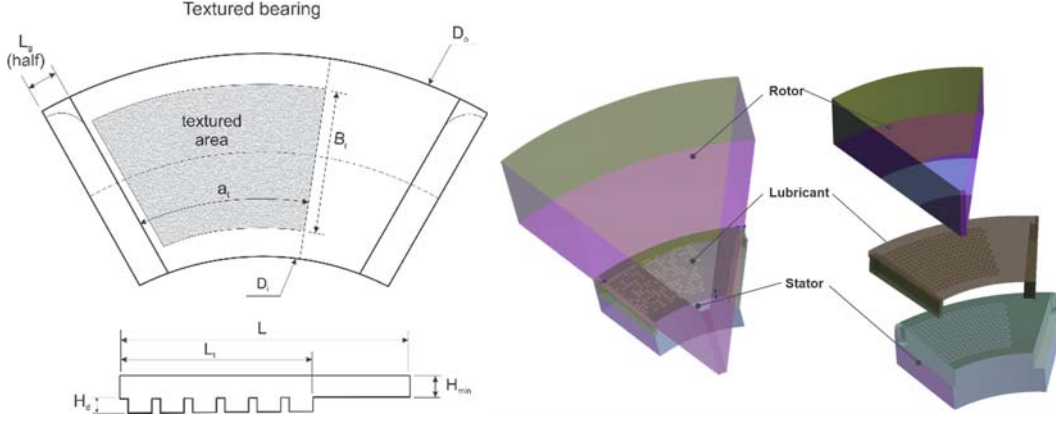


Figure 5. Textured bearing geometry

2.3. Computational model

In the present study, CFD modeling is utilized to solve (a) for the flow field of the lubricant, taking into account thermal effects, and (b) for the temperature field of the bearing pad and rotor. The lubricant pressure is considered to be higher than vapor pressure, i.e. cavitation effects are not accounted for. The computational domain includes a single pad, the corresponding part of the collar, and the lubricant confined between the pad and the collar. Half of the fore- and half of the aft- groove volume is also considered. The conservation equations are:

Mass conservation equation:

$$\nabla \cdot \mathbf{V} = 0 \quad (1)$$

Momentum equation:

$$\rho(\mathbf{V} \cdot \nabla)\mathbf{V} = -\nabla p + \nabla \cdot (\mu \nabla \mathbf{V}) \quad (2)$$

Energy equation, for the fluid domain:

$$\rho C_p \mathbf{V} \Delta T = \nabla \cdot (\lambda_f \nabla T) - \tau : \nabla \mathbf{V} \quad (3)$$

Energy equation, for the solid domain:

$$\nabla \cdot (\lambda_s \nabla T) = 0 \quad (4)$$

The lubrication oil of the present study is ISO VG 46, characterized by a density of 870 kg/m³; a temperature dependent viscosity is considered, given by the McCoull and Walther relation [20]:

$$\log(\log(\mu / \rho + a)) = n - m \log(T) \quad (5)$$

where, ν is the kinematic viscosity (cSt), $a = 0.6$, $m = 3.52681$, $n = 9.02865$, V is the velocity vector (m/s), p the static pressure (Pa), T the temperature (K), τ , the viscous stress tensor, ρ the oil density (kg/m³), μ the oil dynamic viscosity (kg/m.s), c_p the oil specific heat capacity (J/kg.K), λ_f the oil thermal conductivity (W/m.K), λ_{sp} the pad thermal conductivity (W/m.K) and λ_{sr} the rotor thermal conductivity (W/m.K).

The flow Reynolds number is defined at the mid-sector of the bearing based on the minimum film thickness, H_{min} , and the rotor wall circumferential velocity $U = \omega D_m / 2$, by the following equation: $Re = \rho U H_{min} / \mu$. In the present study, typical values range from 1 to 110. Further, the dynamics depends on the oil Prandtl number, $Pr = \mu C_p / \lambda_f$ depending on local temperature. For all cases considered, the flow is laminar.

Spatial discretization and boundary conditions

Typical 3-D finite volume meshes generated for the fluid and the solid domain involved approximately 6×10^5 hexahedral cells. In the bearing regions away from the textured/pocketed/tapered geometry, a minimum of 14 cells was used in the cross flow direction. Representative meshes generated for the different bearing types of the present study are presented in Figure 6(a)-(d).

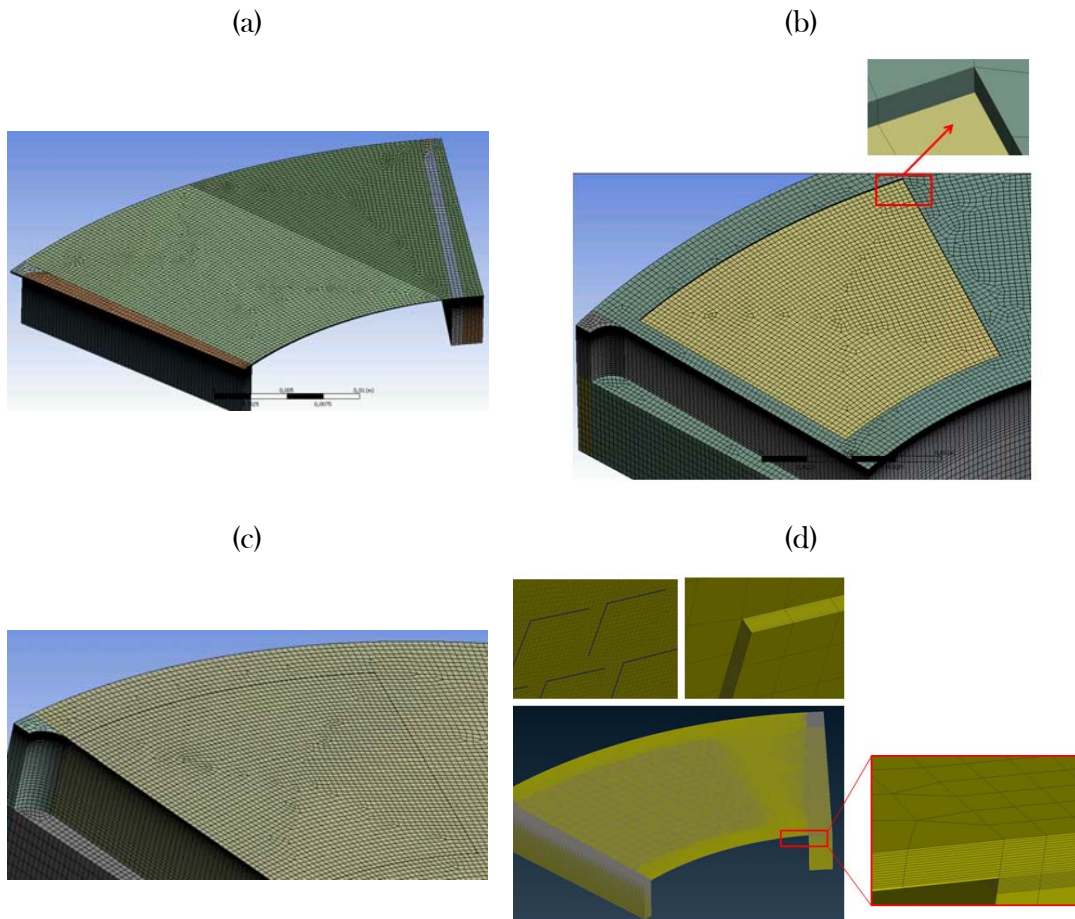


Figure 6. (a) Tapered-land bearing: computational grid in the fluid domain, (b) Closed pocket bearing: computational grid in the stator domain, (c) Open pocket bearing: computational grid in the stator domain, and (d) Textured bearing: details of computational grid in the fluid domain

Different meshes were created, with finite volume numbers both lower and significantly higher than the typical meshes used for the computations reported subsequently; the relative differences in terms of load capacity, friction torque and maximum pad temperature between typical and very fine meshes were of the order of 1%-2%.

All walls are considered impermeable, with the no-slip condition applied. The rotor is moving at a constant angular velocity ω , giving a circumferential local velocity $U = \omega \cdot r$, where r is the local radius.

The inlet fluid surface of a bearing is considered as opening. The oil feeding pressure and temperature are assumed to be constant at 1 bar (above the atmospheric) and 40°C, respectively. A Neumann boundary condition is assumed for the velocity. The outer fluid surface of the bearing is considered as pressure outlet, with a fixed value of 0 bar (relative to the atmospheric); a Neumann boundary condition is considered for the velocity and temperature, while no inflow

is permitted. Rotational periodicity is implemented for corresponding points of the inflow and outflow areas of the bearing pad.

In the fluid-pad and fluid-rotor interfaces, continuity of temperature and heat flux is implemented. At the remaining bearing external surfaces, the following values of convection coefficient, a_{Conv} , and ambient temperature, T_{amb} , have been considered:

- Pad inner surface: $a_{Conv} = 200(W/m^2 \cdot K)$, $T_{amb} = 40^{\circ}C$
- Pad outer surface: $a_{Conv} = 25(W/m^2 \cdot K)$, $T_{amb} = 40^{\circ}C$
- Pad bottom: $a_{Conv} = 1000(W/m^2 \cdot K)$, $T_{amb} = 40^{\circ}C$ (equivalent convection parameters accounting for the thermal resistance of the steel support)
- Pad leading/trailing surfaces: $a_{Conv} = 200(W/m^2 \cdot K)$, $T_{amb} = 40^{\circ}C$ (assumed convection with lubricating oil in the groove area)
- Rotor outer surface: $a_{Conv} = 25(W/m^2 \cdot K)$, $T_{amb} = 20^{\circ}C$
- Rotor top surface: $a_{Conv} = 25(W/m^2 \cdot K)$, $T_{amb} = 20^{\circ}C$

The vertical load, W , and the friction torque, M_t , exerted on the rotor surface are calculated as follows:

Vertical load, W :

$$W = F_p = N_p \int_A p \, dA \quad (6)$$

Friction torque, M_t :

$$M_t = N_p \int_A t_{\theta} r \, dA \quad (7)$$

Where τ_{θ} is the shear stress at the film/runner interface in the circumferential direction.

2.4. Computational results

Variation of Operating Conditions: Rotational Speed and Minimum Film Thickness Variation

In Figure 8 - Figure 13, the bearing load capacity, friction torque, maximum fluid temperature and maximum pad temperature are presented as functions of minimum film thickness, for the reference design of the four types of thrust bearing of the present study. In particular, the geometry of the bearings is characterized by a taper/pocket/dimple depth, H_d , of 20 μm , a pocket/texture circumferential extend angle of 29° and a taper width of 15 mm. In all cases, an increase of load capacity, friction torque and temperature levels at decreasing film thickness is verified. Qualitatively, the increase in bearing load capacity appears to be a quadratic function of

the inverse of minimum film thickness. The open pocket bearing exhibits a behavior which is superior to all other types in terms of the load capacity, in the entire operational range, especially at low values of minimum film thickness (high thrust loads), and low values of rotational speed. At increasing values of rotational speed (above 4000 RPM), the performance of the tapered-land thrust bearing is substantially improved, reaching, at high thrust loads, the performance of the open pocket bearing. At higher values of minimum film thickness (lower thrust loads), the four bearing types have similar performance characteristics. In general, the textured bearing is characterized by a lower value of friction torque (in comparison to the other bearing types); at low loads, this yields an improved value of friction coefficient.

As illustrated in Figure 8 - Figure 13, at low values of minimum film thickness, the closed pocket bearing is characterized by substantially lower levels of load capacity, in comparison to the open pocket bearing. In particular, the decrease in load capacity is approximately 30% at low rotational speeds, reaching 50% at 10000 RPM. This decrease should be mainly attributed to the decreased circumferential oil mass flow of the closed pocket bearing configuration (due to the geometric restriction at the entrance), which leads to a substantial increase of oil temperature and a corresponding decrease of oil viscosity.

Also Figure 8 - Figure 13 demonstrate that textured bearings behave sufficiently well at high loads and low values of rotational speed, with reference to the closed pocket and the tapered land bearings. However, the performance of the textured bearing deteriorates in the limit of high speeds, and this is associated with an increase in temperature levels, which is substantially higher in comparison to all other bearing types.

In more detail, the computed fields are visualized in Figure 14, for a representative case characterized by $N=4000$ RPM and $H_{min}=15$ μm . Here, the pressure field, the temperature distribution on the stator surface, as well as the temperature field on the bearing mid-plane are presented. The gradual pressure build-up, the oil heating, as well as the effective cooling of the stator and the rotor, are evident. For all cases, it is shown that, in the streamwise direction, the maximum in pressure is attained at the pocket/taper/texture end. In the closed pocket bearing, a small sub-ambient pressure regime is present at the pocket entrance region. In all cases, the maximum pad temperature is, attained downstream, at the bearing outer radius region, due to the combined effects of convection and centrifugal forces.

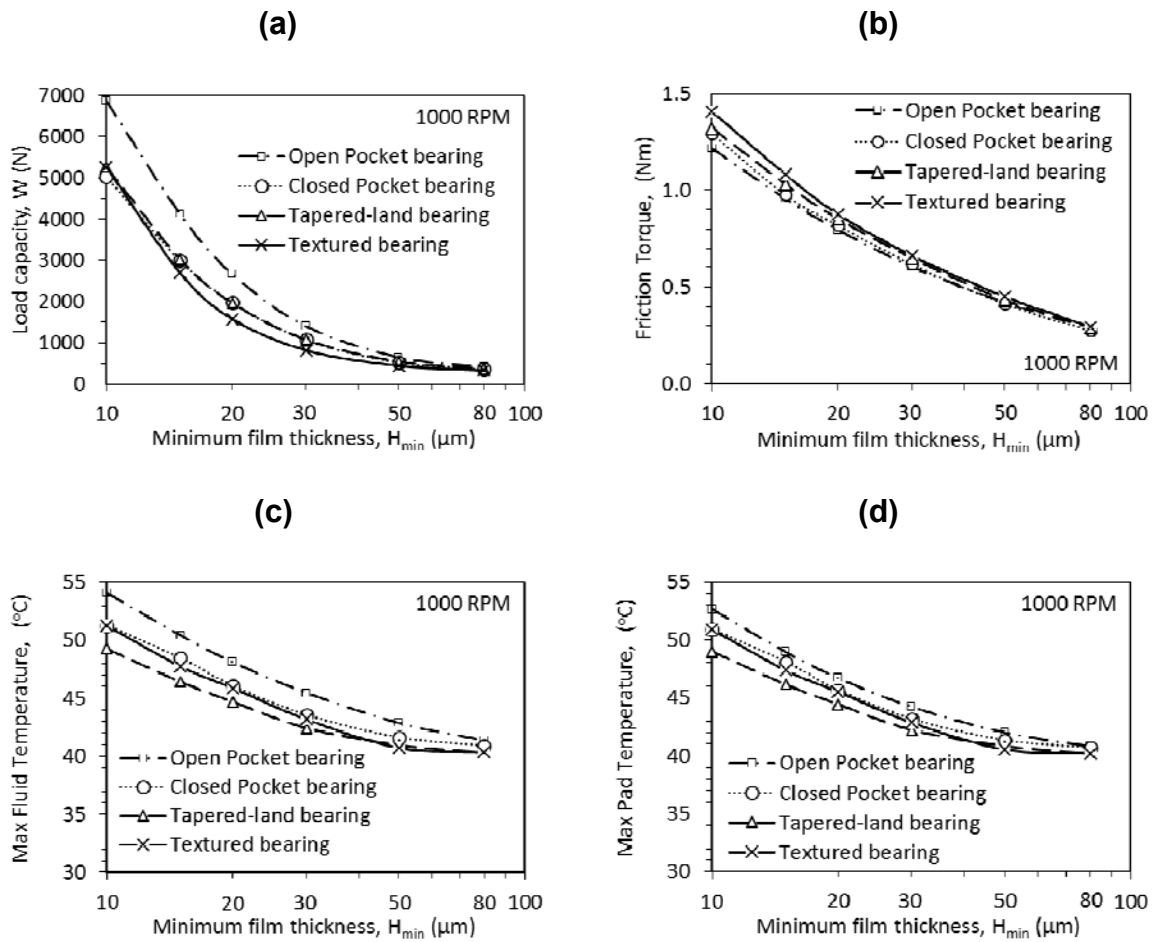


Figure 7. Computed values of (a) load carrying capacity, (b) friction torque, (c) maximum fluid temperature, and (d) maximum pad temperature versus minimum film thickness, for the reference design of the four types of thrust bearing of the present study, at $N=1000$ RPM.

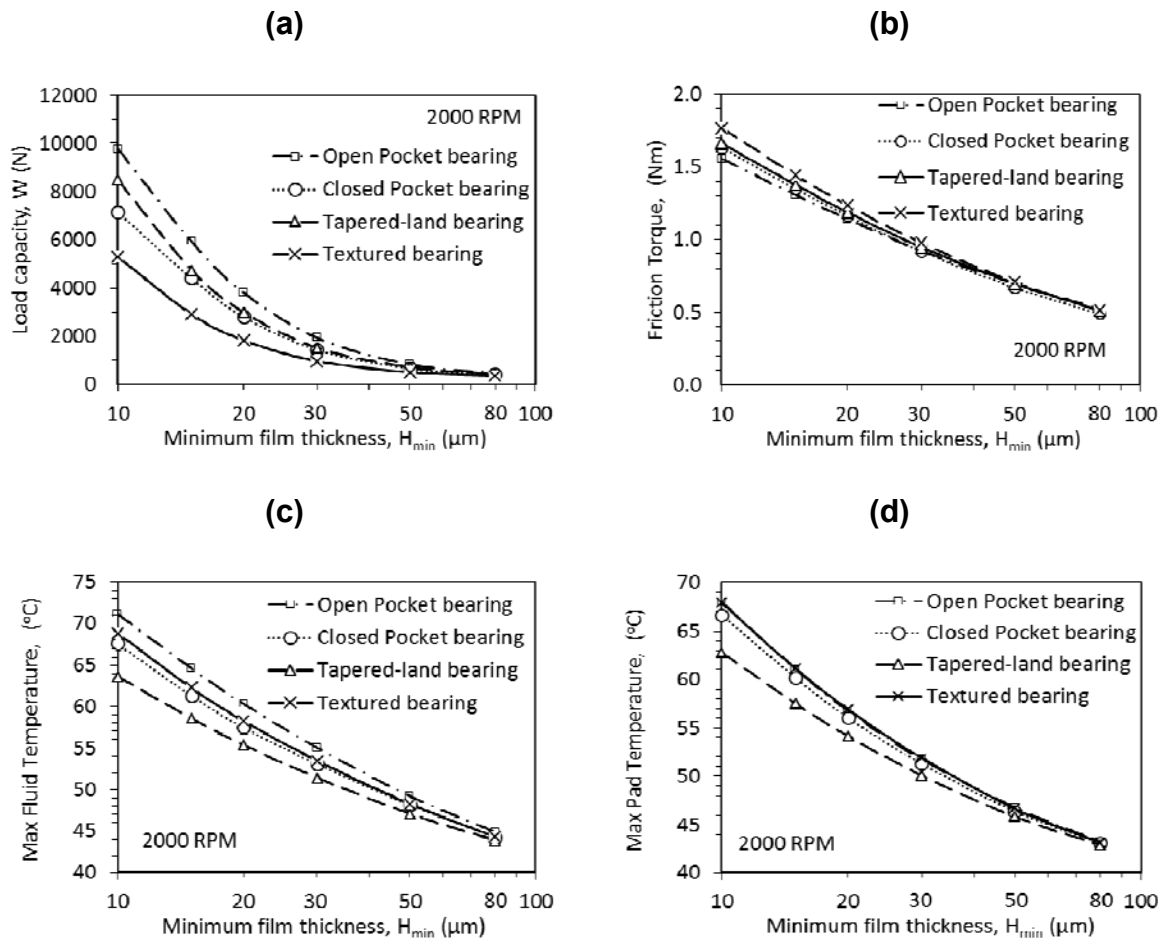


Figure 8. Computed values of (a) load carrying capacity, (b) friction torque, (c) maximum fluid temperature, and (d) maximum pad temperature versus minimum film thickness, for the reference design of the four types of thrust bearing of the present study, at $N=2000$ RPM.

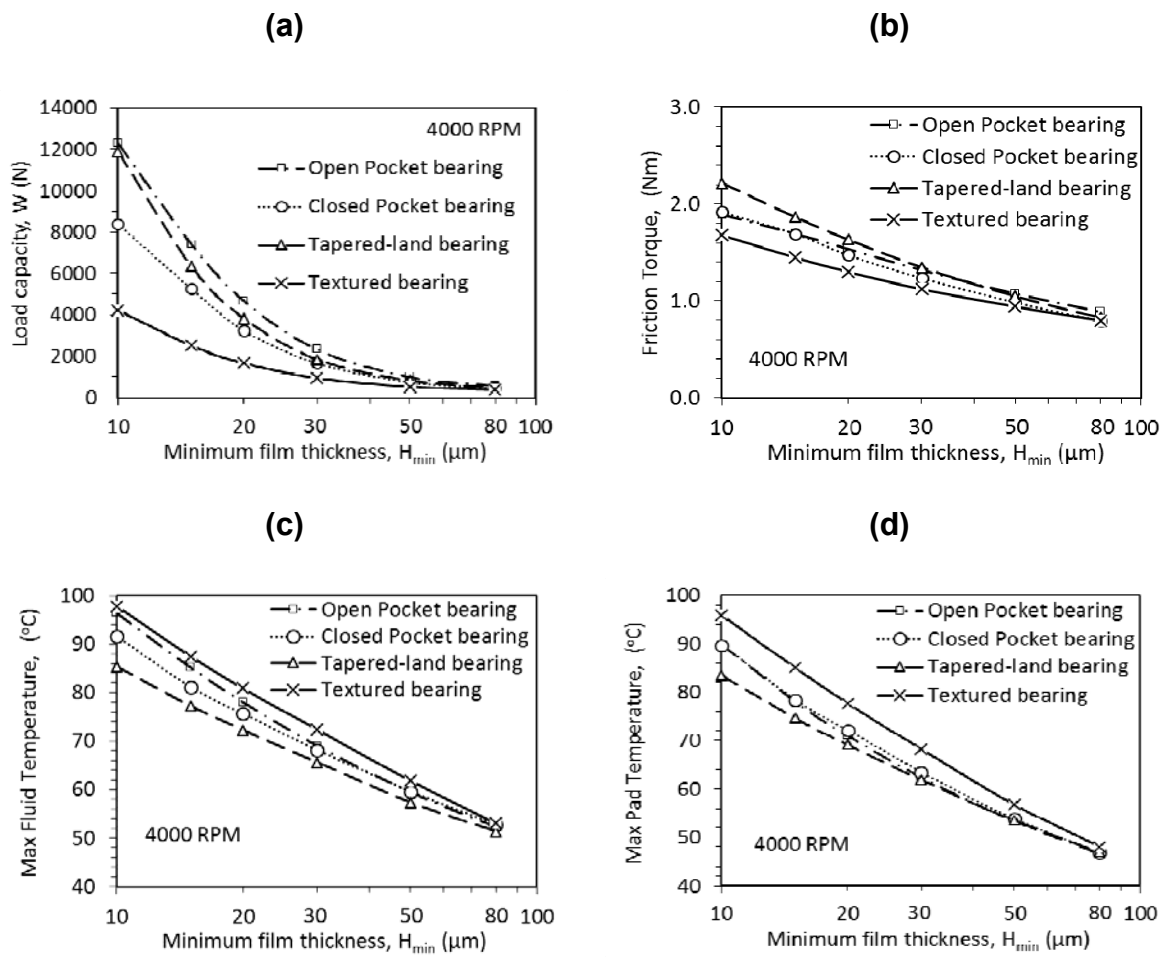


Figure 9. Computed values of (a) load carrying capacity, (b) friction torque, (c) maximum fluid temperature, and (d) maximum pad temperature versus minimum film thickness, for the reference design of the four types of thrust bearing of the present study, at $N=4000$ RPM.

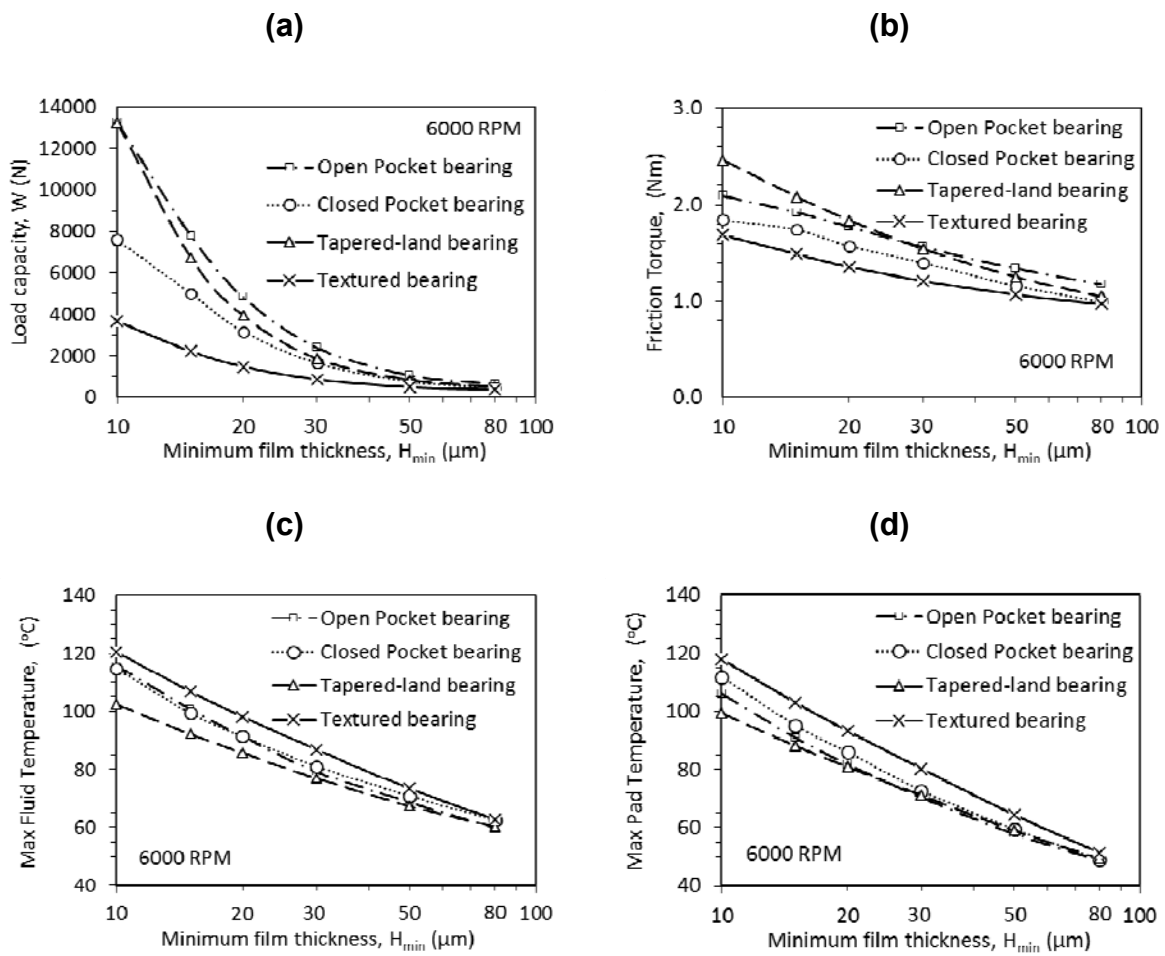


Figure 10. Computed values of (a) load carrying capacity, (b) friction torque, (c) maximum fluid temperature, and (d) maximum pad temperature versus minimum film thickness, for the reference design of the four types of thrust bearing of the present study, at $N=6000$ RPM.

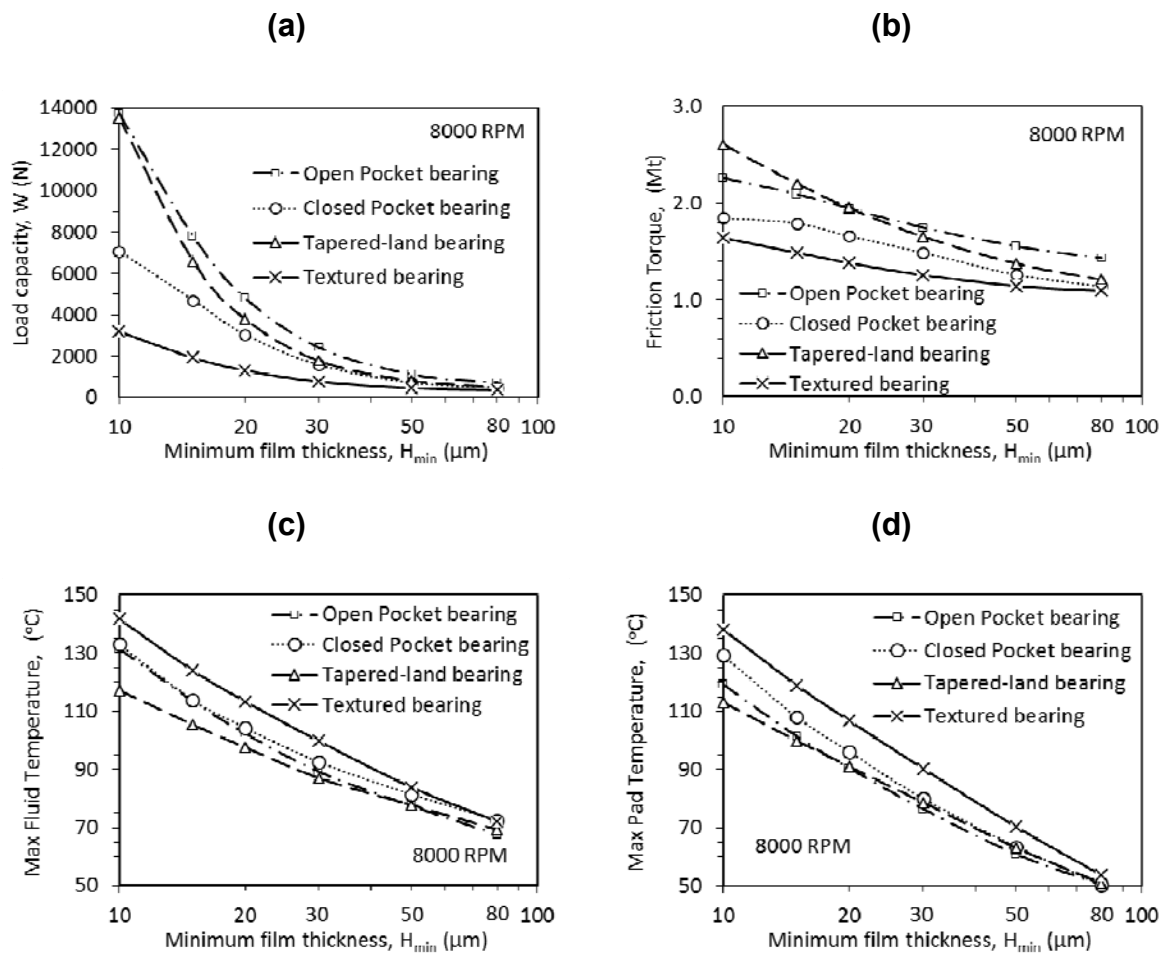


Figure 11. Computed values of (a) load carrying capacity, (b) friction torque, (c) maximum fluid temperature, and (d) maximum pad temperature versus minimum film thickness, for the reference design of the four types of thrust bearing of the present study, at $N=8000$ RPM.

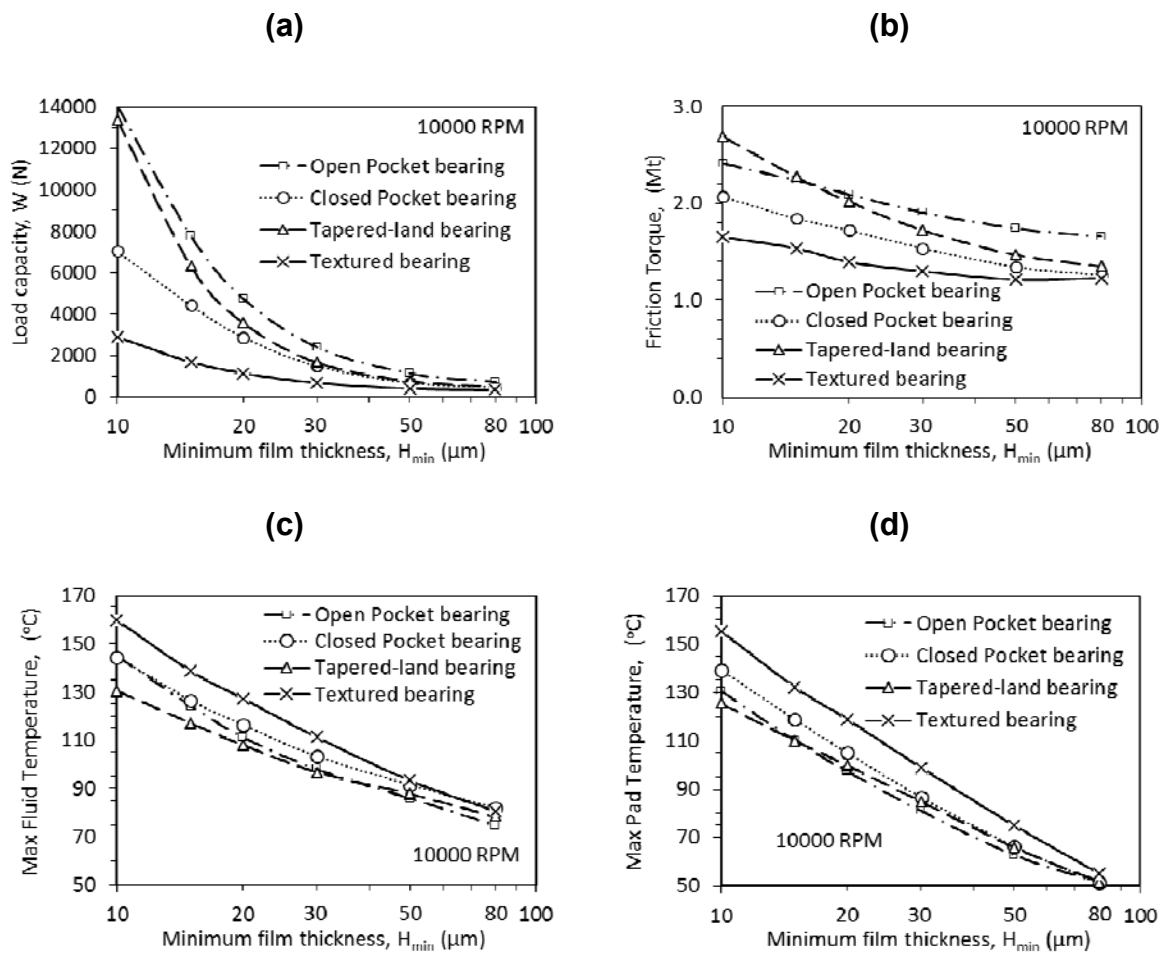


Figure 12. Computed values of (a) load carrying capacity, (b) friction torque, (c) maximum fluid temperature, and (d) maximum pad temperature versus minimum film thickness, for the reference design of the four types of thrust bearing of the present study, at $N=10000$ RPM.

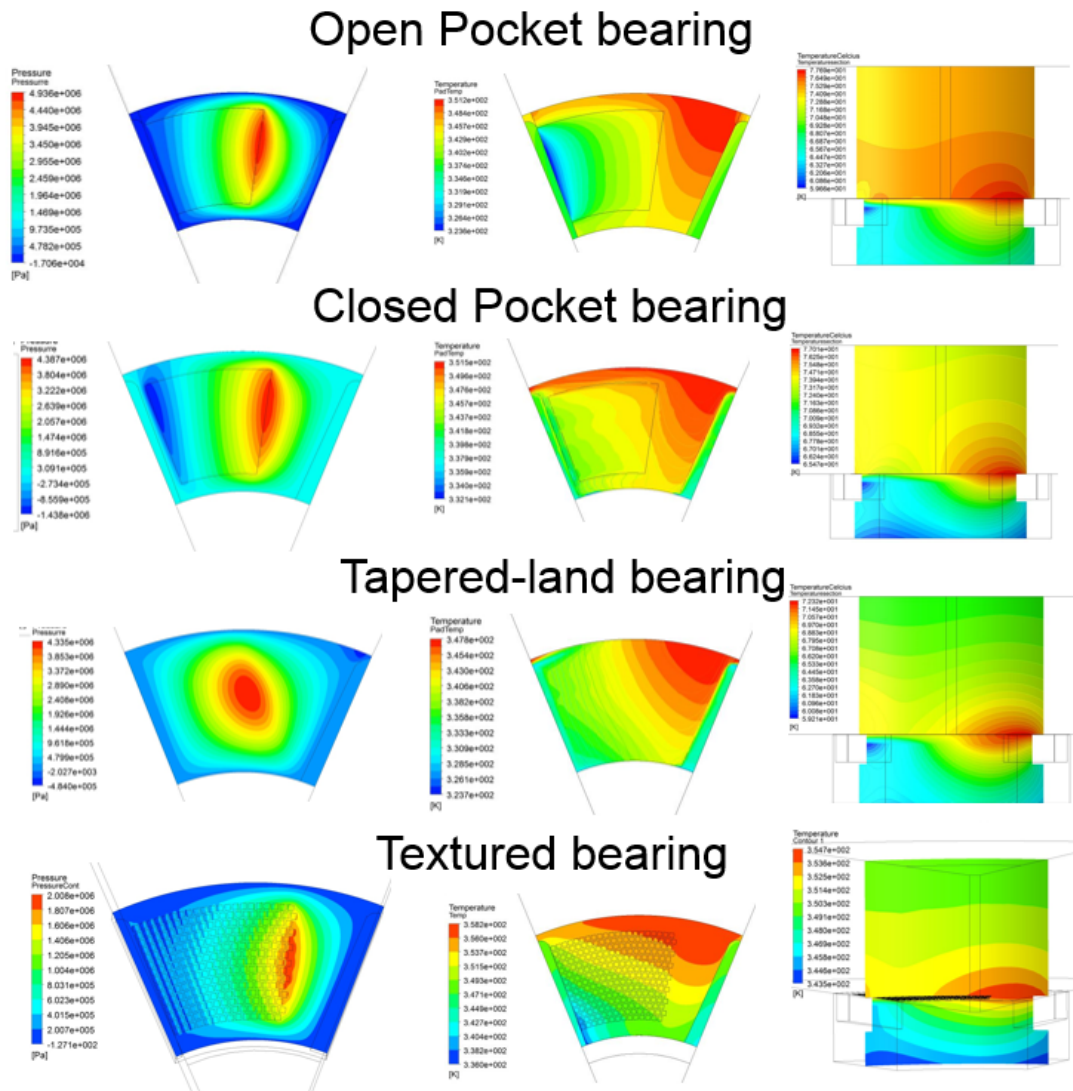


Figure 13. Distributions of computed fields for the reference design of the four types of thrust bearings of the present study, at $N=4000$ RPM, $H_{min}=15 \mu\text{m}$. Left column: pressure distributions on the rotor surface; middle column: temperature distributions on the stator surface; right column: temperature distributions on the bearing mid-plane.

Texture / pocket / taper depth variation

In thrust bearings, the texture/pocket/taper depth is expected to affect performance indices. At small depth levels, a further increase in depth is expected to increase pressure buildup, and thus load capacity. For high depths, the presence of secondary flow structures is expected to increase substantially the energy dissipation, and thus to prohibit further increase in load capacity. Therefore, optimal depths exist, which, based on recent studies, are of the order of minimum film thickness. In Figure 15 - Figure 18, the computed values of load carrying capacity versus pocket/taper/ texture depth are presented, for different values of minimum film thickness, for the

four bearing types of the present study. Here, the value of bearing rotational speed is varied from 1000 RPM to 10000 RPM. The existence of an optimal depth, which is a function of both load and rotational speed, is observed for all cases.

In particular, regarding open/closed pocket bearings, Figure 14 and Figure 15 demonstrate that, for operation at low rotational speed and low value of film thickness, H_{min} , an optimum ratio of pocket depth, H_d , to H_{min} of approximately 2 is identified. For higher values of H_{min} , the optimal ratio H_d / H_{min} decreases to approximately 1.5 ($H_{min}=20 \mu\text{m}$), and to 1 ($H_{min}=30 \mu\text{m}$, $H_{min}=50 \mu\text{m}$). For very low values of H_{min} (very high thrust loads), increase of pocket depth beyond the optimal value leads to a substantial decrease of load capacity. For the range of pocket depths considered here, this decrease can be a factor of 4, at low or moderate values of rotational speed. The effect becomes milder or even negligible at higher values of H_{min} . At high values of rotational speed (above 4000 - 6000 RPM), and very low values of H_{min} an optimal H_d / H_{min} of approximately 1 is favored, which increases at increasing H_{min} . Regarding tapered-land bearings, Figure 16 shows that, at low values of minimum film thickness, H_{min} , an optimum ratio of taper depth, H_d , to H_{min} of approximately 3 is identified. At higher values of H_{min} , the optimal ratio H_d / H_{min} decreases to approximately 2.5 ($H_{min}=20 \mu\text{m}$), and to 1.7-2.0 ($H_{min}=30 \mu\text{m}$, $H_{min}=50 \mu\text{m}$). At very low values of H_{min} (very high thrust loads), an increase of taper depth beyond the optimal value leads to a significant decrease of load capacity. The effect becomes less pronounced or even negligible at higher values of H_{min} . Finally, for textured bearings, Figure 17 shows that, for low values of rotational speed and minimum film thickness, H_{min} , an optimum ratio of texture depth, H_d , to H_{min} of approximately 2 exists. The optimum ratio value decreases as H_{min} is increased (becomes approximately 1.5 for $H_{min}=20 \mu\text{m}$, and 1 for $H_{min}=30 \mu\text{m}$, $H_{min}=50 \mu\text{m}$). In the limit of very low values of H_{min} (very high thrust loads), an increase of texture depth beyond the optimal value leads to a drastic decrease of load capacity. The decrease is less pronounced or even negligible at higher values of H_{min} . An optimal ratio H_d / H_{min} of approximately 1 is favored at high rotational speeds (above 4000 RPM).

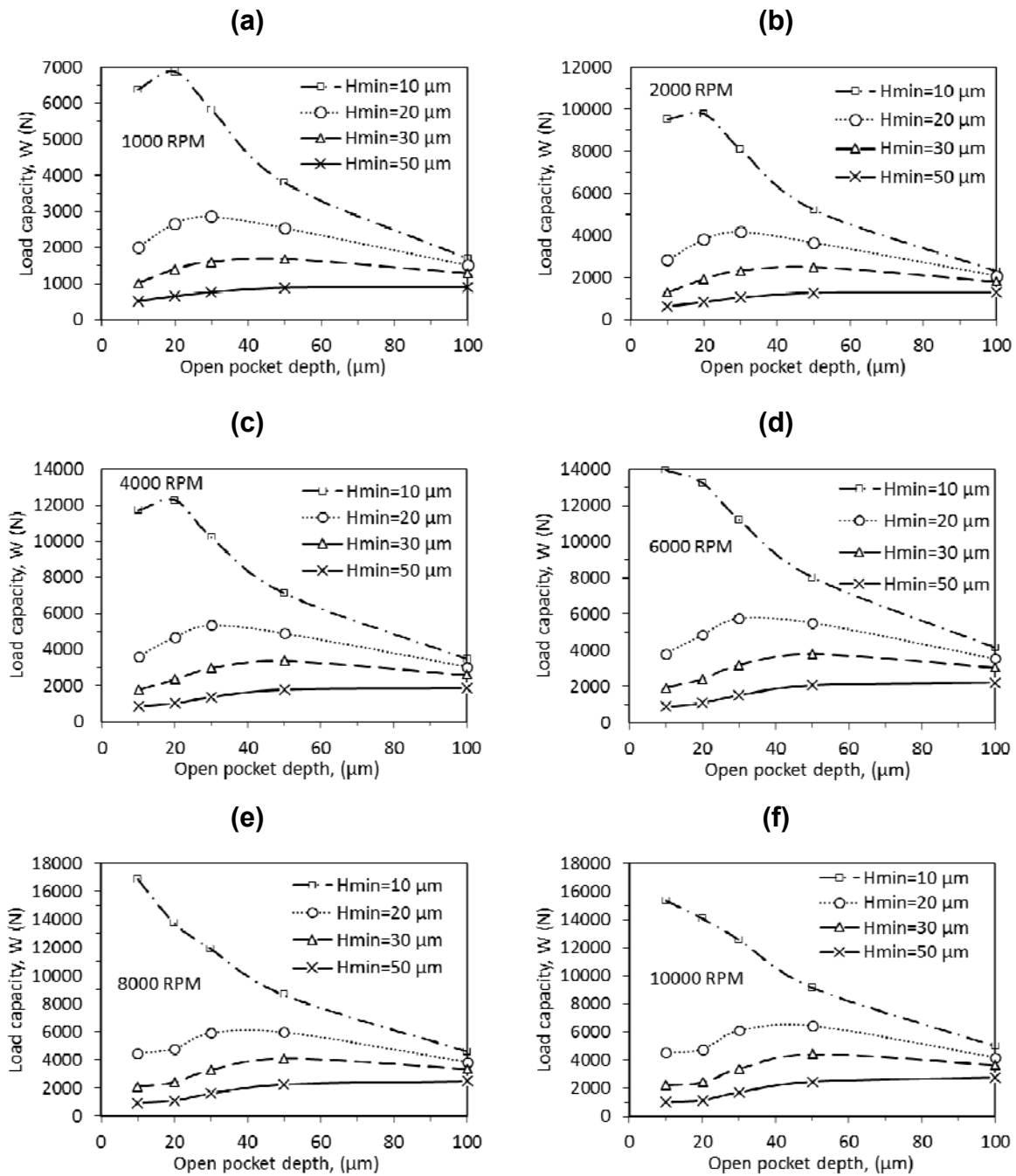


Figure 14. Open pocket bearing: computed values of load carrying capacity versus pocket depth, for different values of minimum film thickness. The six graphs presented correspond to rotational speeds from 1000 to 10000 RPM.

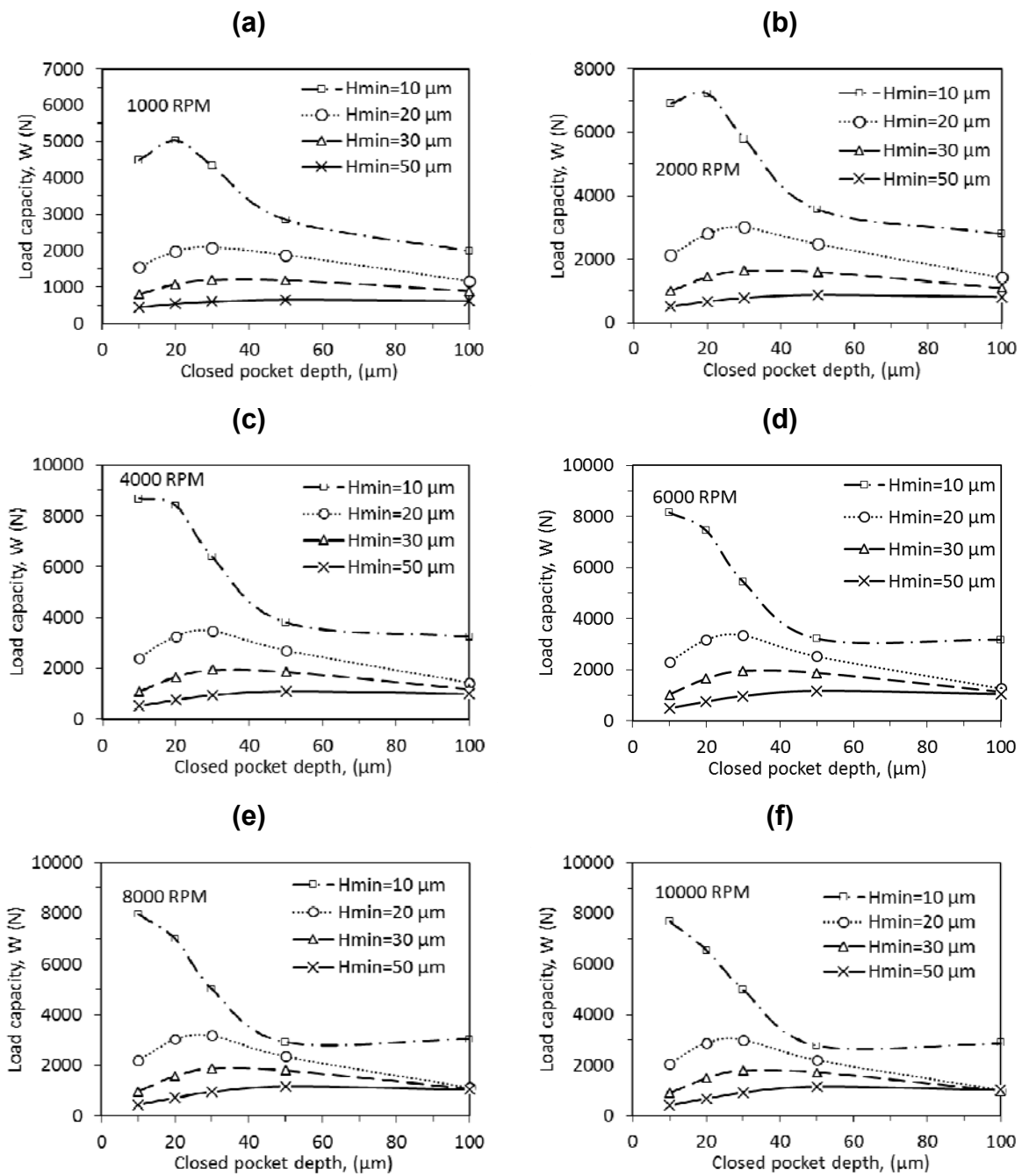


Figure 15. Closed pocket bearing: computed values of load carrying capacity versus pocket depth, for different values of minimum film thickness. The six graphs presented correspond to rotational speeds from 1000 to 10000 RPM.

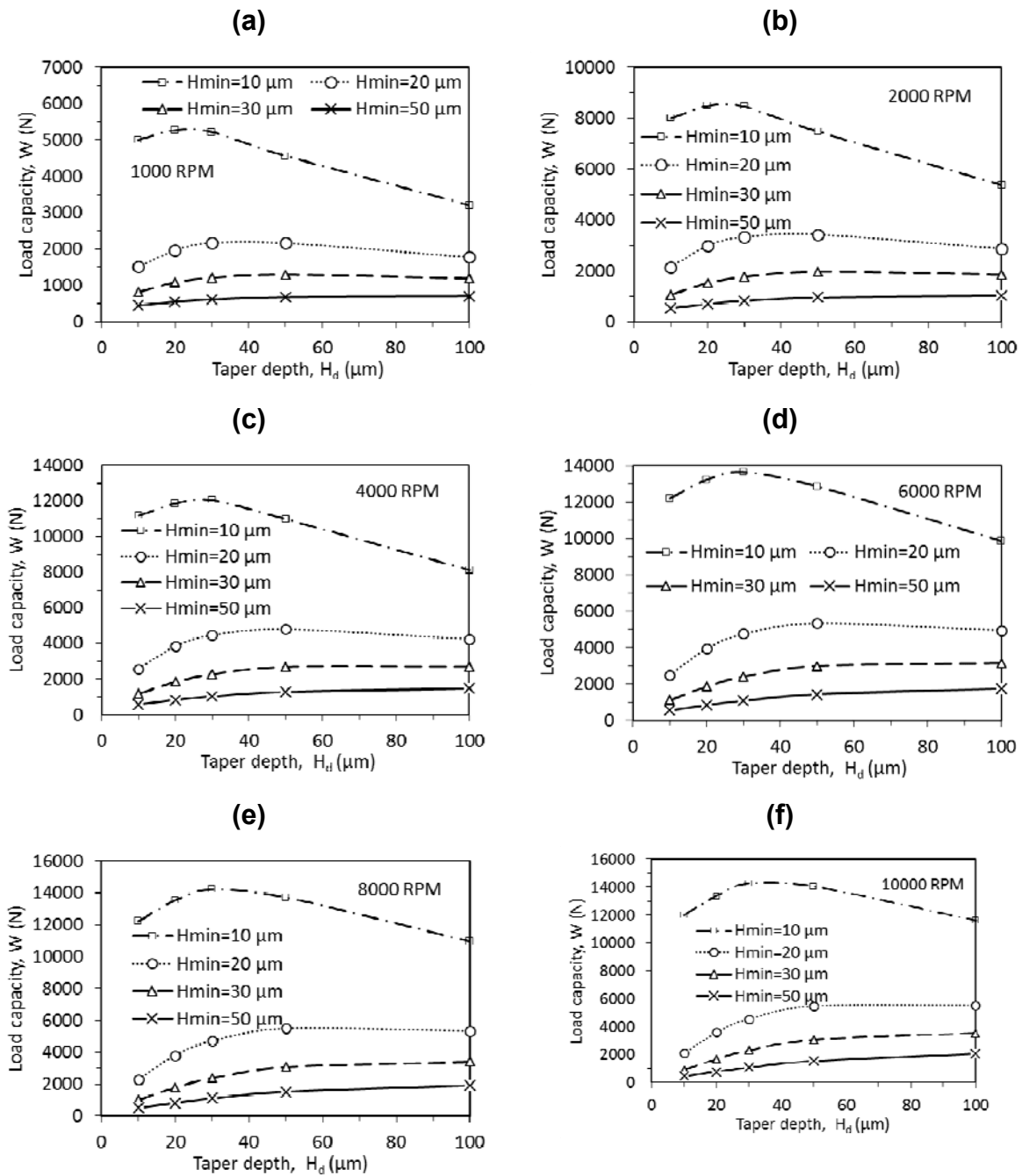


Figure 16. Tapered-land bearing: computed values of load carrying capacity versus taper depth, for different values of minimum film thickness. The six graphs presented correspond to rotational speeds from 1000 to 10000 RPM.

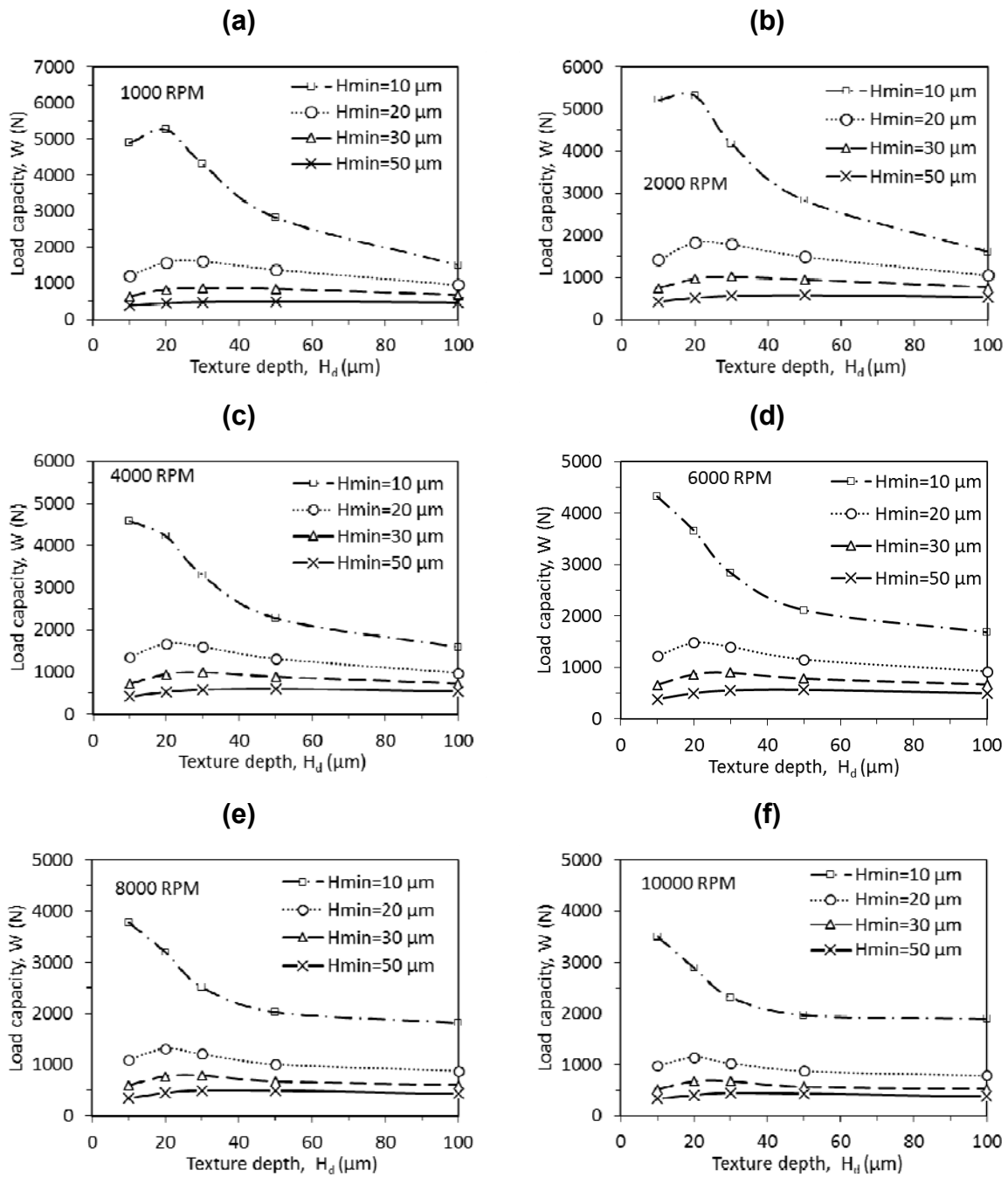


Figure 17. Textured bearing: computed values of load carrying capacity versus dimple depth, for different values of minimum film thickness. The six graphs presented correspond to rotational speeds from 1000 to 10000 RPM.

Operation at a prescribed bearing load

Thrust bearing operation aims at supporting an external axial load. Therefore, a comparison of the four bearing types considered in the present chapter has been performed for two representative values of load capacity, 2000 N and 4000 N. Two values of rotational speed have been accounted for, equal to 4000 RPM and 8000 RPM. The results are presented in Figures 19-22 in terms of the computed pressure distributions and temperature distributions on the stator surface; the corresponding values of minimum film thickness, friction torque and maximum stator temperature are also included. These results demonstrate the superiority of the open pocket bearing, illustrated by the high values of minimum film thickness and the corresponding low levels of maximum oil temperature. The tapered-land bearing is characterized by a comparable performance. In all cases considered, the textured bearing operation is characterized by substantially lower values of minimum film thickness, accompanied by significantly higher values of maximum pad temperature, which, for the case of thrust load of 4000 N and rotational speed of 8000 RPM, reaches 145°C, approximately 60°C higher than that of the open pocket bearing.

W=2000 N, N=4000 RPM			
	Operational Characteristics	Pressure distribution (rotor-fluid interface)	Temperature distribution (pad top)
Open pocket bearing	$H_{min}=33.2 \mu\text{m}$ $M_t=1.27 \text{ Nm}$ $T_{pad,max}=60.5 \text{ }^\circ\text{C}$		
Closed pocket bearing	$H_{min}=26.6 \mu\text{m}$ $M_t=1.32 \text{ Nm}$ $T_{pad,max}=65.6 \text{ }^\circ\text{C}$		
Tapered-land bearing	$H_{min}=29 \mu\text{m}$ $M_t=1.37 \text{ Nm}$ $T_{pad,max}=62.6 \text{ }^\circ\text{C}$		
Textured bearing	$H_{min}=17.5 \mu\text{m}$ $M_t=1.34 \text{ Nm}$ $T_{pad,max}=81.3 \text{ }^\circ\text{C}$		

Figure 18. Distributions of computed fields for four types of thrust bearings, at $N=4000 \text{ RPM}$, for a constant axial load of 2000 N . Left column: pressure distribution on the rotor surface; right column: temperature distribution on the stator surface. For each case, the values of minimum film thickness, friction torque and max. stator temperature are also included.

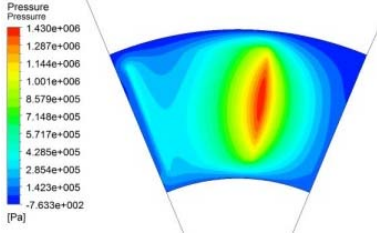
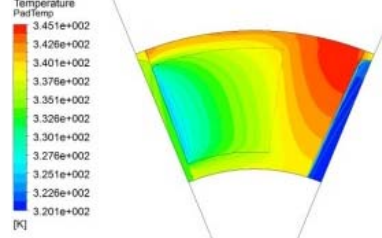
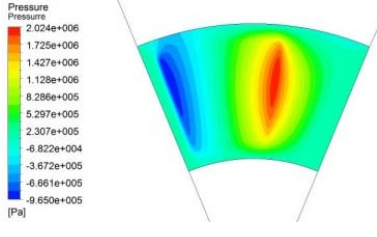
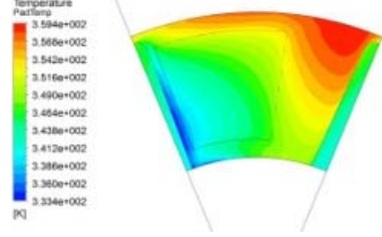
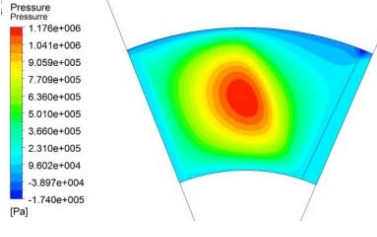
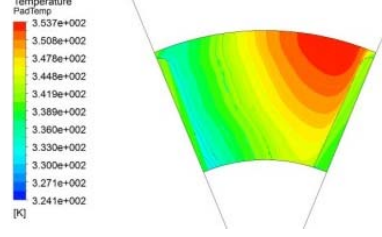
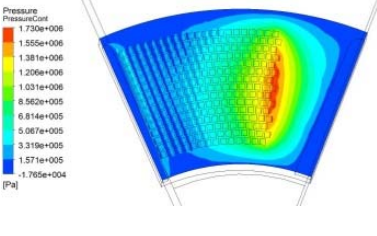
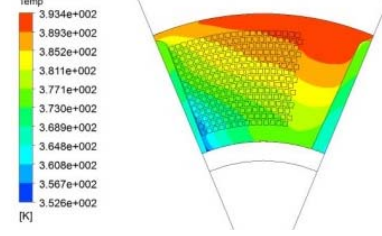
W=2000 N, N=8000 RPM			
	Operational Characteristics	Pressure distribution (rotor-fluid interface)	Temperature distribution (pad top)
Open pocket bearing	$H_{min}=34.2 \mu\text{m}$ $M_t=1.69 \text{ Nm}$ $T_{pad,max}=72 \text{ }^\circ\text{C}$		
Closed pocket bearing	$H_{min}=25.7 \mu\text{m}$ $M_t=1.56 \text{ Nm}$ $T_{pad,max}=86.2 \text{ }^\circ\text{C}$		
Tapered-land bearing	$H_{min}=28.3 \mu\text{m}$ $M_t=1.69 \text{ Nm}$ $T_{pad,max}=80.6 \text{ }^\circ\text{C}$		
Textured bearing	$H_{min}=14.6 \mu\text{m}$ $M_t=1.5 \text{ Nm}$ $T_{pad,max}=120.2 \text{ }^\circ\text{C}$		

Figure 19. Distributions of computed fields for four types of thrust bearings, at $N=8000 \text{ RPM}$, for a constant axial load of 2000 N . Left column: pressure distribution on the rotor surface; right column: temperature distribution on the stator surface. For each case, the values of minimum film thickness, friction torque and max. stator temperature are also included.

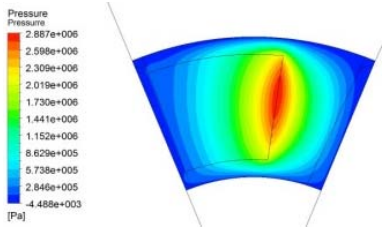
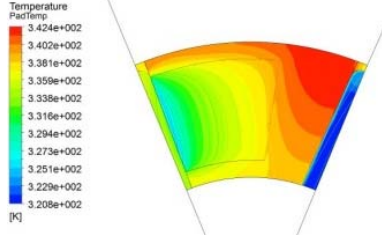
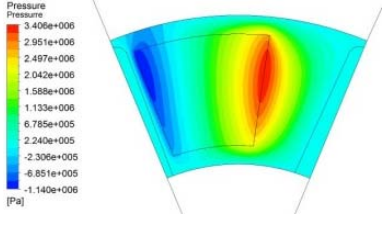
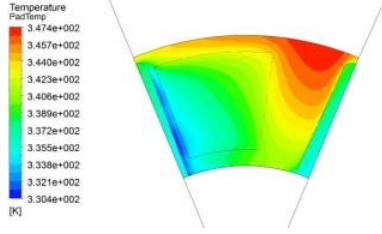
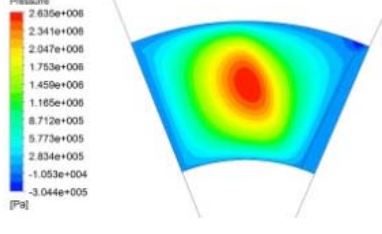
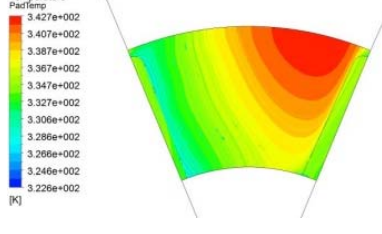
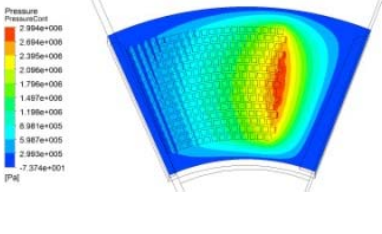
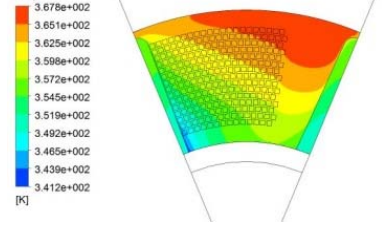
W=4000 N, N=4000 RPM			
	Operational Characteristics	Pressure distribution (rotor-fluid interface)	Temperature distribution (pad top)
Open pocket bearing	$H_{min}=21.6 \mu\text{m}$ $M_t=1.5 \text{ Nm}$ $T_{pad,max}=69.3 \text{ }^\circ\text{C}$		
Closed pocket bearing	$H_{min}=17.9 \mu\text{m}$ $M_t=1.56 \text{ Nm}$ $T_{pad,max}=74.3 \text{ }^\circ\text{C}$		
Tapered-land bearing	$H_{min}=19.5 \mu\text{m}$ $M_t=1.66 \text{ Nm}$ $T_{pad,max}=69.6 \text{ }^\circ\text{C}$		
Textured bearing	$H_{min}=10.5 \mu\text{m}$ $M_t=1.64 \text{ Nm}$ $T_{pad,max}=94.6 \text{ }^\circ\text{C}$		

Figure 20. Distributions of computed fields for four types of thrust bearings, at $N=4000 \text{ RPM}$, for a constant axial load of 4000 N . Left column: pressure distribution on the rotor surface; right column: temperature distribution on the stator surface. For each case, the values of minimum film thickness, friction torque and max. stator temperature are also included.

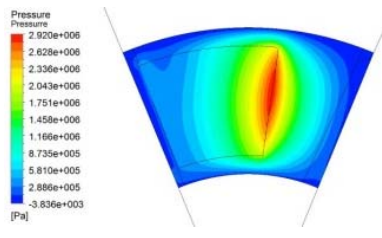
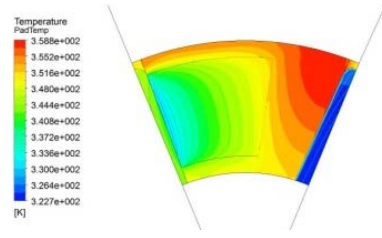
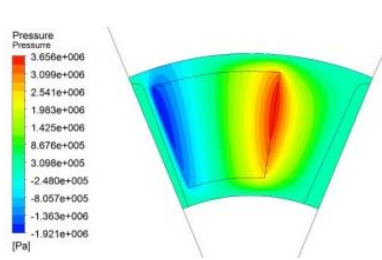
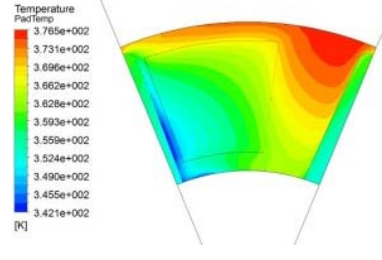
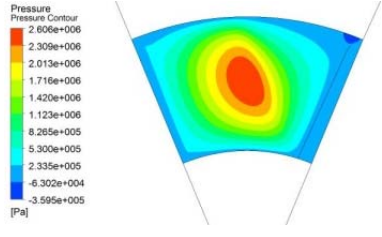
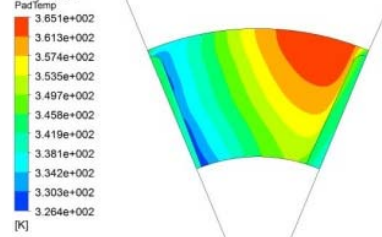
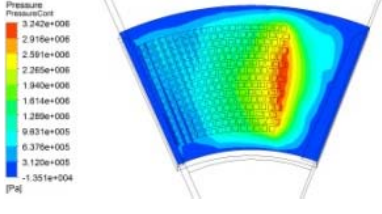
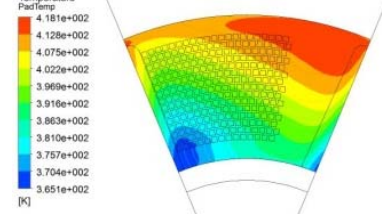
W=4000 N, N=8000 RPM			
	Operational Characteristics	Pressure distribution (rotor-fluid interface)	Temperature distribution (pad top)
Open pocket bearing	$H_{min}=22.72 \mu\text{m}$ $M_t=1.88 \text{ Nm}$ $T_{pad,max}=85.7 \text{ }^\circ\text{C}$		
Closed pocket bearing	$H_{min}=16.81 \mu\text{m}$ $M_t=1.74 \text{ Nm}$ $T_{pad,max}=103.4 \text{ }^\circ\text{C}$		
Tapered-land bearing	$H_{min}=19.4 \mu\text{m}$ $M_t=1.96 \text{ Nm}$ $T_{pad,max}=92.0 \text{ }^\circ\text{C}$		
Textured bearing	$H_{min}=7.885 \mu\text{m}$ $M_t=1.87 \text{ Nm}$ $T_{pad,max}=145 \text{ }^\circ\text{C}$		

Figure 21. Distributions of computed fields for four types of thrust bearings, at $N=8000 \text{ RPM}$, for a constant axial load of 4000 N . Left column: pressure distribution on the rotor surface; right column: temperature distribution on the stator surface. For each case, the values of minimum film thickness, friction torque and max. stator temperature are also included.

2.5. Conclusions

In the present chapter, a detailed study of the performance of four types of sector pad thrust bearings by means of Computational Fluid Dynamics has been presented. The four bearings, of comparable dimensions, were: (a) an open pocket bearing, (b) a closed pocket bearing, (c) a tapered-land bearing, and (d) a bearing partially textured with rectangular dimples. Here, the effects of varying rotational speed, minimum film thickness, as well as texture/taper depth on bearing performance indices were quantified. Further, bearing performance at representative (constant) values of axial load, for two values of rotational speed, were evaluated. The results have demonstrated a very good performance of the open pocket bearing, as well as of the tapered-land bearing. The textured bearing offers reasonable performance only at low to moderate loads and low values of rotational speed. The present results form a useful reference that can be utilized in the design of sector pad thrust bearings.

3. Computational Investigation of Thermoelastohydrodynamic (TEHD) Lubrication in a Textured Sector-Pad Thrust Bearing

3.1. Introduction

Mechanical (elastic) deformations and thermal expansion affect bearing performance, especially at high values of load and rotational speed. Therefore, at demanding operating conditions, bearing parameters (load capacity, friction coefficient) calculated by means of thermohydrodynamic (THD) analysis may deviate from the actual ones. In this chapter the effect of pressure field on the deformations of the rotor and stator of a representative textured thrust bearing are analyzed by means of an one-way FSI approach, which couples CFD calculations in the lubricant domain with FEM calculations of elastic deformation of the rotor and pad solid elements, at representative values of rotor rotational speed and rotor thickness.

3.2. Bearing geometry

The thrust bearing configuration investigated in this chapter is that of the textured thrust bearing investigated in Chapter 2 (see Figures 22 and 23).

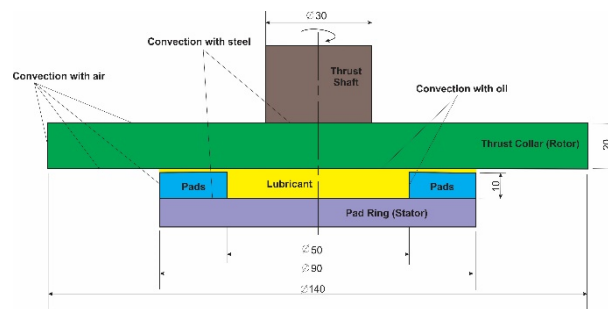


Figure 22. Geometry of computational model.

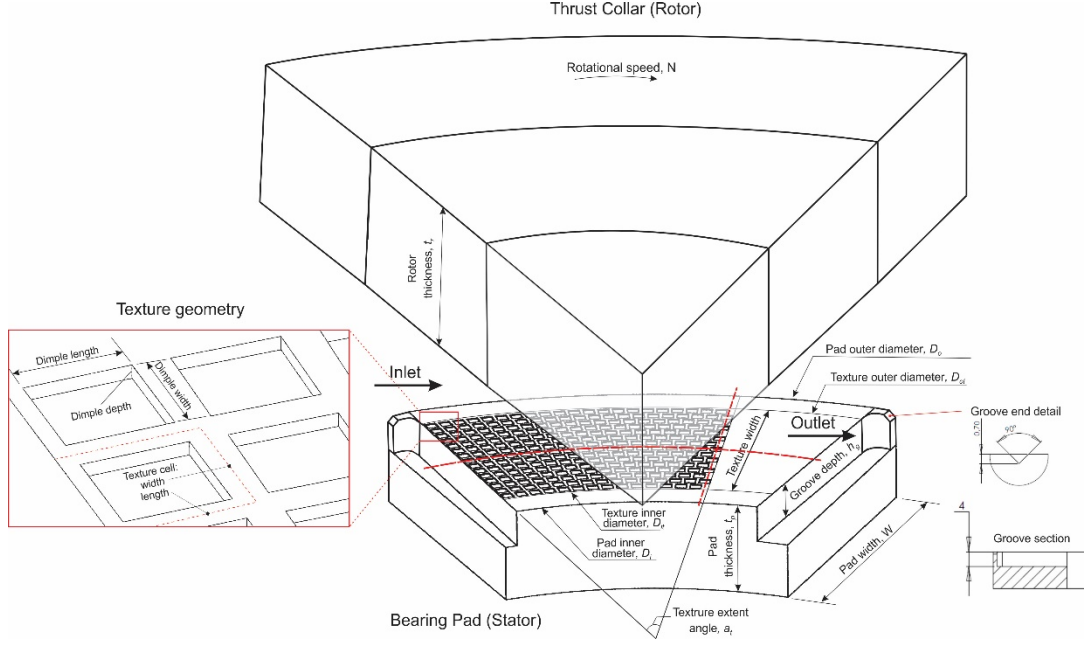


Figure 23. Sketch of the bearing of the present study and top view of the bearing pad

3.3. Computational model

The conservation equations, solved with the CFD code ANSYS CFX for steady incompressible flow with zero gravitational and external body forces have been presented in Section 2.3 (Eqs.1-5)

The pad and the rotor undergo elastic deformation due the exerted pressure distribution and the thermal expansion. The total solid strain can be computed as:

$$\boldsymbol{\varepsilon} = \boldsymbol{\varepsilon}^{el} + \boldsymbol{\varepsilon}^{th} \quad (8)$$

Where $\boldsymbol{\varepsilon}$ is total strain *vector* = $[\varepsilon_x, \varepsilon_y, \varepsilon_z, \varepsilon_{xy}, \varepsilon_{yz}, \varepsilon_{xz}]^T$ and $\boldsymbol{\varepsilon}^{el}$, $\boldsymbol{\varepsilon}^{th}$ the elastic and thermal strain vectors, respectively.

The elastic strain $\boldsymbol{\varepsilon}^{el}$ of each solid part can be computed from the solution of the elasticity equation:

$$\boldsymbol{\sigma}^{el} = D\boldsymbol{\varepsilon}^{el} \quad (9)$$

where $\boldsymbol{\sigma}^{el}$ is the elastic stress *vector* = $[\sigma_x, \sigma_y, \sigma_z, \sigma_{xy}, \sigma_{yz}, \sigma_{xz}]^T$ and D_{st} the stiffness matrix of the solid, given below.

$$D_{st}^{-1} = \begin{bmatrix} 1/E_x & -v_{xy}/E_x & -v_{xz}/E_x & 0 & 0 & 0 \\ -v_{yx}/E_y & 1/E_y & -v_{yz}/E_y & 0 & 0 & 0 \\ -v_{zx}/E_z & -v_{zy}/E_z & 1/E_z & 0 & 0 & 0 \\ 0 & 0 & 0 & 1/G_{xy} & 0 & 0 \\ 0 & 0 & 0 & 0 & 1/G_{yz} & 0 \\ 0 & 0 & 0 & 0 & 0 & 1/G_{xz} \end{bmatrix} \quad (10)$$

Here, E_i ($i = x, y, z$) is the Young's modulus of elasticity in the i^{th} direction, v_{ij} is the Poisson ratio for orthotropic materials, and G_{ij} is the shear modulus in the ij plane.

The solid thermal strain ε^{th} can be computed from the following equation:

$$\varepsilon^{th} = \Delta T [a_x^{se}, a_y^{se}, a_z^{se}, 0, 0, 0]^T \quad (11)$$

where ε^{th} is the thermal strain vector, $\Delta T = T - T_{ref}$ (T is the local and T_{ref} is the reference, strain-free temperature), and a_i^{se} , $i = x, y, z$, are the coefficients of thermal expansion in the i^{th} direction.

In the present work, the values of thermophysical properties utilized are given below:

Lubricant :

$$Cp = 20000 \text{ J / kg} \cdot \text{K}, \lambda_f = 0.13 \text{ W / m} \cdot \text{K}.$$

Solids (isotropic):

$$Cp = 434 \text{ J / kg} \cdot \text{K} \text{ and } \lambda_{sp} = 50 \text{ W / m} \cdot \text{K} \quad \lambda_{sv} = 60,5 \text{ W / m} \cdot \text{K} \quad , \quad a_{pad} = 18 \times 10^{-6} \text{ K}^{-1} \quad , \\ a_{rotor} = 11,5 \times 10^{-6} \text{ K}^{-1}$$

$$E_{sp} = 1,2 \times 10^{11} \text{ Pa}, E_{sr} = 2,1 \times 10^{11} \text{ Pa} \quad , \quad v_{sp} = 0,33 \quad v_{sr} = 0,3.$$

In the present study, $a^{se} = 0$, i.e. **thermal deformation is not taken into account.**

The density of the lubrication oil utilized (ISO VG 46) is 870 kg/m^3 , while a temperature dependent viscosity is considered, according to the McCoull and Walther relation Eq:(5), as used in the previous chapter.

The flow dynamics depends (a) on the Reynolds number, Re , which is defined at the thrust bearing mid-sector, in terms of the rotor speed, $U = \omega R_m$, and the minimum film thickness H_{min} (ω is the rotor angular velocity and R_m the pad mid-sector radius), and (b) on the lubricant Prandtl number, at a representative temperature. In the present study, for a representative rotational speed of 4000 RPM ($U = 14.65 \text{ m/s}$), a minimum film thickness value of $15 \text{ } \mu\text{m}$ and an average lubricant temperature of $70 \text{ } ^\circ\text{C}$, $Re = 13.7$. The computed thrust load is 2934 N .

Spatial discretization and boundary conditions

The 3-D mesh generated for the fluid domain contains approximately 2×10^6 hexahedral cells (finite volumes). In each pad dimple, the fluid volume mesh typically has 10 cell layers in the axial direction, 8×8 cells on a rectangular cross-section, and 8 cell layers in the stator-rotor clearance. The rotor domain comprises approximately 10^6 cells and the pad domain 1.5×10^6 cells. No-slip conditions are implemented for the fluid velocity at the pad and rotor inner walls.

The inner surface of the fluid domain is considered as an inlet boundary, with a pressure value of 1.5×10^5 Pa above atmospheric and a constant oil temperature of 40°C . The outer surface of the fluid domain is considered as outlet boundary, with atmospheric pressure, and a Neumann boundary condition for temperature. Regarding the groove symmetry planes (inflow and outflow boundaries for the present problem setup), rotational periodicity has been considered, both for the velocity and temperature fields. Regarding thermal boundary conditions, the rotor is assumed stationary (frozen), therefore a constant thermal loading of the rotor is computed. At the fluid-pad and fluid-rotor interfaces, continuity of temperature and heat flux is considered. At the leading/trailing edges of the rotor and the pad, conditions of rotational periodicity are applied. At the remaining external surfaces of the rotor and the pad, appropriate combinations of convection coefficient, a_{conv} , and ambient temperature, T_{amb} , are prescribed, following the work in [9]; they are presented below.

Regarding elasticity boundary conditions, the pad bottom is assumed fixed (zero displacements/rotations), and the rotor is assumed clamped up to a radius of 25 mm (pad inner radius). The fluid-pad and fluid-rotor interfaces are considered as coupling walls. A one-way fluid-structure interaction (FSI) technique has been applied to impose computed pressure on the solid surfaces, as boundary condition for solving the solid elasticity problems.

For the given problem setup, grid independence studies have considered coarser grids than the high resolution one described above. The results have demonstrated differences in load capacity and computed temperatures of the order of 1%.

In the fluid-pad and fluid-rotor interfaces, continuity of temperature and heat flux is implemented. At the remaining bearing external surfaces, the following values of convection coefficient, a_{conv} , and ambient temperature, T_{amb} , have been considered:

- Pad inner surface: $a_{conv} = 200(W/m^2 \cdot K)$, $T_{amb} = 40^\circ\text{C}$
- Pad outer surface: $a_{conv} = 25(W/m^2 \cdot K)$, $T_{amb} = 40^\circ\text{C}$
- Pad bottom: $a_{conv} = 1000(W/m^2 \cdot K)$, $T_{amb} = 40^\circ\text{C}$ (equivalent convection parameters accounting for the thermal resistance of the steel support)

- Pad leading/trailing surfaces: $a_{Conv} = 200(W/m^2 \cdot K)$, $T_{amb} = 40^{\circ}C$ (assumed convection with lubricating oil in the groove area)
- Rotor air surface: $a_{Conv} = 25(W/m^2 \cdot K)$, $T_{amb} = 20^{\circ}C$
- Rotor top inner surface (shaft location): $a_{Conv} = 1000(W/m^2 \cdot K)$, $T_{amb} = 20^{\circ}C$
- Rotor bottom inner surface: $a_{Conv} = 200(W/m^2 \cdot K)$, $T_{amb} = 40^{\circ}C$

3.4. Computational results

First, bearing operation for a reference case is considered. The parameters corresponding to the reference case are $N=4000$ RPM and $H_{min} = 15\mu m$, yielding a total bearing load $W=2934$ N. The pressure distribution at the rotor-pad interface and the temperature distribution at the pad surface are presented in Figure 24(a). Further, in Figure 24(b), temperature distribution at the pad and the rotor is presented at a vertical cross section corresponding to the pad mean radius. Figure 24(a) demonstrates a gradual pressure buildup along the main flow direction, reaching a maximum at the texture rear end. Regarding the temperature distribution, a maximum is identified at the outer region of the bearing, close to the outflow, and its location should be attributed to the combined effect of oil heating due to viscous dissipation and the action of centrifugal forces. The resulting elastic displacements of the collar and the pad are presented in Figure 25. A close similarity is found between the upper pad surface deformation field and the exerted pressure. The computed deformation field of the rotor is representative of a beam with fixed support, exhibiting large displacement values at large radii.

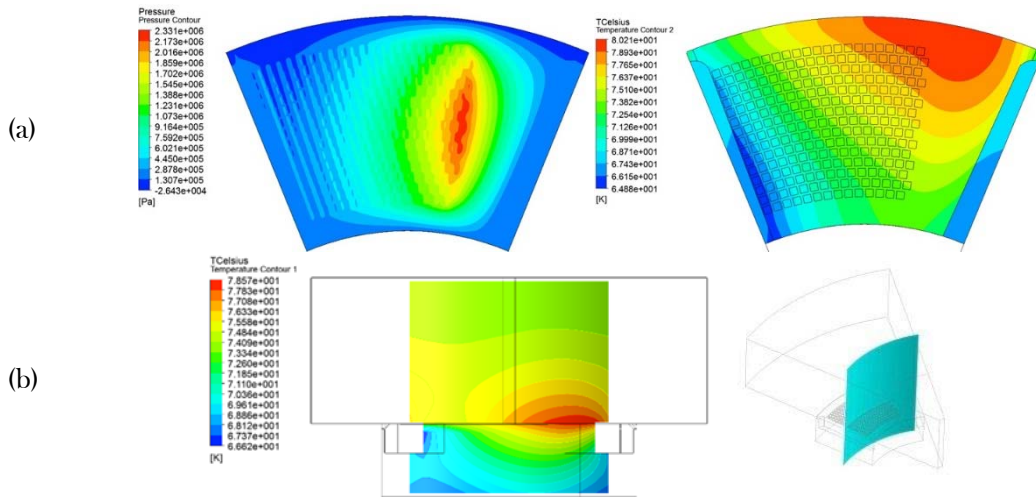


Figure 24. Reference case ($N=4000$ RPM, $H_{min}=15$ μm , resulting in a load $W=2934$ N): (a) Computed pressure distribution at the fluid-rotor interface and temperature distribution at the pad surface. (b) Temperature distribution at the pad and the collar, at a vertical cross section at the mean pad radius.

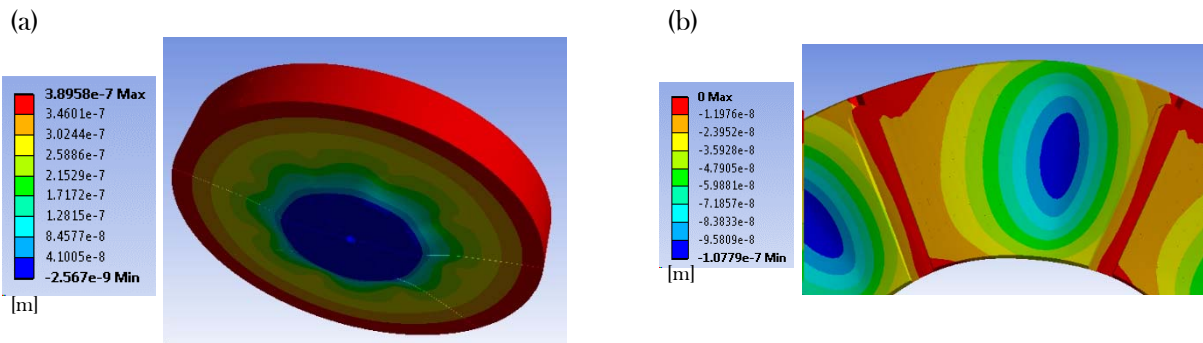


Figure 25. Reference case ($N=4000$ RPM, $H_{min}=15$ μm , resulting in a load $W=2934$ N): Plots of elastic displacement at the collar and the pad domains.

Further, the effects of bearing speed on bearing performance have been investigated, for different values of minimum film thickness, varying from 5 μm to 20 μm . Figure 26 (a)-(d) presents the computed variation of load capacity and maximum fluid temperature versus rotational speed, and the corresponding variation of maximum rotor/pad displacement. Load capacity is found to increase at low rotational speeds, reaching a maximum at speeds around 2000 RPM. The subsequent decrease, a marked difference from the continuous increase of isothermal flow (see Figure 28), is caused by the decreased levels of oil viscosity due to heating (see continuous temperature rise in the same figure). A substantial increase in load capacity (and maximum fluid temperature) is verified at decreasing values of minimum film thickness.

Figure 26 demonstrates that the maximum displacement of the collar and the pad follow the trend of load capacity, also exhibiting a maximum value at rotational speeds of approximately 2000 RPM. In all cases, the maximum rotor displacement is substantially higher than that of the pad, which should be attributed to the corresponding difference in effective stiffness.

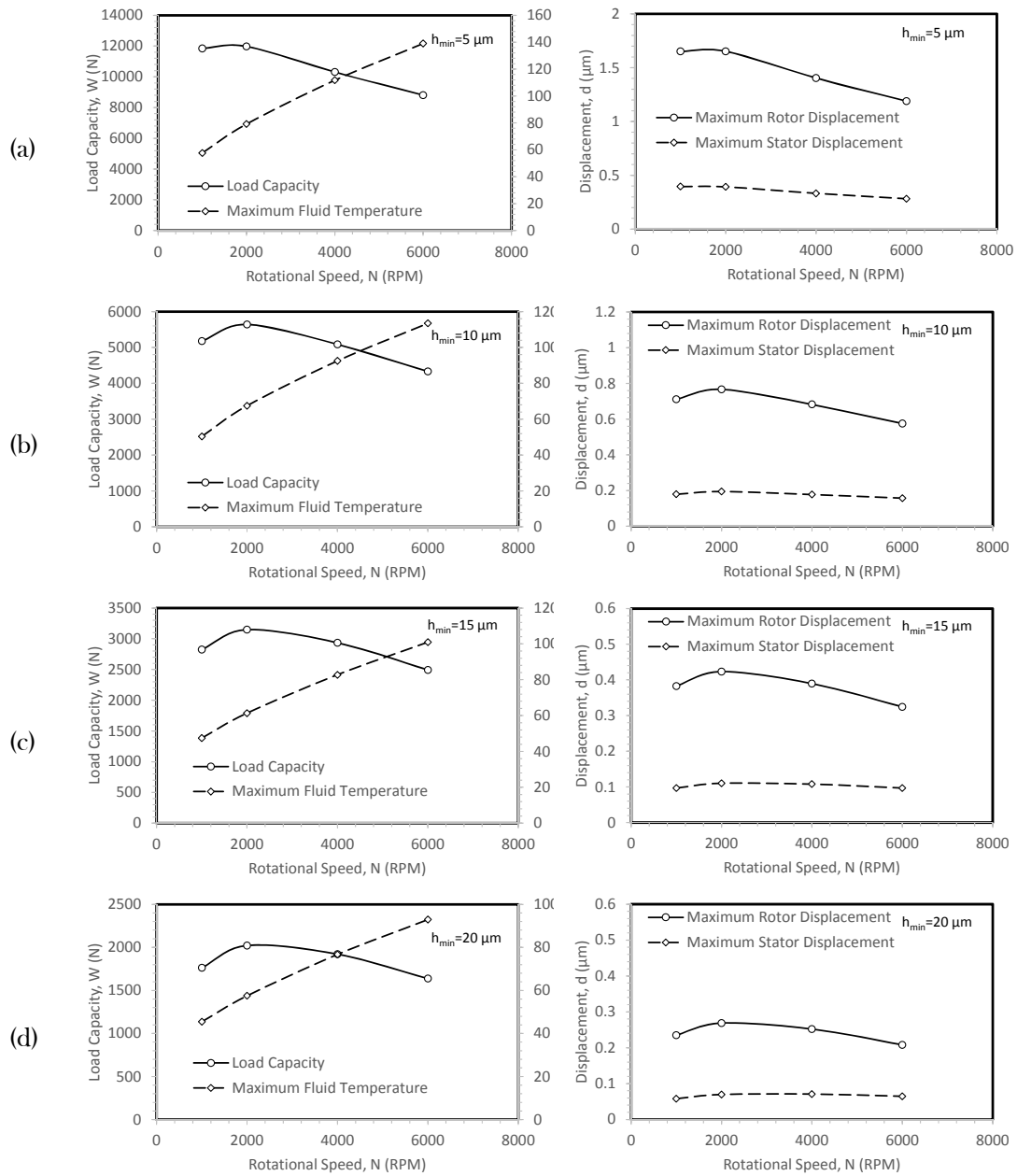


Figure 26. Load capacity, maximum fluid temperature and maximum rotor/pad displacement versus rotational speed, for four different values of minimum film thickness.

Next, the effect of rotor thickness on the performance characteristics of the bearing is quantified. Figure 6(a)-(f) presents the computed variation of load capacity and maximum fluid temperature, and the corresponding variation of maximum rotor/pad displacement, as a function of rotor thickness, for three different values of minimum film thickness; a negligible effect on load capacity, maximum fluid temperature and pad displacement is verified. On the other hand, Figure 26 (b),(d),(f) demonstrates an increase of rotor displacement with decreasing rotor thickness, qualitatively at a quadratic rate. This increase becomes very pronounced at low values of minimum film thickness.

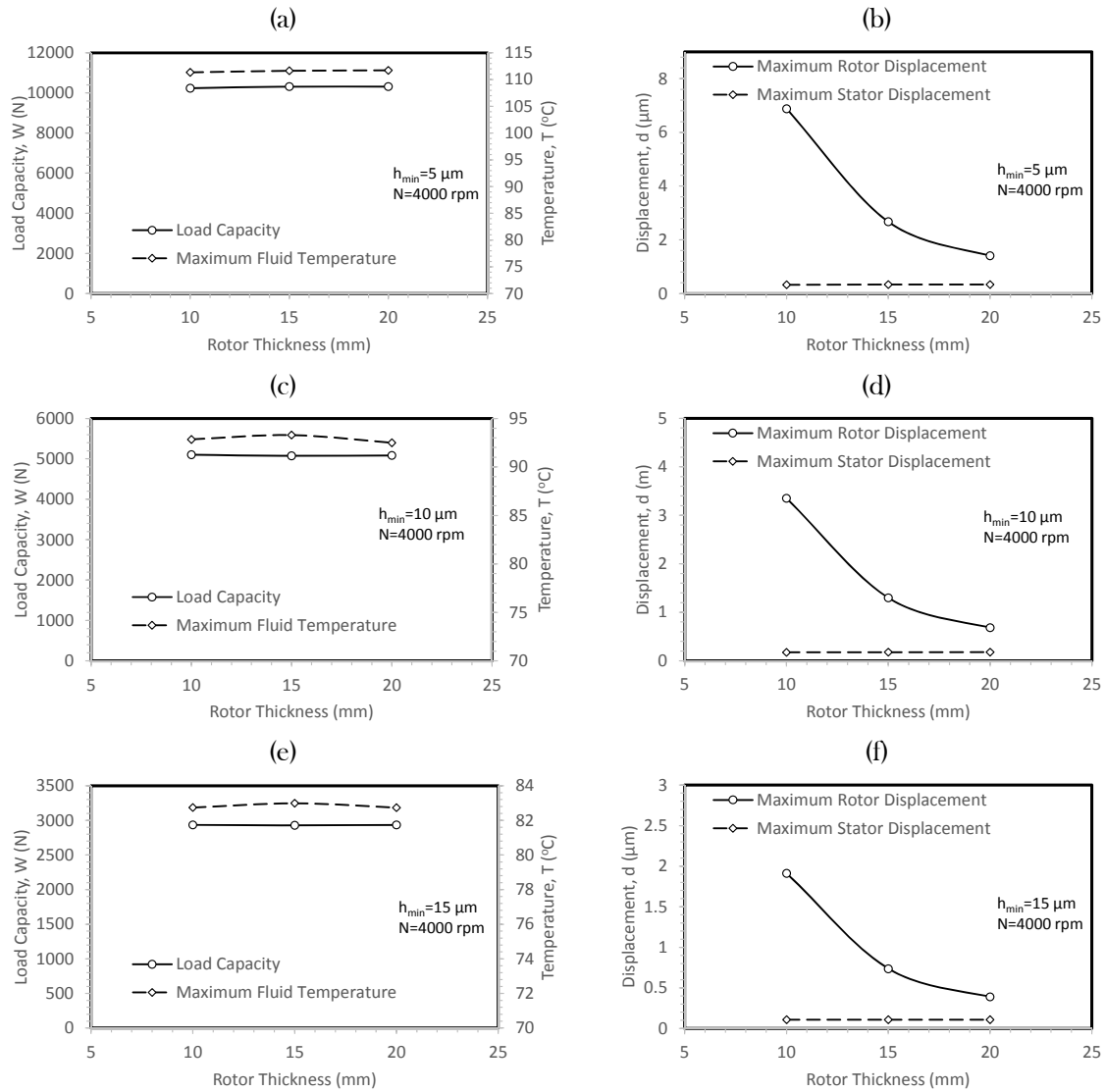


Figure 27. Load capacity, maximum fluid temperature and maximum rotor/pad displacement versus rotor thickness, for different values of minimum film thickness.

Figure 28 presents the effect of minimum film thickness on the computed pressure distribution; here, operation at $N=4000 \text{ RPM}$ for a rotor thickness of 15 mm is considered. An increase in the dimpled region is verified in all cases, with the pressure levels decreasing at increasing minimum film thickness. In Figure 29, the corresponding profiles of the rotor and pad displacement along the bearing mid-sector and the radial direction, the latter in the texture rear end region, are presented. Figure 8 demonstrates that, in the circumferential direction, both the rotor and pad exhibit maximum deformation at the texture rear end, i.e. in the region of maximum pressure. The same holds for the distribution along the radial direction for the bearing pad. On the other hand, due to the different structural boundary conditions, the rotor deformation in the radial direction increases monotonically at increasing radius.

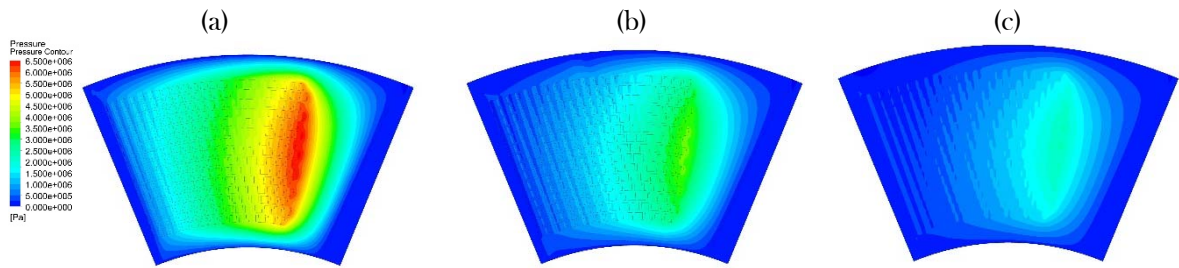


Figure 28. Rotor thickness of 15 mm, $N=4000$ RPM: Computed pressure distribution at the fluid-rotor interface, for minimum film thickness value of (a) $5 \mu\text{m}$, (b) $10 \mu\text{m}$, and (c) $15 \mu\text{m}$.

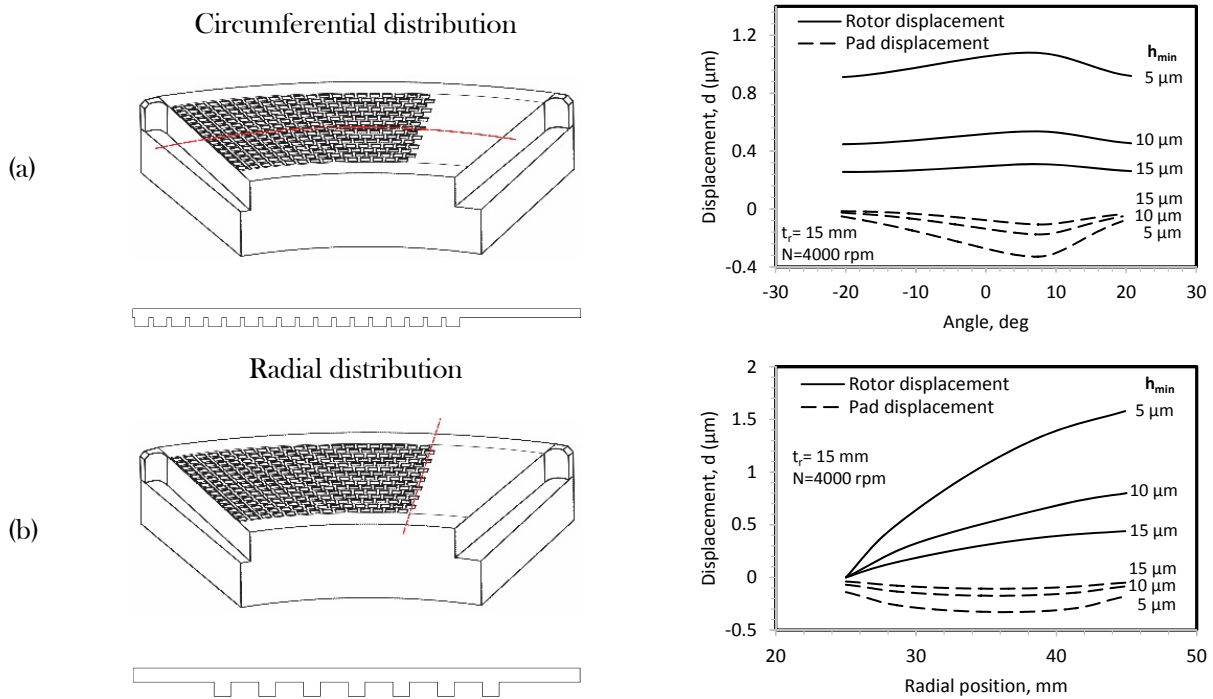


Figure 29. Profiles of rotor/pad displacement along (a) the circumferential, and (b) the radial direction, for different values of minimum film thickness. The corresponding locations are depicted in the left column sketches.

3.5. Conclusions

In the present chapter, a computational study of thermoelastohydrodynamic (TEHD) lubrication in a complex geometry textured thrust bearing has been presented. Here, a CFD-based THD analysis has been performed, along with a one-way fluid-structure interaction (FSI) coupling, yielding the displacement field of the solid parts (rotor collar, bearing pad). The main conclusions can be summarized as follows:

- The effect of oil heating on bearing performance has been confirmed to be substantial. In particular, for constant film thickness, a decrease in load capacity with bearing rotational speed is already present at values of N close to 2000 RPM.
- The variation of collar and pad deformations with bearing rotational speed follows the trend of load capacity. In the fluid-pad interface region, the pad deformation bears a pattern similar to the distribution of exerted pressure. The rotor deformation field is representative of a beam with fixed support. The maximum rotor deformation is substantially higher than that of the pad, and is a decreasing function of rotor thickness.

The present development yields a basis for detailed TEHD lubrication studies characterized by two-way FSI coupling in complex geometry thrust bearings

4. Effects of manufacturing errors on tribological characteristics of 3-D textured thrust bearings

4.1. Introduction

In the present chapter, the performance sensitivity of textured thrust bearings to manufacturing errors is investigated by means of Navier–Stokes CFD simulations, for incompressible isothermal flow. In particular, discrepancies in the size and shape of the texture geometry, as well as macroscopic errors in the stationary surface (concavity/convexity and waviness) are considered and parametrically modelled. The effects of these manufacturing errors on the bearing load carrying capacity and friction coefficient are analyzed, for representative width-to-length bearing ratios.

4.2. Bearing geometry

In Papadopoulos et al. [4], the optimization of texture geometry of three-dimensional converging thrust bearings with partial periodic rectangular texturing was considered. A sketch of such a bearing and of the corresponding 3-D channel geometry is presented in Figure 30. The channel consists of a moving smooth wall (rotor) and a stationary textured wall (stator). In the case of a smooth (untextured) stator, pressure buildup is only feasible for converging channels. The presence of dimples can result in substantial pressure buildup, even for parallel or slightly diverging bearings.

In the present study, the three-dimensional parametric CAD model of Papadopoulos et al. [4] has been generalized, to include different types of manufacturing errors. The bearing height varies from the inlet height $H_1(x = 0)$ to its value H_0 at the outlet ($x = L$). H_0 and H_1 are controlled by the convergence ratio, $k = (H_1 - H_0) / H_0$, taking positive, zero or negative values, for converging, parallel and diverging sliders, respectively. The value of minimum film thickness, H_{min} , depends on the actual stator geometry. Here, H_{min} is assumed in all cases constant. The length of the bearing is controlled by the non-dimensional parameter $= L / H_{min}$; here is equal to 100, as in [4]. The bearing width, B , is controlled by the ratio B / L .

Part of the stationary wall is textured with rectangular dimples. For all cases, an untextured part (sill) at the inlet, of length equal to 1/100 of the total length, i.e. $l_{ui} = 0.01$, is considered. The untextured length at the bearing outlet is variable, controlled by the non-dimensional parameter l_{uo} . The textured part exhibits N periodic texture cells. Each texture cell is defined by the cell length, L_c , the dimple length, L_d , and the dimple depth, H_d , see Figure 1(b). These dimensional geometric parameters are controlled by the texture density, ρ_T , and the relative dimple depth, s .

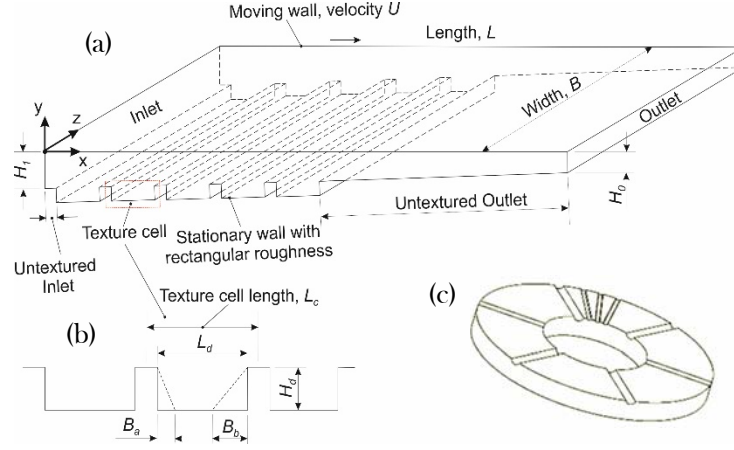


Figure 30. (a) Three-dimensional textured converging slider geometry (parallel slider for $H_1=H_0$, diverging slider for $H_1<H_0$). (b) Geometry of dimples. (c) Typical thrust bearing application with partial texturing. (Papadopoulos et al. [4])

Due to manufacturing errors, the stator surface can be characterized by several types of deviations from the nominal surface, see e.g. Kwan and Post [41]. In the present work, a number of manufacturing errors is considered, resulting in the following deviations from a nominal design, see Figure 2:

- (i) Discrepancy in convergence ratio.
- (ii) Discrepancy in normalized dimple depth.
- (iii) Discrepancy of dimple shape from the reference orthogonal form.
- (iv) Concavity / convexity of the base stator surface.
- (v) Waviness of the base stator surface in the streamwise direction.

Discrepancy of dimple shape from the reference orthogonal form is accounted for by considering trapezoids, inscribed in the reference (rectangular) dimple geometry. The discrepancy is quantified by the non-dimensional parameters b_a , b_b , defined in terms of lengths B_a , B_b , (see Figure 30), as follows:

$$b_a = B_a/L_d \quad (12)$$

$$b_b = B_b/(L_d - B_a) \quad (13)$$

Concavity/convexity (in the streamwise direction) is defined by first considering two points, with a vertical coordinate C with respect to a local coordinate system, with origin at the mid-point of the base (planar) stator surface. Positive values of C correspond to concave, while negative values to convex manufactured surfaces. For a given value of C , a parabola between the stator end-points is readily defined, thus determining the convex/concave stator base surface, see Figure 2. Parameter C is controlled by the non-dimensional parameter $c = C / H_{min}$.

Waviness in the streamwise direction is considered sinusoidal, defined in terms of wavenumber n , amplitude A and phase angle ϕ . In the present work three different values of n are considered, $n = 1, 3, 5$. Amplitude A_w is controlled by the normalized waviness amplitude $a_w = A_w/H_{min}$. The local difference between the manufactured and the nominal film thickness is defined as follows:

$$\Delta H(x) = a_w H_{min} \sin(2\pi n x / L + \phi), n = 1, 3, 5$$

4.3. Computational model

In the present chapter, the flow is considered isothermal, and cavitation is not accounted for. The conservation equations for unsteady incompressible and isothermal flow, with zero gravitational and other external body forces, are, the mass conservation equation and the momentum equations as described before.

Those equations have been solved with the CFD code ANSYS CFX. From dimensional analysis, it follows that, for given geometry, the flow dynamics depends on the Reynolds number, Re , defined here in terms of the moving wall velocity and the minimum film thickness, H_{min} . In the present study, $Re=1$, a value representative of bearing applications. Results are presented in non-dimensional form.

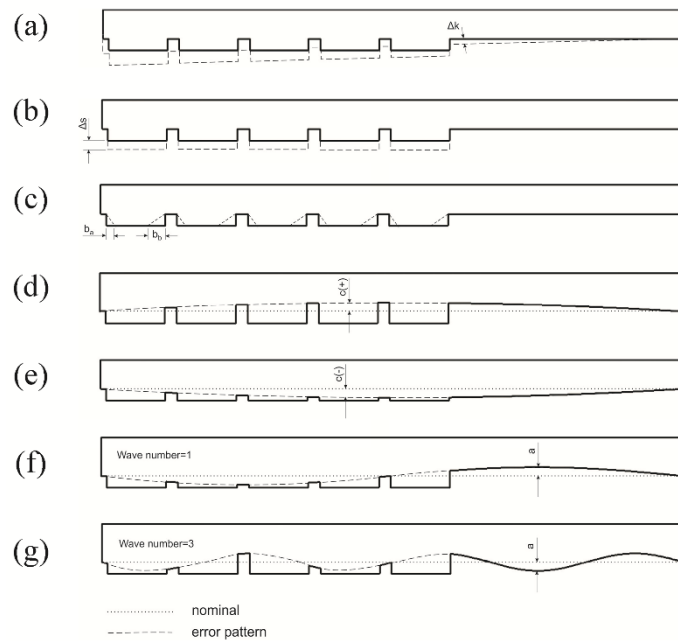


Figure 31. Sketch of textured sliders with manufacturing errors in the stator: (a) discrepancy in convergence ratio, (b) discrepancy in dimple depth, (c) discrepancy in dimple shape from orthogonal, (d) stator concavity, (e) stator convexity, (f) stator waviness with wavenumber $n=1$, and (g) stator waviness with wavenumber $n=3$.

Typical 3-D meshes generated consist of approximately 600,000 hexahedral finite volumes. Here, the density of grids utilized is similar to that of the validated grids in Papadopoulos et al. [4].

The bearing walls are considered impermeable. The bottom wall is stationary. The upper wall is assumed to be moving at a constant velocity U (parallel to the x axis), $(x, y = 0, z) = U$. No-slip conditions are assumed at both walls. The inlet and outlet surfaces of the bearing are considered openings: the pressure is assumed constant, with the same value $p=0$ prescribed at both boundaries, while a Neumann boundary condition is assumed for the velocity. At the bearing sides, $z=0, B$, an outflow condition is prescribed, prohibiting fluid entrance to the computational domain.

All simulations were initialized from zero velocity and pressure fields. For $Re=1$, the governing equations were integrated for a total non-dimensional time ($\frac{tU}{H_{min}}$) of 10, with a time step of 0.05. In all cases, convergence to steady state was verified by monitoring the computed velocity and pressure at a number of representative points of the flow domain.

The shear (friction) force and the vertical force exerted to the rotor are calculated at steady state by integrating the shear stress, τ , and pressure, p , respectively, over the rotor surface:

$$F_{fr} = \int_0^B \int_0^L \tau \, dx \, dz, F_{fp} = \int_0^B \int_0^L p \, dx \, dz = W \quad (14)$$

The friction coefficient is defined as:

$$f = F_{fr} / F_p \quad (15)$$

4.4. Geometry parameters of optimized reference textured bearings

In the present study, the bearings considered are characterized by manufacturing errors, with respect to reference optimal stator texture patterns. These optimal patterns correspond to maximum load carrying capacity, and are the outcome of the optimization study of Papadopoulos et al. [4], see Table 1.

B/L ratio	Convergence ratio, k	Untextured outlet length, l_{uo}	Non-dimensional dimple depth, s
inf	0	0.364	0.695
	$k = k_{opt} = 0.75$	0.307	0.412
1.0	0	0.447	0.412
	$k = k_{opt} = 1.1$	0.567	0.308
0.5	0	0.532	0.372
	$k = k_{opt} = 1.31$	0.705	0.380

Table 1. Parameters of optimal texture geometry reported in Papadopoulos et al. [4]: values of l_{uo} and s , for different values of k and B/L . These values are derived for constant values of dimple number and dimple density, $N=5$ and $\rho=0.83$. For a given value of B/L , a convergence ratio of $k = k_{opt}$ corresponds to the global maximum in load carrying capacity.

4.5. Computational results

The tribological performance of thrust bearings is expressed by the two main integral parameters, the normalized load carrying capacity, W^* , and the friction coefficient, f . To assess the performance of textured thrust bearings with manufacturing errors, a detailed computational investigation is performed, for representative values of the slider width-to-length ratio, B/L , equal to infinity (2-D sliders), 1, and 0.5. For all three values of B/L , two values of convergence ratio are considered, equal to $k=0$ (parallel sliders) and $k = k_{opt}$, see Table 1. The types of manufacturing errors considered are depicted in Figure 2. The following ranges are selected for the parameters quantifying manufacturing errors:

- Discrepancy in convergence ratio: $\Delta k = [-0.2, 0.2]$.
- Discrepancy in normalized dimple depth: $\Delta s = [-0.3, 0.3]$.
- Discrepancy of dimple shape from the reference orthogonal form: $b_a = [0, 0.3]$, $b_b = [0, 0.3]$.
- Concavity / convexity of the base stator surface in the streamwise direction: $c = [-0.3, 0.3]$.
- Waviness of the base stator surface in the streamwise direction: $n = 1, 3, 5$; $a = [0, 0.3]$.

Figure 32 and Figure 33 present the effect of different types of manufacturing errors on the load carrying capacity and friction coefficient of infinite width, parallel, and converging (with $k = k_{opt}$) bearings. The following observations can be made:

- As in parallel sliders pressure buildup is only due to texturing, an increase in convergence ratio, k , results in increased load carrying capacity (Figure 32(a)), due to the addition of the wedge effect; correspondingly, a decrease in k (diverging slider) results in a decrease in W^* . Nonetheless, a decrease in k of the order of 0.1 can be tolerated if a decrease in W^* of 30% can be accepted. The monotonic increase in W^* with k results in a

corresponding monotonic decrease in friction coefficient, see Figure 32(f). In converging sliders of infinite width, a variation of k around k_{opt} by $\Delta k = \pm 0.2$ results in a small decrease of less than 2% in W^* (Figure 4(a)). The friction coefficient is a slowly decreasing function of k (Figure 33(f)).

- In parallel sliders, the variation of dimple depth around the optimum by $\pm 30\%$ of H_{min} results in a maximum decrease in W^* of less than 10% (Figure 32(b)). A corresponding increase of less than 10% is found for the friction coefficient (Figure 32(g)). For converging bearings with $k = k_{opt}$, the effect of varying s around the optimum value is even milder (Figure 33(b,g)).
- In the presence of both concavity and convexity, the load carrying capacity of parallel sliders decreases (Figure 32(c)), with a corresponding increase in friction coefficient (Figure 32(h)). The decrease in W^* is more pronounced for $c > 0$ (concave sliders), exceeding 35% at $c = 0.3$. For converging bearings with $k = k_{opt}$, the effects of varying parameter c are similar for $c < 0$ (convex sliders); however, a non-negligible increase in W^* is gained for $c > 0$ (concave sliders), see Figure 33(c). The effect on the friction coefficient is the same as in parallel sliders.
- In parallel sliders, the presence of waviness of $n=1$ (one full sine pattern) has a positive effect on performance, in terms of both W^* and f . Specifically, an improvement of approximately 20% is obtained for both parameters for a non-dimensional wave amplitude $a=0.2$, see Figure 3(d,i). However, performance deteriorates at increasing n values. The trends are the same for converging bearings with $k = k_{opt}$ (Figure 33(d,i)).
- In parallel sliders, the deviation of the dimple shape from an orthogonal one, expressed by parameters b_a and b_b , is not significant, see Figure 32(e,j). The effects are even smaller for converging bearings with $k = k_{opt}$ (Figure 33(e,j)).

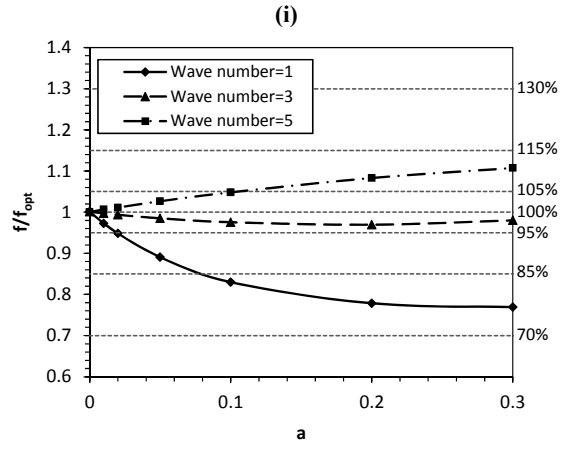
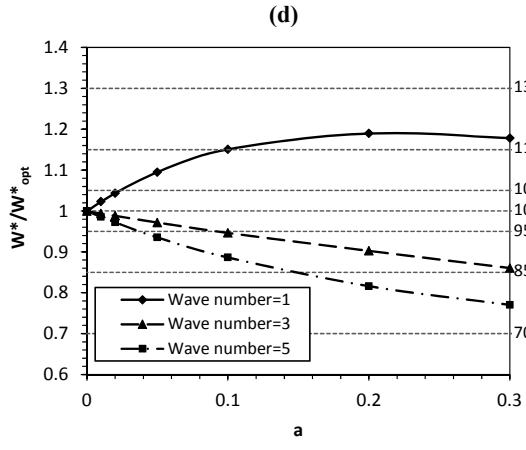
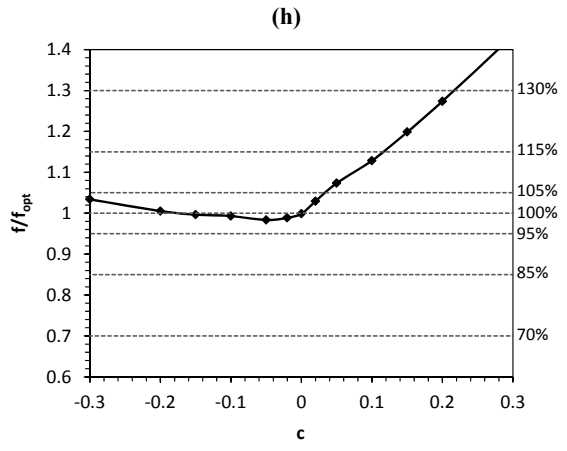
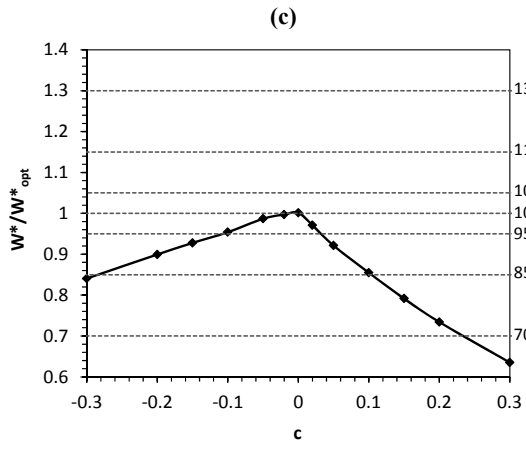
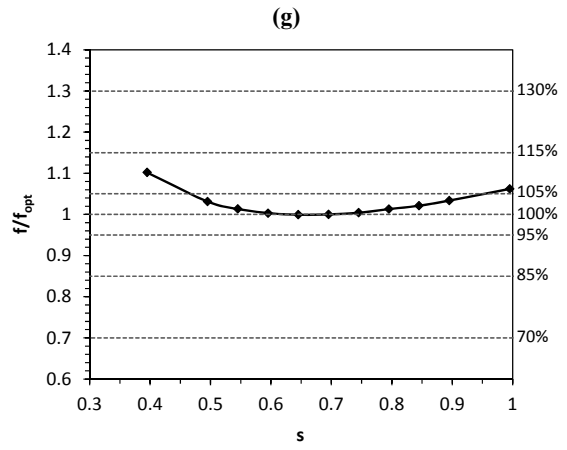
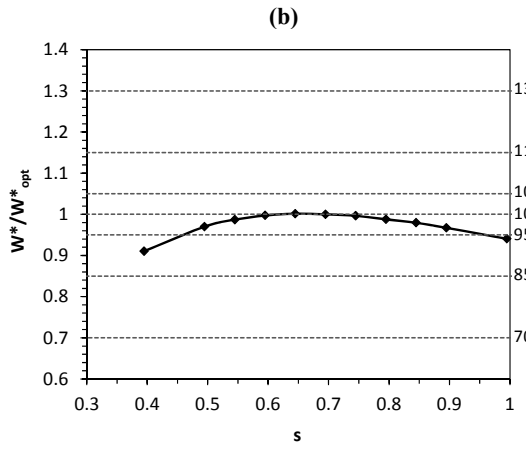
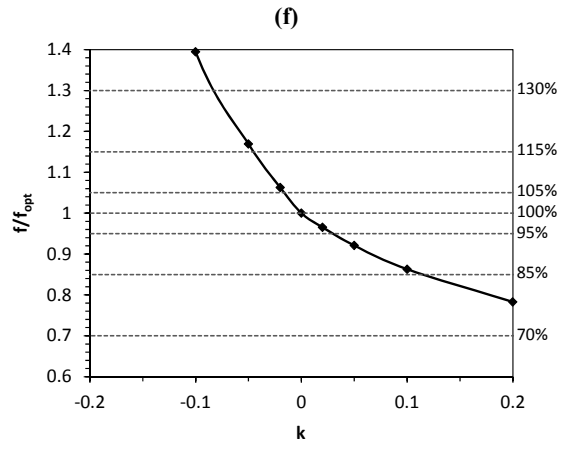
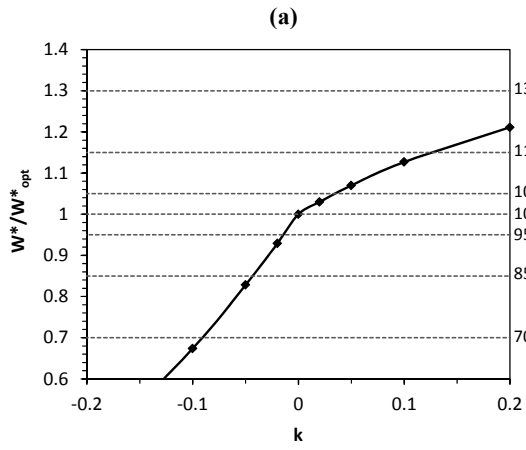
For finite width bearings, variation of the parameters characterizing manufacturing errors results in the same trends in W^* and f as those found for infinite width sliders; nonetheless, the deviations from the nominal design are more pronounced. These deviations increase at decreasing B/L (Figure 34 - Figure 37). It is noted that the results presented in Figure 34 - Figure 37 can be used for prescribing tolerances, in the design of textured thrust bearings.

To illustrate the effects of different manufacturing errors on the pressure buildup mechanism of infinite width sliders, Figure 38 - Figure 40 are presented. Figure 38 presents pressure distributions of parallel and converging bearings with $k = k_{opt} = 0.75$, corresponding to nominal designs, as well as to strongly concave/convex stators. Figure 38(a) shows that concavity results in substantial pressure buildup in the dimpled region, with a sharp decrease in the untextured part; the latter can be attributed to the locally diverging slider geometry. On the other

hand, the effect of convexity is less pronounced in the dimpled region, however, the pressure decrease is smoother in the untextured part. Consequently, the two pressure integrals (load carrying capacities) exhibit comparable values. In both cases, the values of pressure maximum as well as of the pressure integral are lower than the corresponding of the nominal design (Figure 32(c)). In converging sliders (Figure 38(b)), concavity results in a pressure rise, which is higher than that of the nominal design (similar conclusions are drawn for untextured concave sliders in Abramovitz [34]); correspondingly, the pressure integral is increased, see Figure 33(c). A less pronounced increase and a corresponding decreased pressure integral are attained for the case of a convex infinite slider.

The effect of stator waviness on the pressure distribution is presented in Figure 39. It is found that, for both parallel and converging bearings, the presence of one full sine pattern results in increased overall pressure buildup, which explains the increased load capacity values of Figure 32(d) and Figure 33(d). Pressure buildup becomes less pronounced at increasing wavenumber values.

Figure 40 presents the effect of parameters b_a and b_b , on the pressure distribution and flow structure (streamline patterns). It is found that slight inclination of both dimple legs leads to a marginal increase in pressure buildup (Figure 40(a)), due to the decrease in the size of the corresponding recirculation zones (Figure 40(b)). However, a substantial increase in b_a and b_b results in decreased pressure buildup, due to a decrease of the equivalent (useful) dimple length.



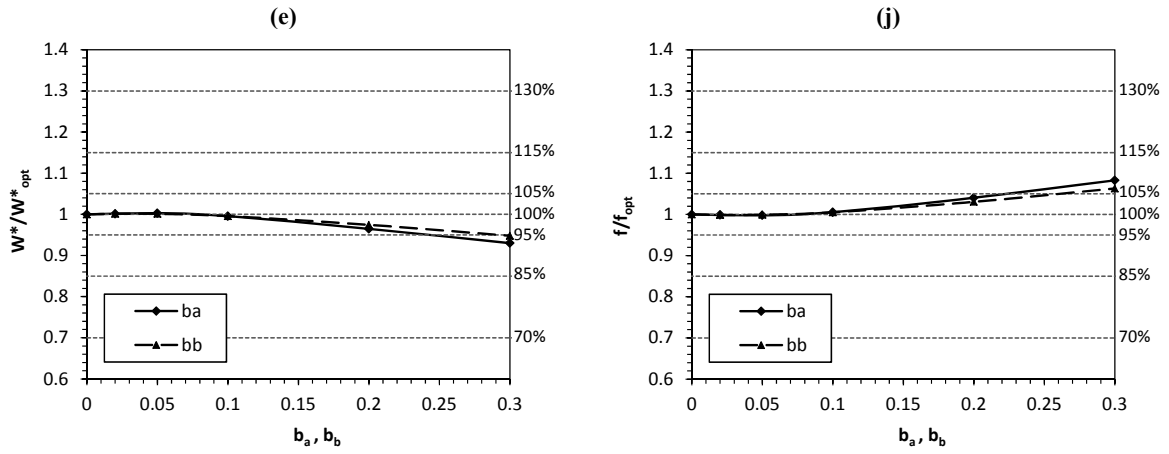
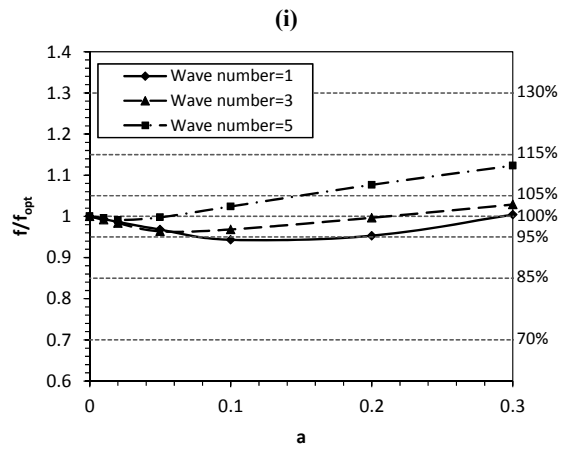
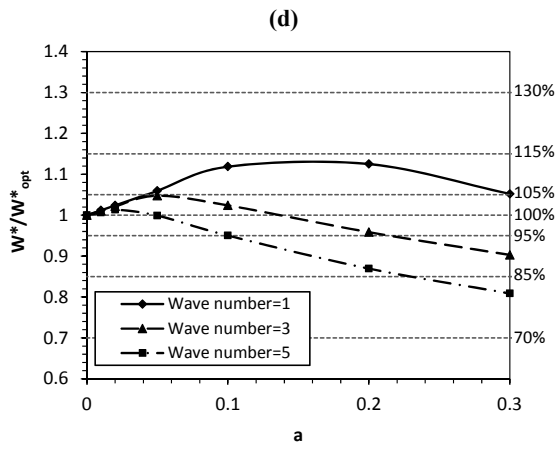
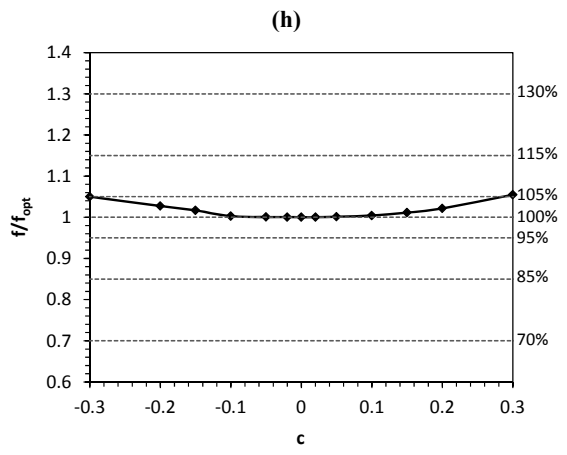
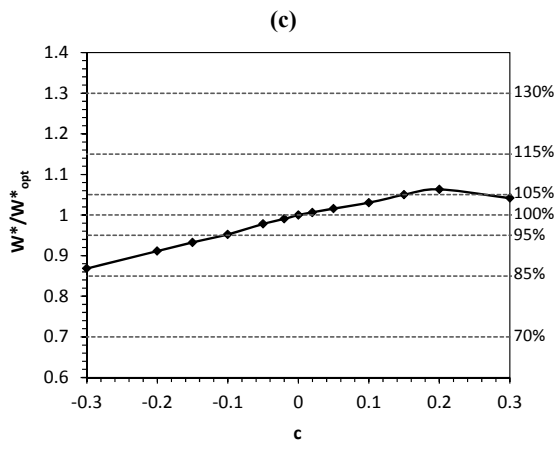
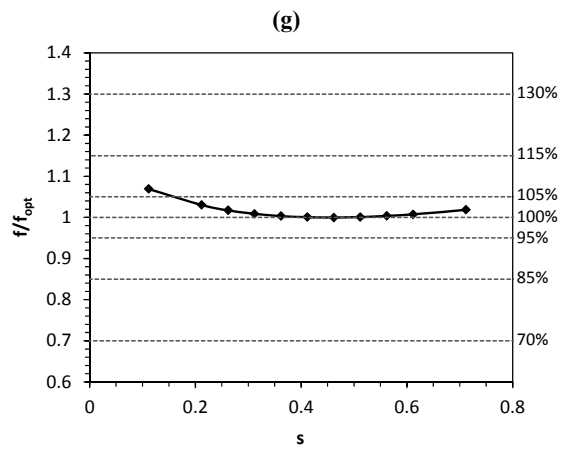
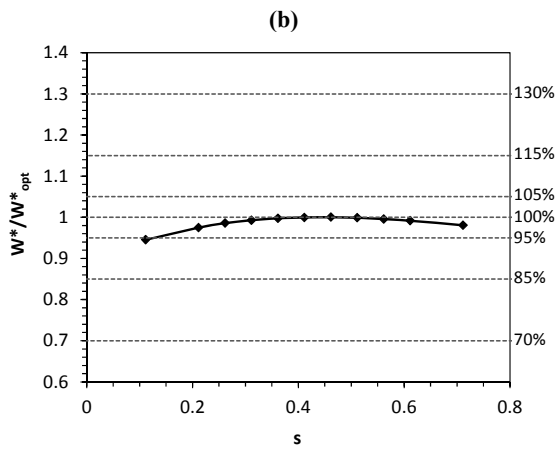
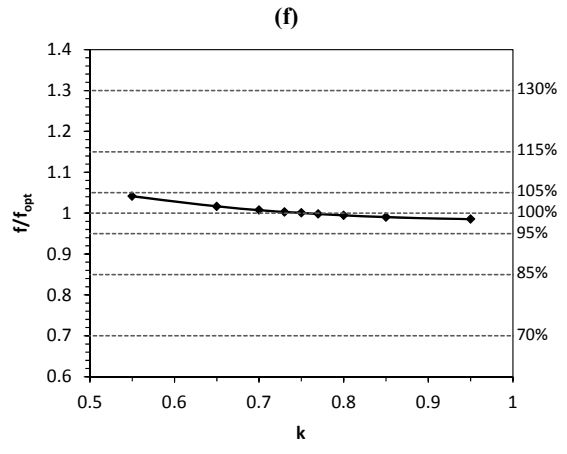
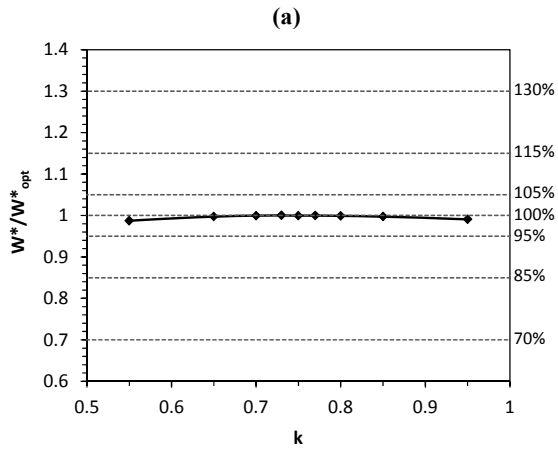


Figure 32. $B/L = \inf, k = 0$: Normalized values of load carrying capacity (W / W_{opt}) and friction coefficient (f / f_{opt}) for different parameters expressing manufacturing errors: (a),(f) discrepancy in convergence ratio; (b),(g) discrepancy in normalized dimple depth; (c),(h) concavity (+) / convexity (-); (d),(i) waviness; (e),(j) discrepancy from orthogonal dimple shape.



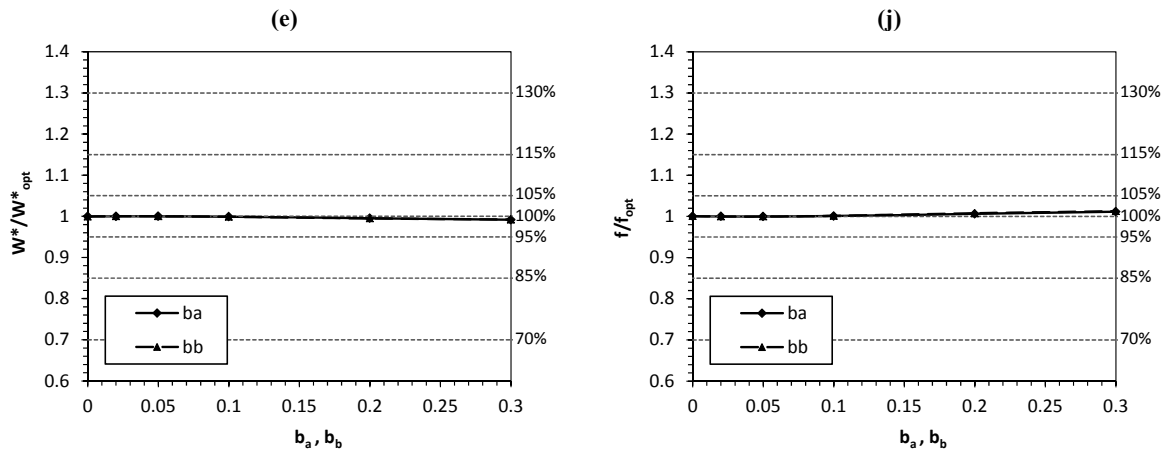
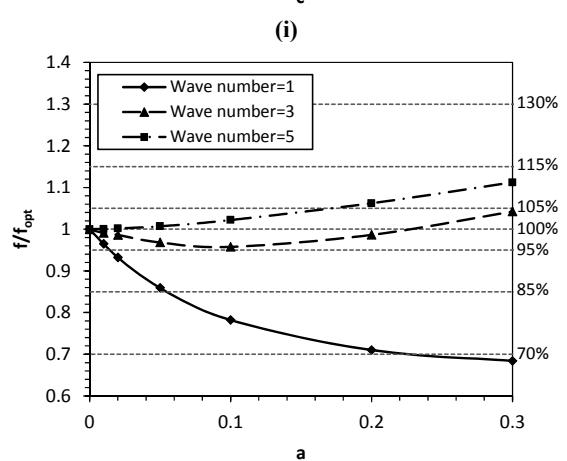
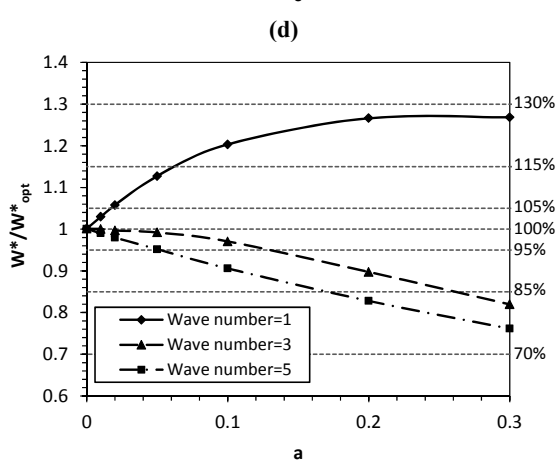
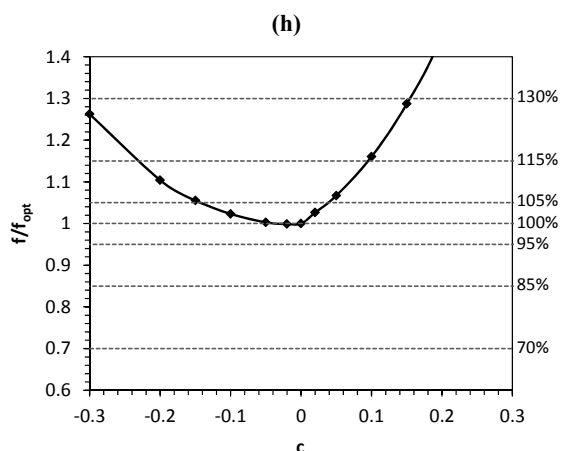
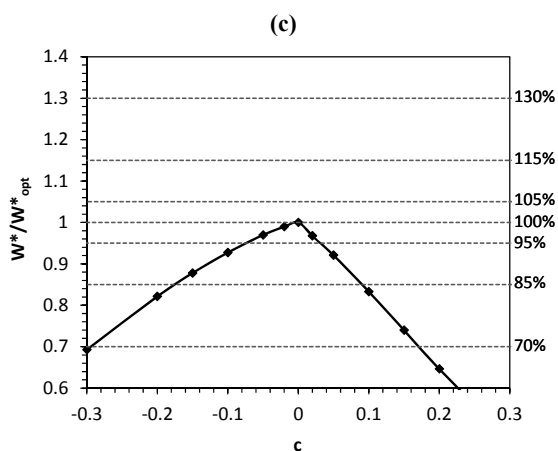
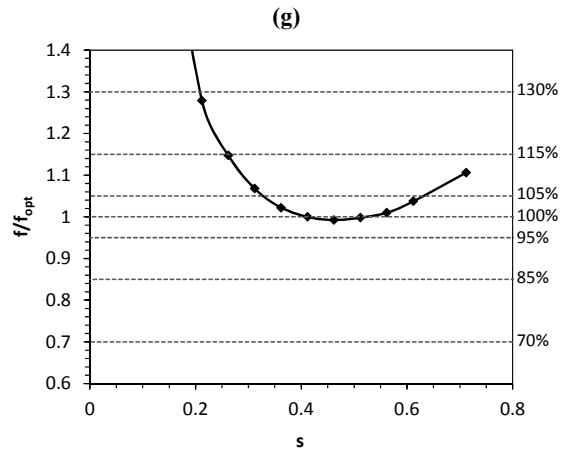
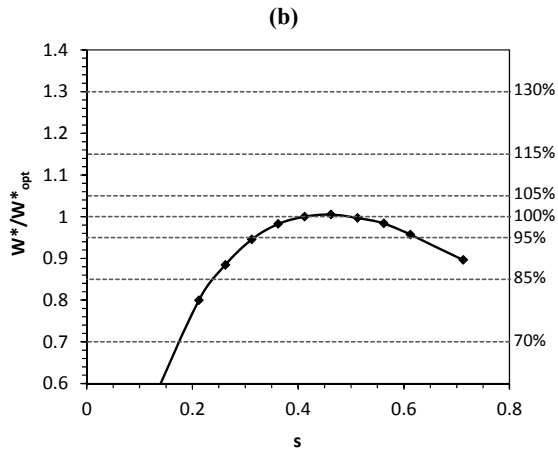
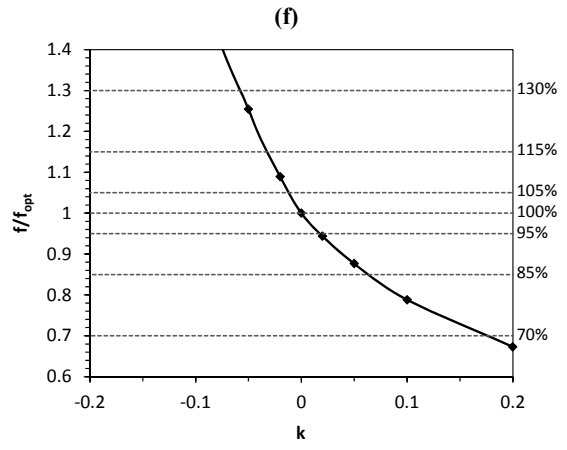
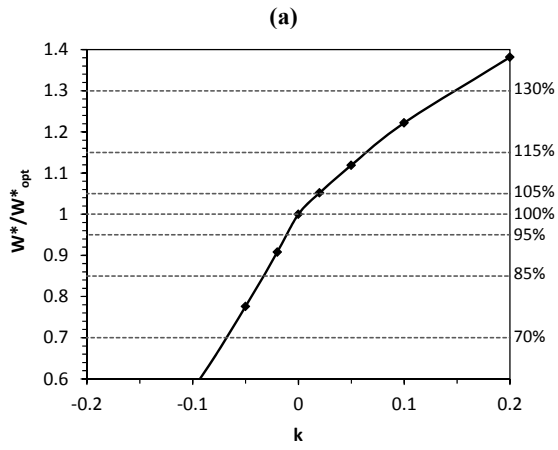


Figure 33. – $B/L = \text{inf}$, $k = k_{opt}=0.75$. Normalized values of load carrying capacity (W / W_{opt}) and friction coefficient (f / f_{opt}) for different parameters expressing manufacturing errors: (a),(f) discrepancy in convergence ratio; (b),(g) discrepancy in normalized dimple depth; (c),(h) concavity (+) / convexity (-); (d),(i) waviness; (e),(j) discrepancy from orthogonal dimple shape.



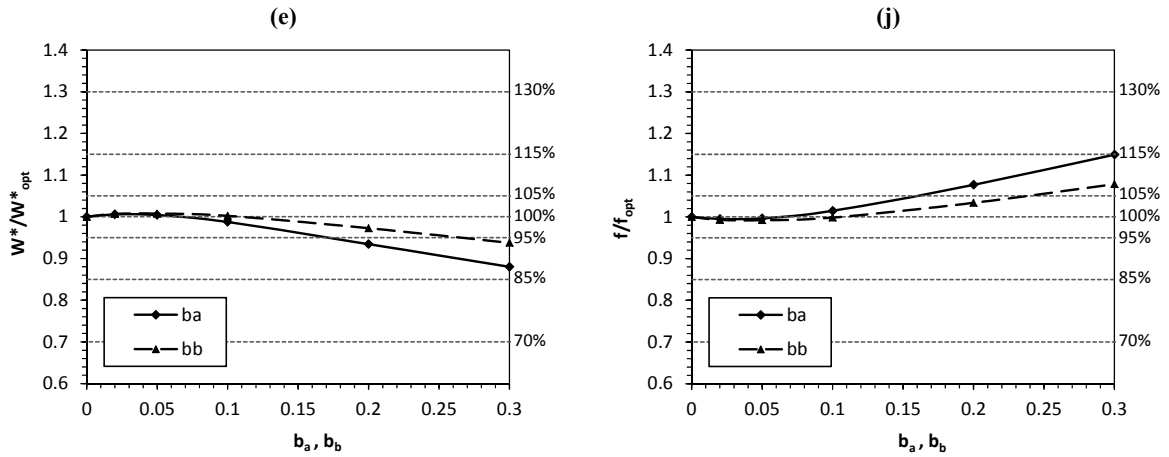
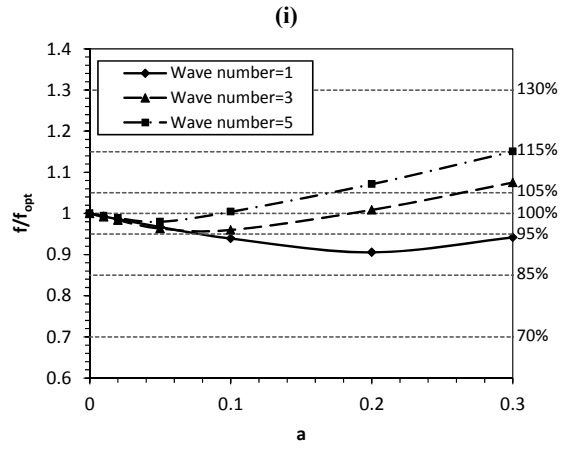
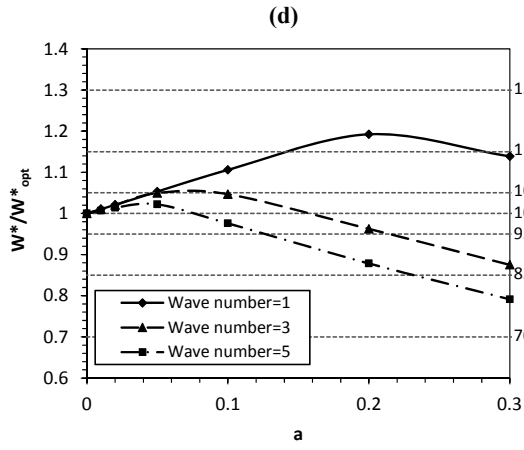
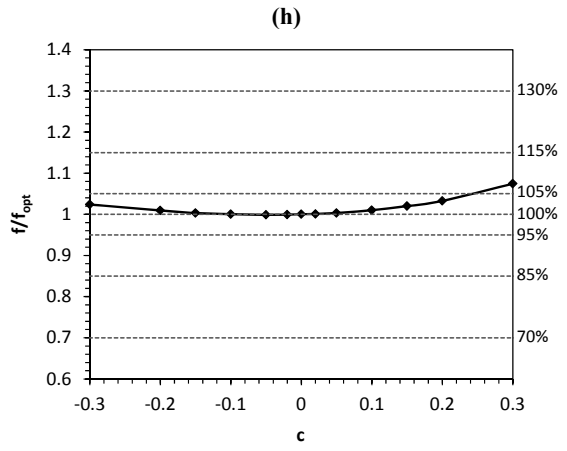
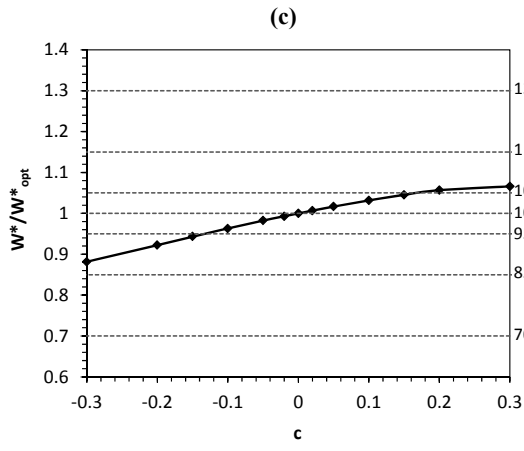
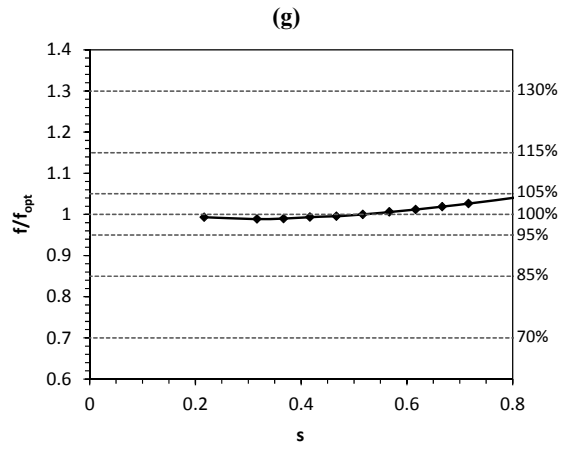
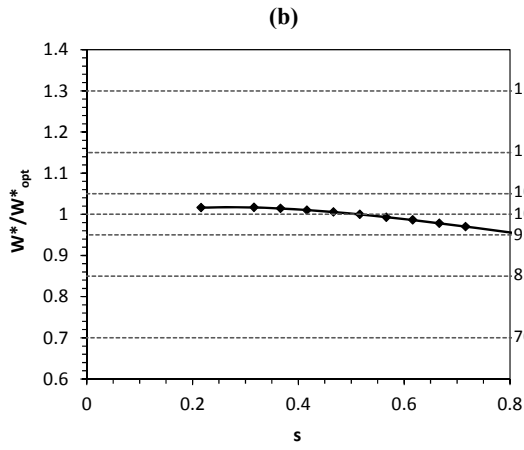
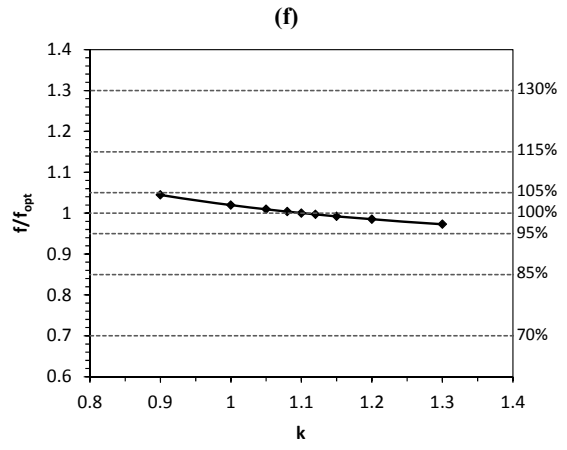
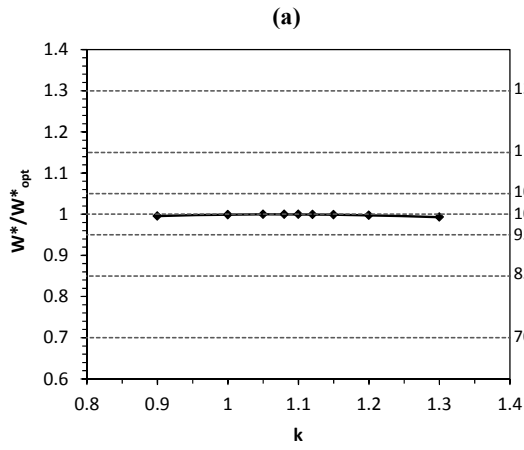


Figure 34. $B/L = 1.0$, $k = 0$. Normalized values of load carrying capacity (W / W_{opt}) and friction coefficient (f / f_{opt}) for different parameters expressing manufacturing errors: (a),(f) discrepancy in convergence ratio; (b),(g) discrepancy in normalized dimple depth; (c),(h) concavity (+) / convexity (-); (d),(i) waviness; (e),(j) discrepancy from orthogonal dimple shape.



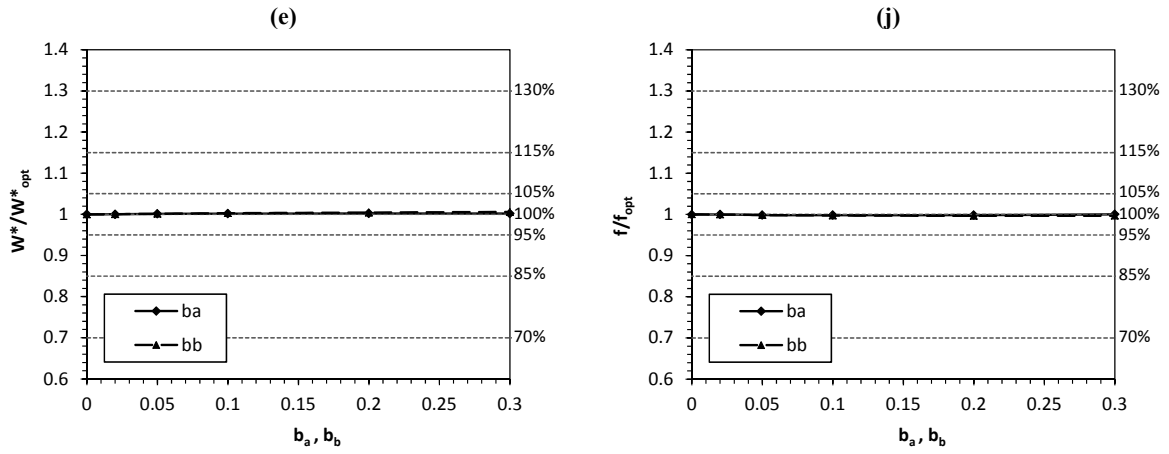
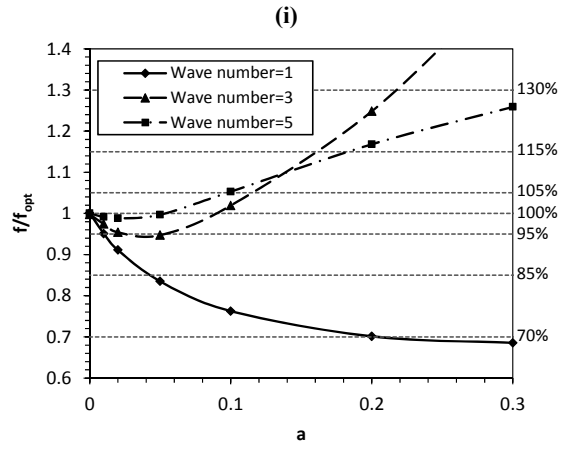
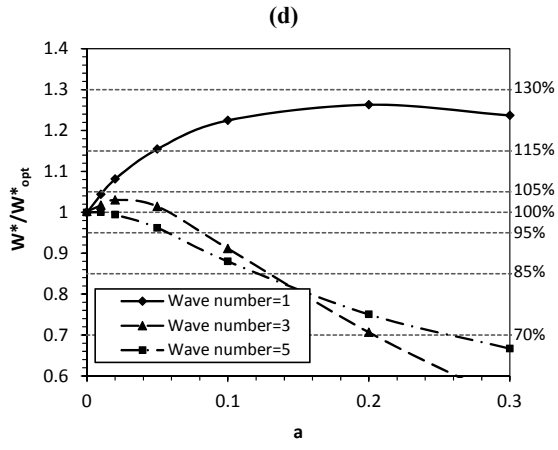
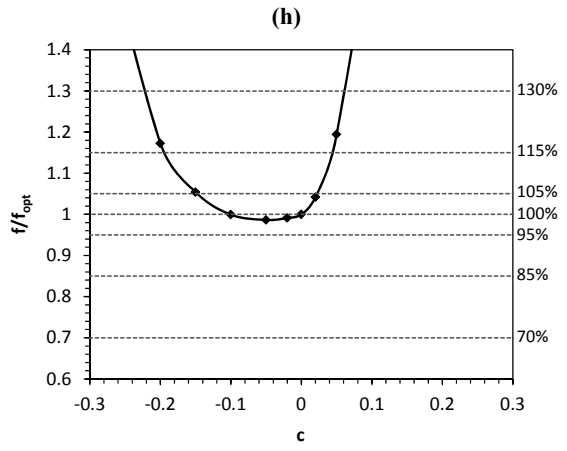
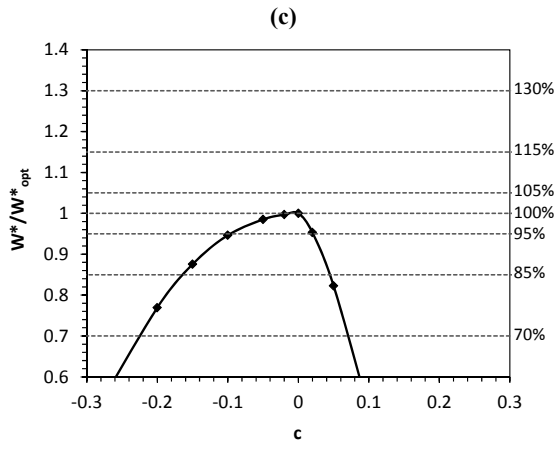
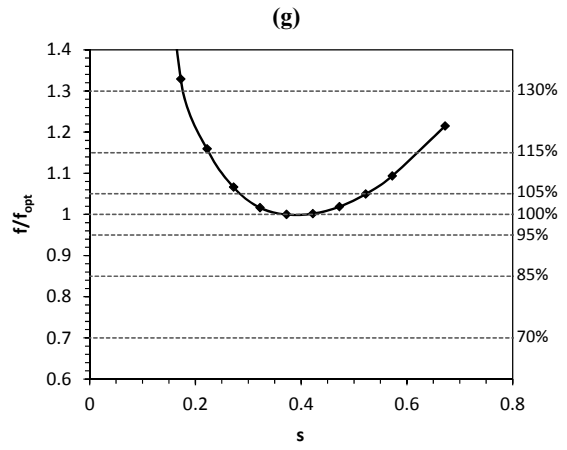
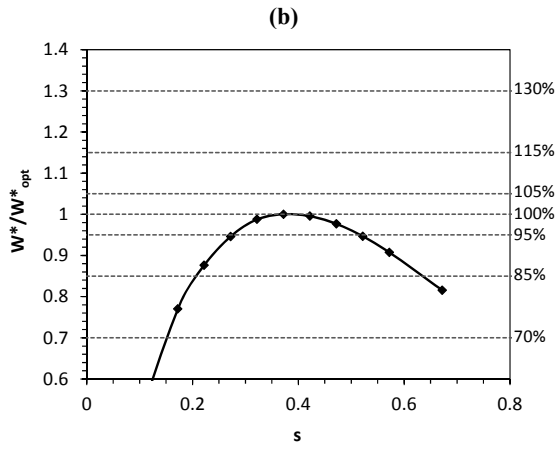
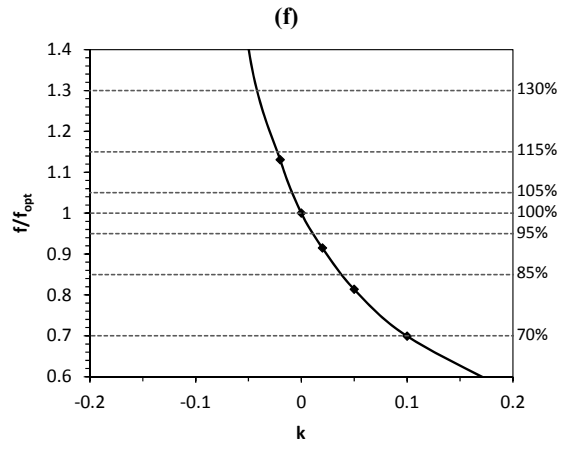
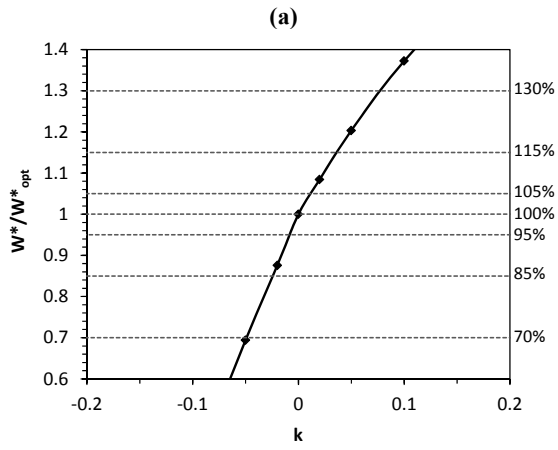


Figure 35. $B/L = 1.0$, $k = k_{opt} = 1.1$. Normalized values of load carrying capacity (W / W_{opt}) and friction coefficient (f / f_{opt}) for different parameters expressing manufacturing errors: (a),(f) discrepancy in convergence ratio; (b),(g) discrepancy in normalized dimple depth; (c),(h) concavity (+) / convexity (-); (d),(i) waviness; (e),(j) discrepancy from orthogonal dimple shape.



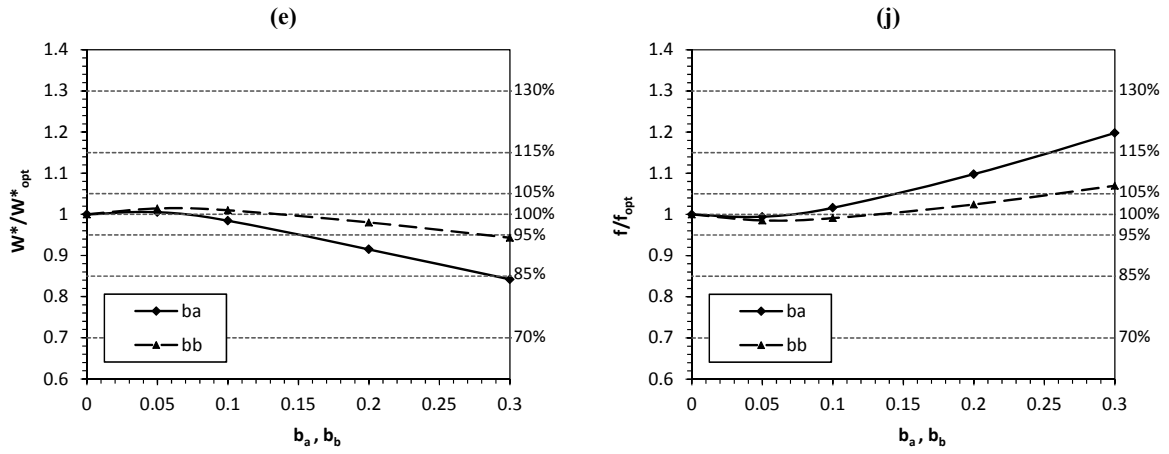
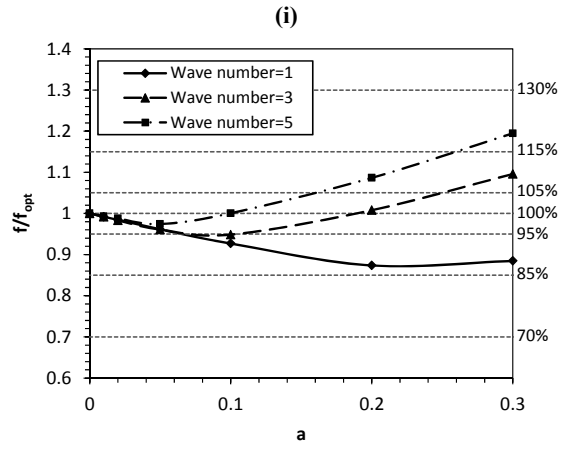
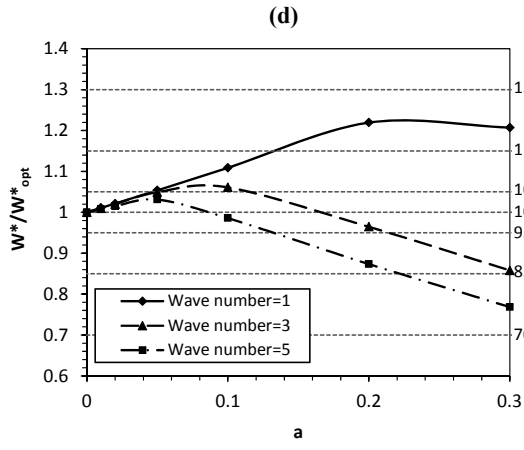
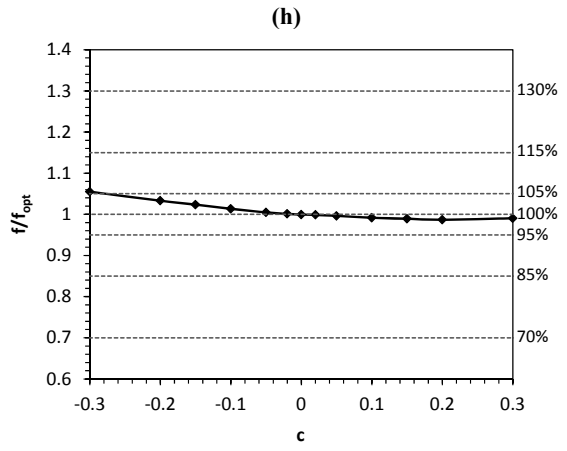
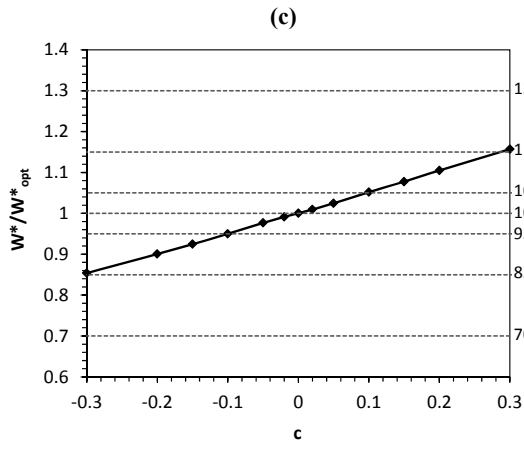
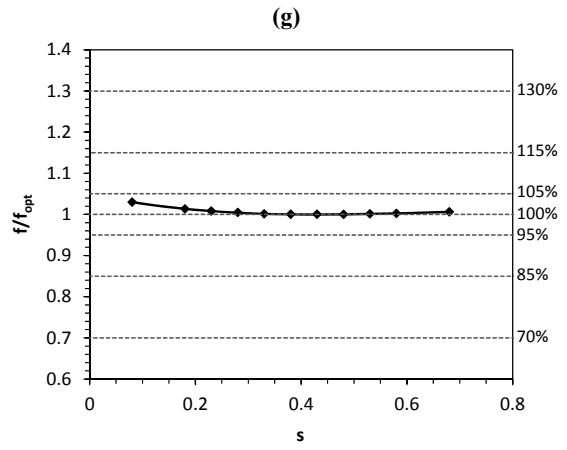
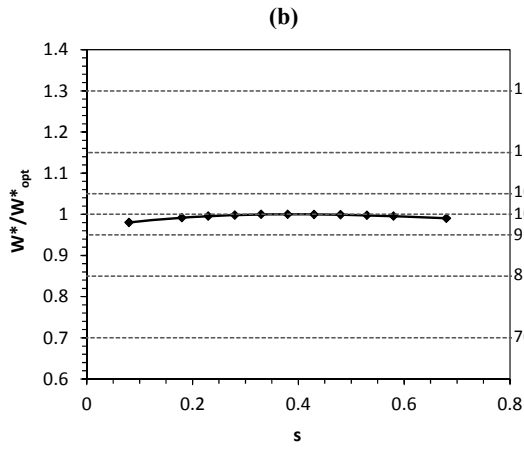
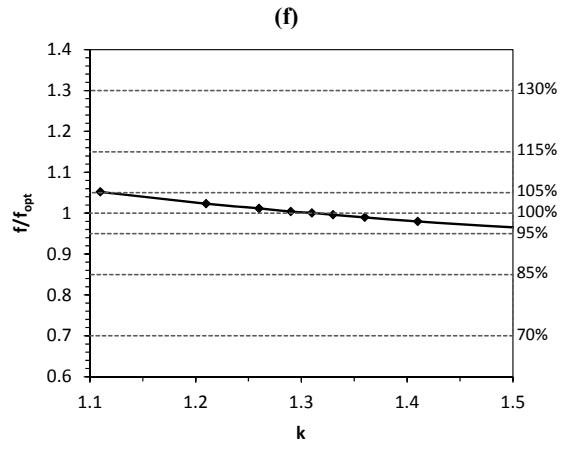
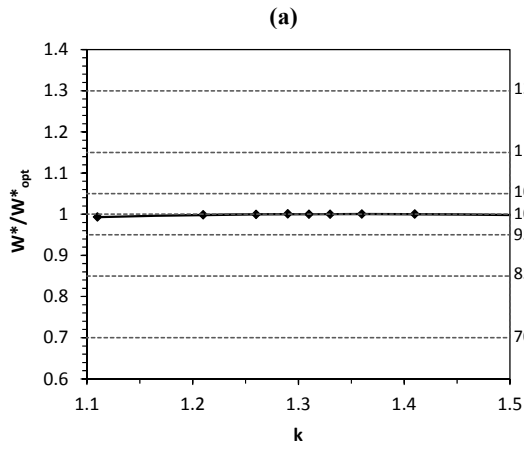


Figure 36. $B/L = 0.5$, $k = 0$. Normalized values of load carrying capacity (W / W_{opt}) and friction coefficient (f / f_{opt}) for different parameters expressing manufacturing errors: (a),(f) discrepancy in convergence ratio; (b),(g) discrepancy in normalized dimple depth; (c),(h) concavity (+) / convexity (-); (d),(i) waviness; (e),(j) discrepancy from orthogonal dimple shape.



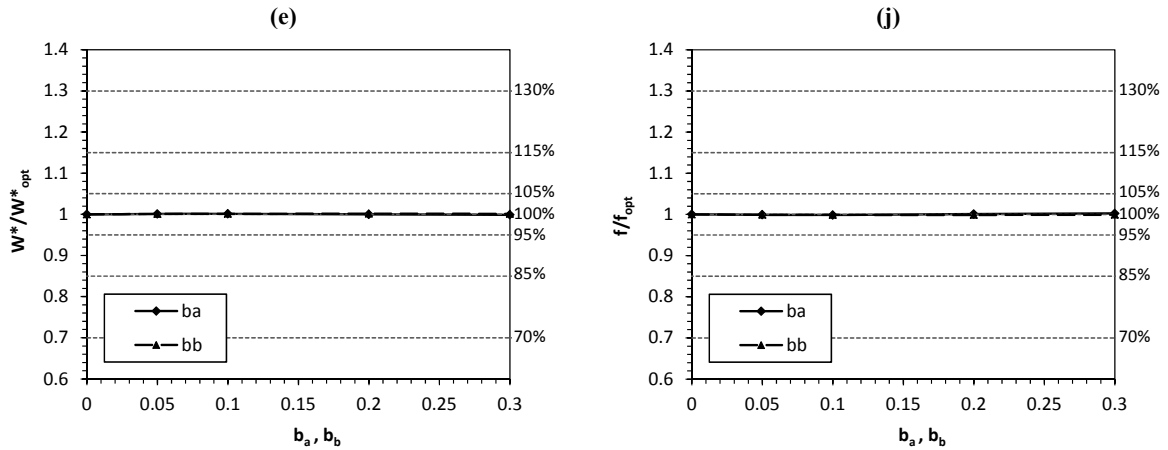


Figure 37. $B/L = 0.5$, $k = k_{opt} = 1.31$. Normalized values of load carrying capacity (W / W_{opt}) and friction coefficient (f / f_{opt}) for different parameters expressing manufacturing errors: (a),(f) discrepancy in convergence ratio; (b),(g) discrepancy in normalized dimple depth; (c),(h) concavity (+) / convexity (-); (d),(i) waviness; (e),(j) discrepancy from orthogonal dimple shape.

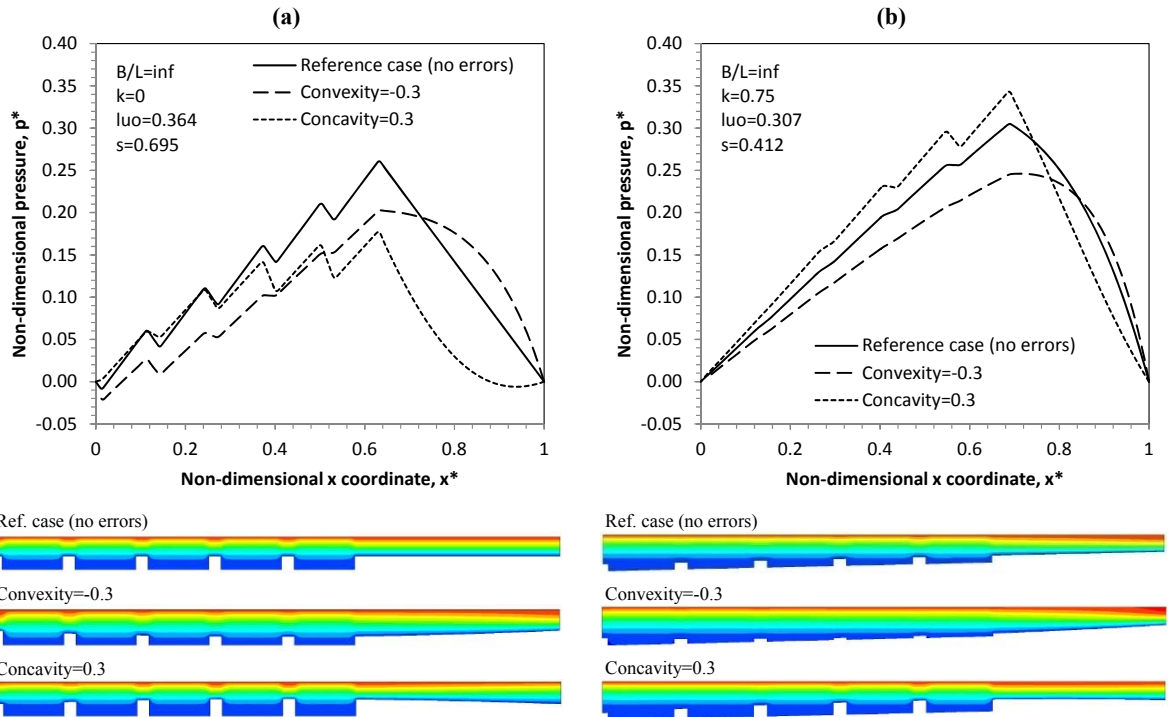


Figure 38. $B/L = \text{inf}$: Distributions of non-dimensional pressure on the moving wall, and color-coded contours of non-dimensional streamwise velocity, for: (a) a parallel bearing, and (b) a converging bearing with $k = k_{opt} = 0.75$, for nominal designs ($c=0$), convex sliders with $c=-0.3$, and concave sliders with $c=0.3$.

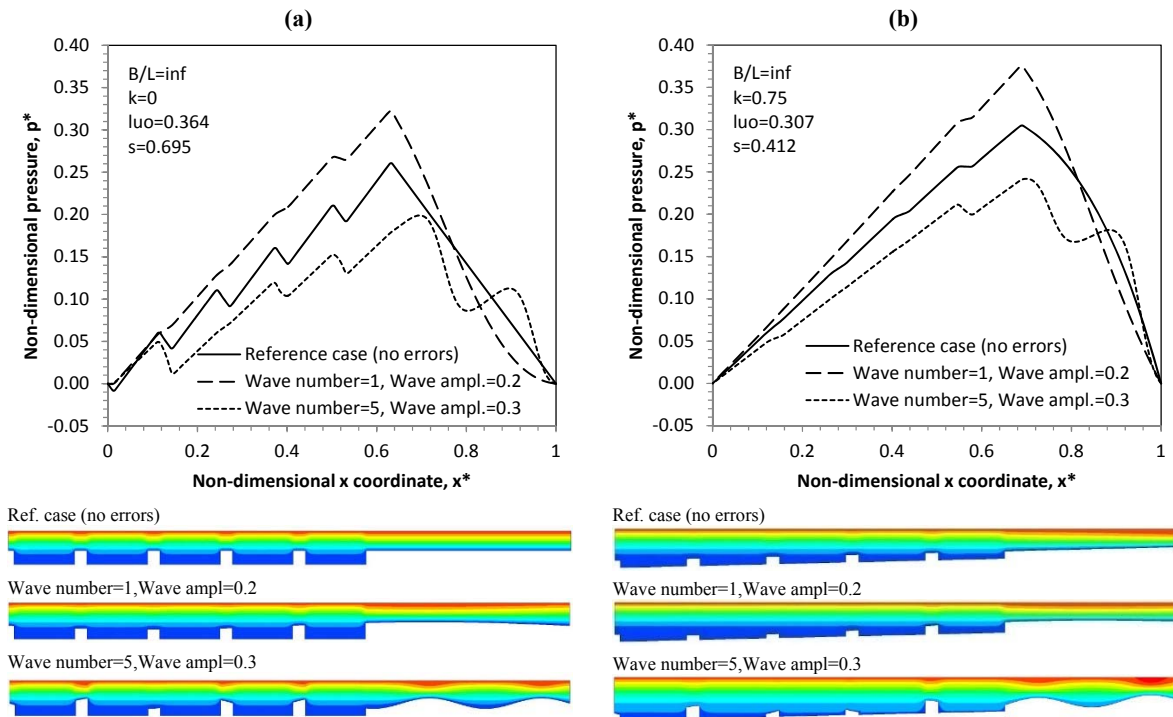


Figure 39. $B/L = \text{inf}$: Distributions of non-dimensional pressure on the moving wall, and color-coded contours of non-dimensional streamwise velocity, for: (a) a parallel bearing, and (b) a converging bearing with $k = k_{opt} = 0.75$, for nominal designs ($\alpha=0$), and wavy sliders with different wave number and non-dimensional amplitude values.

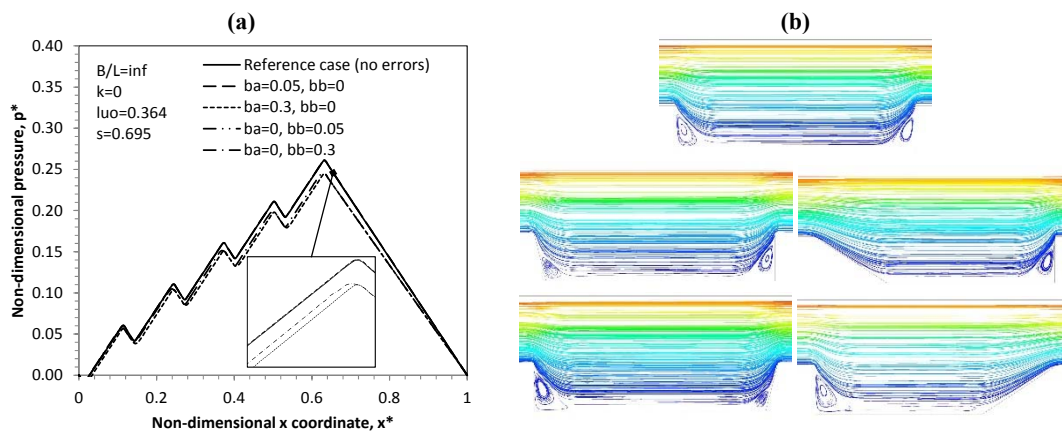


Figure 40. $B/L = \text{inf}$, $k=0$: (a) Distributions of non-dimensional pressure on the moving wall for different values of parameters b_a and b_b . (b) Corresponding streamlines in the region of the first dimple, coded with velocity magnitude.

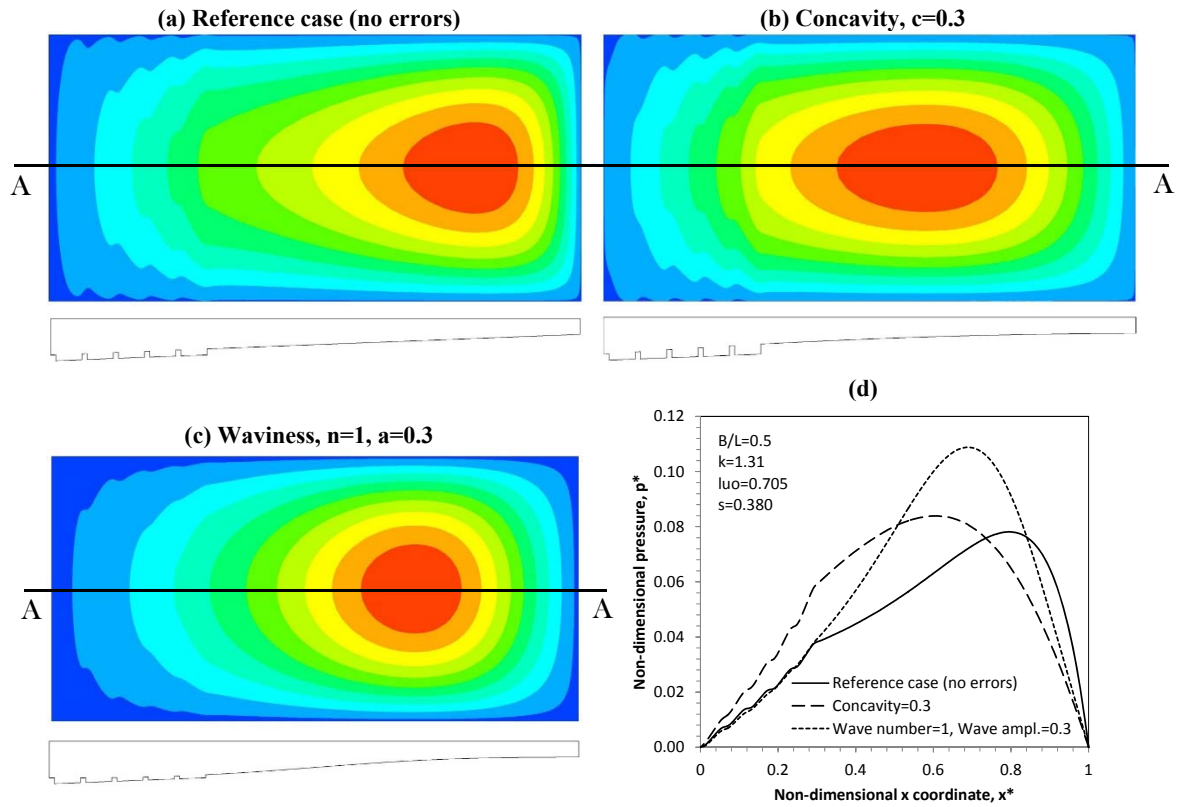


Figure 41. $B/L = 0.5$, $k = k_{opt} = 1.31$: Color-coded contours of non-dimensional pressure on the moving wall of the slider, for: (a) nominal optimal slider; (b) a concave slider with $c=0.3$; (c) a wavy slider with $n=1$ and $a=0.3$. (d) Corresponding distributions of non-dimensional pressure on the moving wall symmetry line (A-A).

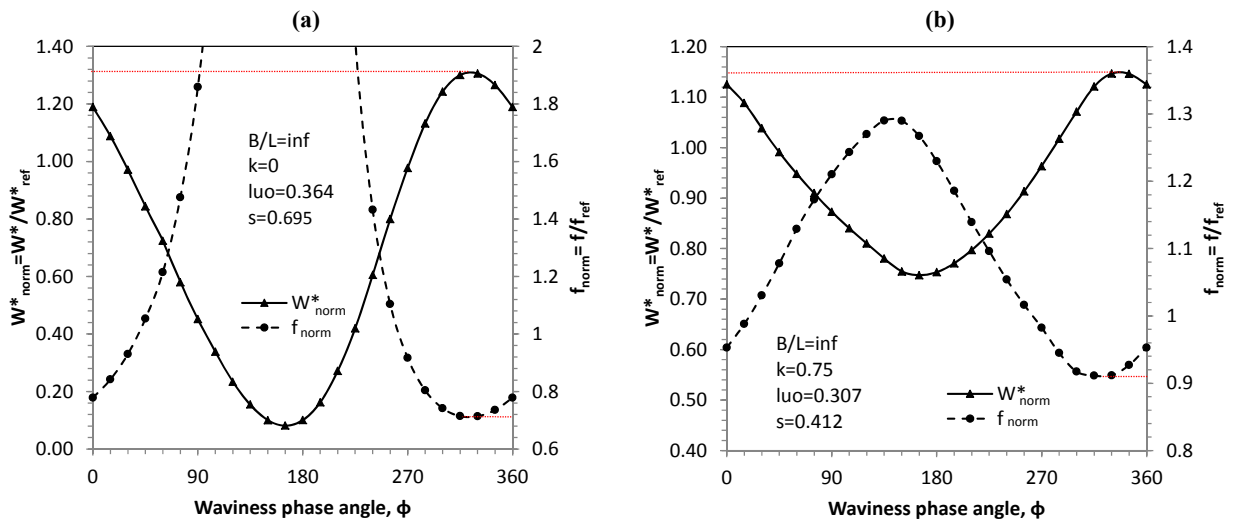


Figure 42. $B/L = \text{inf}$: Normalized values of load carrying capacity and friction coefficient, versus waviness phase angle, ϕ , for optimally textured sliders with: (a) $k=0$, (b) $k=0.75$.

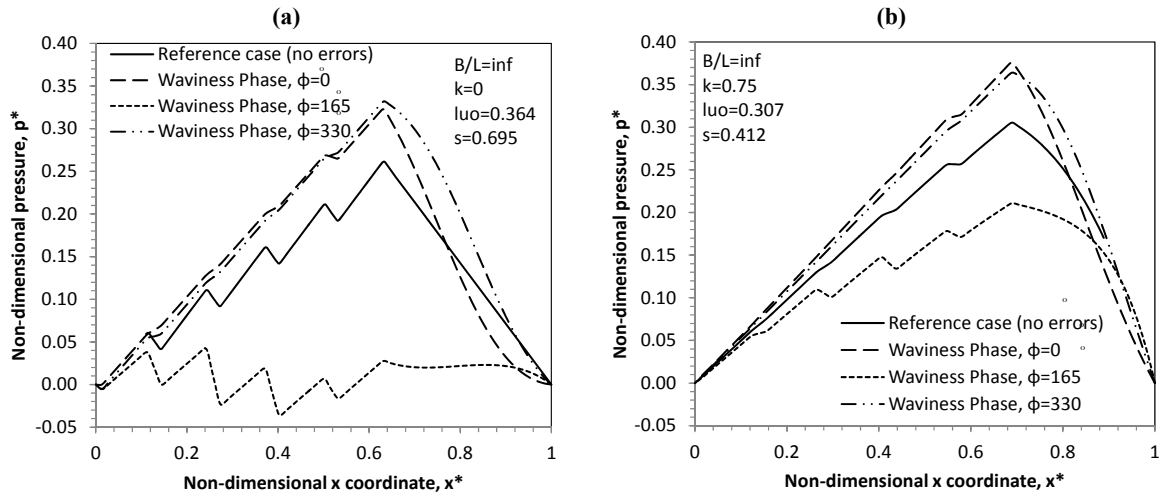


Figure 43

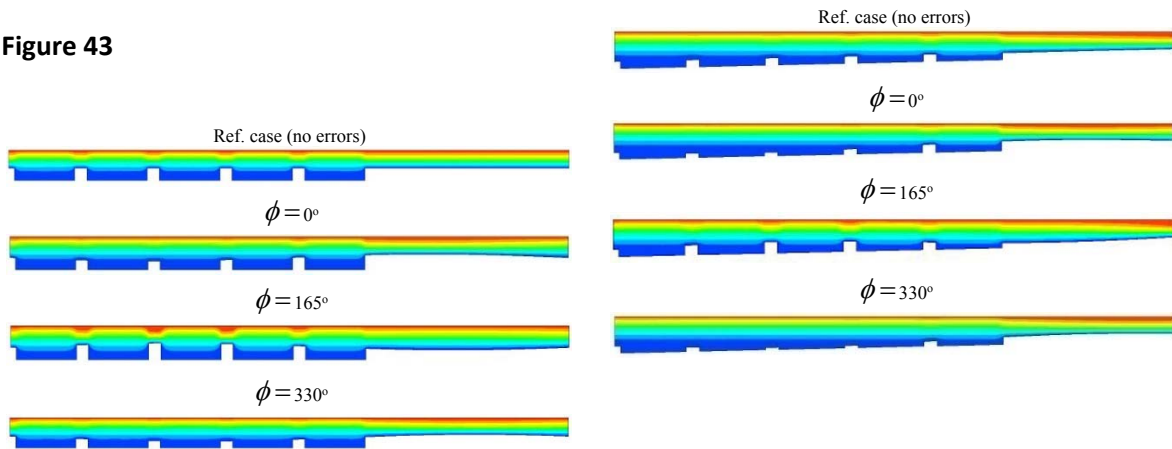


Figure 44. $B/L = \text{inf}$: Distributions of non-dimensional pressure on the moving wall, and color-coded contours of non-dimensional streamwise velocity, for: (a) a parallel bearing, and (b) a converging bearing with $k = k_{opt} = 0.75$. Here, nominal designs ($\alpha=0$), and wavy sliders with $\alpha=0.2$ and different waviness phase angles, ϕ , are considered.

The effects of finite bearing width on pressure distribution is presented in Figure 41, for representative cases with $B/L=0.5$. Here, converging sliders with $k = k_{opt}$, of nominal design, as well as two sliders with manufacturing errors (the latter characterized by substantially improved performance) are considered. Figure 41(a),(d) shows that, in the case of nominal design, a substantial pressure buildup is present, for the textured, as well as for a large portion of the untextured part. Figure 41(b),(d) shows that, for a concave slider with $c=0.3$, an increased pressure buildup slope is attained for the textured part, resulting in an substantial increase of the pressure integral (see Figure 37(c) for $c=0.3$). Finally, Figure 41(c),(d) demonstrates that in the case of a wavy stator with $n=1$ and $a=0.3$, a substantial increase in pressure buildup is attained for a large portion of the untextured part; this increases substantially the maximum pressure value, as well as the pressure integral (by approximately 20%, see Figure 37(d) for $a=0.3$).

The effect of waviness phase angle, ϕ , on the performance of infinitely wide thrust bearings, in terms of load carrying capacity and friction coefficient, is presented in Figure 42. Here, optimally

textured parallel sliders, as well as converging sliders with $k = k_{opt} = 0.75$, are considered. The value of phase angle is varied in the range of 0-360 degrees. For parallel sliders (Figure 42(a)), a strong dependence of load carrying capacity and friction coefficient on phase angle is observed. In particular, compared to the reference case of a slider without errors, the introduction of waviness with different values of phase angle can lead to sliders with higher load carrying capacity (up to approximately 32%, for $\phi = 330^\circ$) and substantially lower load carrying capacity (by approximately 90%, for $\phi = 165^\circ$). The dependence of friction coefficient on phase angle follows the reverse trend. For converging sliders (Figure 42(b)), the effects are qualitatively similar to those of parallel sliders, but substantially less pronounced. In particular, a maximum increase in load carrying capacity (in comparison to the reference converging slider without errors) of approximately 15% is observed for $\phi = 330^\circ$, while a maximum decrease of approximately 25% is observed for $\phi = 165^\circ$. Figure 44(a,b) presents pressure distributions of parallel and converging sliders with nominal design (no errors), as well as wavy sliders with different waviness phase angles. In the case of $\phi = 0^\circ$ and $\phi = 330^\circ$, the introduction of waviness results in a substantial increase of pressure buildup in the dimpled region of the stator, followed by a sharp decrease in the untextured region, leading overall to a substantial increase in load carrying capacity (pressure integral) for parallel and converging sliders. In the case of $\phi = 165^\circ$, the performance is severely deteriorated for parallel sliders, since the pressure buildup in the dimpled area is very low; nonetheless, in converging sliders, the deterioration is less pronounced, since substantial pressure buildup is maintained due to the wedge effect.

4.6. Conclusions

In the present study, the effects of different types of manufacturing errors on the performance of optimally textured parallel and converging thrust bearings has been studied using CFD. Several types of manufacturing errors of the stator surface, including discrepancies in the size and shape of the texture geometry, as well as macroscopic errors in the stator surface (concavity/convexity and waviness), have been accounted for. A wide range of error amplitudes has been considered for each manufacturing error. The effect of the different manufacturing errors on the performance indices of the bearings has been further analyzed by means of pressure and velocity distribution plots. The present results have demonstrated that:

- The effect of manufacturing errors on load capacity and friction coefficient is more pronounced for parallel sliders. In converging sliders, the effect is reduced, since a significant portion of pressure buildup is due to the wedge effect.
- The effect of manufacturing errors on load carrying capacity and friction coefficient decreases with the non-dimensional bearing width, B/L .
- In several cases, the presence of manufacturing errors (e.g. concavity, and single full sine patterned waviness of the stator) results in improved bearing performance, in terms of both load carrying capacity and friction coefficient. The corresponding improvement in load carrying capacity can be of the order of 30% for wavy parallel sliders, and 15% for wavy converging sliders of optimal convergence ratio.
- A small inclination of the dimple legs has only a small effect on the bearing performance indices of parallel bearings; the effect becomes negligible for optimally converging sliders, even for larger inclinations.

The present results can be used as guidelines for prescribing manufacturing tolerances of textured thrust bearings.

5. Conclusions and future study

In the present work, the performance of thrust bearings with artificial surface texturing has been investigated by means of Computational Fluid Dynamics. First, bearings with four different designs (open and closed pocket bearings, taper-land bearings and bearings with rectangular surface texturing) have been studied. It has been demonstrated that, for the range of working parameters considered, open pocket bearings are characterized by superior performance in comparison to all the other bearing designs. Taper-land thrust bearings have also demonstrated very good performance characteristics, whereas textured bearings are characterized by reasonable performance only at low to moderate loads and low values of rotational speed. With reference to manufacturing bearings with these geometries, closed pocket bearings are hard to manufacture, while also not being very attractive in terms of performance. The open pocket bearing geometry is also difficult to manufacture, but this disadvantage is counterbalanced by a superior performance. Based on the present study, parallel textured thrust bearings cannot be characterized as favorable solutions, because of their high manufacturing complexity and poor performance under demanding operating conditions. It must be noted, however, that texturing may aid in improving performance when implemented on a taper-land thrust bearing stator.

The next step of the present study was concerned with the analysis of mechanical deformations of a representative textured thrust bearing. The present results have shown that the effect of oil heating on bearing performance can be substantial. In the fluid-pad interface region, the pad deformation pattern is similar to the pressure distribution. Further, the rotor deformation field is representative of a beam with fixed support. The maximum rotor deformation is substantially higher than that of the pad, and decreases with rotor thickness.

As the performance of thrust bearings may be affected by manufacturing errors, a detailed study has been performed for a representative parallel slider, with a stator textured with periodic grooves of an optimized geometry. The results have shown that the tolerances associated with the dimple or groove geometries are of extreme importance. Furthermore, the effect of manufacturing errors on the performance of thrust bearings has been shown to be influential in a way not easily predicted; although they generally lead to inferior performance, in several cases, a substantial increase in performance has been observed.

Overall, the models developed and utilized in the present work are capable of taking into consideration heat dissipation in the fluid domain, conjugate heat transfer through the bearing solid elements and mechanical deformations. Optimal design parameters of pocket and textured thrust bearing have been identified by detailed parametric studies, whereas the effect of manufacturing errors on bearing performance has been quantified for different values of bearing load and rotational speed.

In order to deepen our understanding on thrust bearing behavior and to further optimize bearing performance, the following subjects of further study are proposed:

- The effect of introducing surface texturing in the forms of pockets or dimples should be investigated for the case of taper-land thrust bearings. An optimization process would be also needed to identify optimal combination of slope and texturing on such bearings.
- Alternative geometries of pocket bearings, characterized by an elliptical front face, converging or diverging side faces and inclination of the bottom surface should be also studied, for identifying optimal design characteristics.
- In the present study, a frozen rotor assumption has been considered for calculating conjugate heat transfer through the rotor. A detailed transient solution of a thrust bearing with a moving rotor is needed to further verify this assumption.
- A two-way FSI model of the thrust bearing should be developed, for predicting the behavior of the bearing at high values of thrust load and rotational speed. Also, this model should be capable of calculating thermal expansion of both the rotor and the stator, which can be of the same magnitude as elastic deformations.
- A 3-D THD parametric analysis regarding the effect of manufacturing errors on industrial bearing designs should be performed, for expanding the findings of the present study.-

6. Literature

- [1] Hamrock, B. J., Schmid, S.R., Jacobson, B.O., *Fundamentals of Fluid Film Lubrication*, 2004.
- [2] Papadopoulos C, Kaiktsis L and Fillon M. CFD thermohydrodynamic analysis of 3-D sector-pad thrust bearings with rectangular dimples. Proceedings of ASME Turbo Expo 2013: Turbine Technical Conference and Exposition, San Antonio, Texas, USA, 3-7 June 2013, paper no. GT2013-94043, pp. 1-10.
- [3] Pascovici M, Cicone T, Fillon M and Dobrica M. Analytical investigation of a partially textured parallel slider. Proceedings of the Institution of Mechanical Engineers, Part J: J. of Engineering Tribology 2009; 223(2): 151-158.
- [4] Papadopoulos C, Efstathiou E, Nikolakopoulos P and Kaiktsis L. Geometry optimization of textured 3-D micro-thrust bearings. Proceedings of ASME Turbo Expo 2011: Turbine Technical Conference and Exposition, Vancouver, Canada, 6-10 June 2011, paper no. GT2011-45822, pp. 1-10.
- [5] Cupillard S, Cervantes M and Glavatskih S. Pressure buildup mechanism in a textured inlet of a hydrodynamic contact. J. of Tribology 2008; 130(2): 21701: 1-10.
- [6] Papadopoulos C, Nikolakopoulos P and Kaiktsis L. Characterization of stiffness and damping in textured sector-pad micro-thrust bearing using computational fluid dynamics. Proceedings of ASME Turbo Expo 2012: Turbine Technical Conference and Exposition, Copenhagen, Denmark, 11-15 June, paper no. GT2012-69403, pp. 1-10.
- [7] Marian V, Kilian M and Scholz W. Theoretical and experimental analysis of a partially textured thrust bearing with square dimples. Proc. IMechE, J. Engineering Tribology 2007; Part J; 221: 771-778.
- [8] Charitopoulos A, Foulis D, Papadopoulos C, Kaiktsis L and Fillon M. Computational investigation of thermoelastohydrodynamic (TEHD) lubrication in a textured sector-pad thrust bearing. 12th EDF/Prime Workshop, Futuroscope, France, 17 & 18 September 2013, pp. 1-10.
- [9] Papadopoulos C, Henry Y, Bouyer J, Kaiktsis L and Fillon M. Sector-pad thrust bearings with rectangular dimples: Comparison between experiments and CFD thermohydrodynamic simulations. World Tribology Congress 2013, Torino, Italy, 8-13 September, pp. 1-4.
- [10] Henry, Y, Bouyer J and Fillon M. Experimental investigation on hydrodynamic parallel surface thrust bearings with textured pads. World Tribology Congress 2013, Torino, Italy, 8-13 September, pp. 1-4.
- [11] Dobrica M, Fillon M, Pascovici M and Cicone T. Optimizing surface texture for hydrodynamic lubricated contact using a mass-conserving numerical approach, J. of Engineering Tribology 2010; 224: 737-750.
- [12] Kazuyuki Y and Joichi S. Balancing wedge action: A contribution of textured surface to hydrodynamic pressure generation. Tribol Lett 2013; 50: 349-364, DOI: 10.1007/s11249-013-0132-z.
- [13] Heinrichson N. On the design of tilting-pad thrust bearings. PhD Thesis, Technical University of Denmark, Lyngby, 2006.
- [14] Brajdic-Mitidieri P, Gosman A, Ioannides E and Spikes H. CFD analysis of a low friction pocketed pad bearing. ASME J. of Tribology 2005; 127: 803-812.
- [15] Etsion, Halperin G, Brizmer V and Kligerman Y. Experimental investigation of laser surface textured parallel thrust bearings. Tribology Letters 2004; 17, No 2: 295-300.
- [16] Etsion I. State of the art in laser surface texturing. Transactions of the ASME, Journal of Tribology 2005; Technology Review, 127: 248-253.
- [17] De Pellegrin D and Hargreaves D. An isoviscous, isothermal model investigating the influence of hydrostatic recesses on a spring-supported tilting pad thrust bearing. Elsevier, Tribology International 51, 2012; 25-35.
- [18] Dobrica M and Fillon M. Thermohydrodynamic behavior of a slider pocket bearing. Transactions of the ASME, J. of Tribology 2006; 128: 312-318.
- [19] Dadouche A, Fillon M and Bligoud JC. Experiments on thermal effects in a hydrodynamic thrust bearing. Tribology International 2000; 33: 167-174.
- [20] Dadouche A, Fillon M and Dmochowski W. Performance of a hydrodynamic fixed geometry thrust bearing: comparison between experimental data and numerical results. Tribology Transactions 2006; 49: 419-426.
- [21] Frene J, Nicolas D, Degueurce B, Berthe D and Godet M. Hydrodynamic Lubrication: Bearings and Thrust Bearings, Elsevier, Amsterdam, 1997.
- [22] Van Ostayen R., Van Beek A. & Munnig-Schmidt R. Film height optimization of hydrodynamic slider bearings. In Proceedings of the ASME/STLE International Joint Tribology Conference, IJTC 2007 PART A, pp. 237-239.

- [23] Buscaglia G, Ausas R & Jai M. Optimization tools in the analysis of micro-textured lubricated devices. *Inverse Problems in Science and Engineering* (2006), 14(4), pp. 365-378.
- [24] Tonder K. Effects of skew unidirectional striated roughness on hydrodynamic lubrication. *Wear* (1987), 115(1-2), pp. 19-30.
- [25] Sharma R & Pandey R. Experimental studies of pressure distributions in finite slider bearing with single continuous surface profiles on the pads. *Tribology International* (2009), Vol.42, no 7, pp. 1040-1045.
- [26] Stephens L, Siripuram R, Hayden M & McCrtt B. Deterministic micro asperities on bearings and seals using a modified LIGA process. *Journal of Engineering for Gas Turbines and Power* (2004), Vol. 126, no 1, pp.147-154.
- [27] Thomsen K & Klit P. Analysis of a thrust bearing with flexible pads and flexible supports. *Proceedings, BALTTTRIB 2007 International Scientific Conference*, pp. 174-180.
- [28] Wang X, Zhu J, Li J, Chen W & Cai L. Numerical analysis of elasto-hydrodynamically lubricated point contacts with three dimensional laser micro-texturing asperity. *International Journal of Nonlinear Sciences and Numerical Simulation* (2007), Vol. 8, no 4, pp. 553-559.
- [29] Rahmani R, Shirvani A & Shirvani H. Optimization of partially textured parallel thrust bearings with square-shaped micro-dimples. *Tribology Transactions* (2007), Vol. 50, no 3, pp. 401-406.
- [30] Neal PB. Heat transfer in pad thrust bearings. *Proceedings of the Institution of Mechanical Engineers* (1982), Vol. 196, pp. 216-28.
- [31] Ahmed S, Fillon M & Maspeyrot P. Influence of pad and runner mechanical deformations on the performance of a hydrodynamic fixed geometry thrust bearing. *Proceedings of IMechE* (2009), Vol. 224 Part J. *Engineering Tribology*, pp. 305-315.
- [32] Brockett S, Barrett L & Allaire E. Thermoelastohydrodynamic analysis of fixed geometry thrust bearings including runner deformation. *Tribology Transactions* (1996), Vol. 39, pp. 555-562.
- [33] Incopera F & De Witt D. *Fundamentals of heat and mass transfer*. 6th Edition, John Wiley & Sons (2006).
- [34] Abramovitz S. Theory for a slider bearing with a convex pad surface; Side flow neglected. *Journal of Franklin Institute* 1955, Vol. 259, No. 3, pp 221-233.
- [35] Andharia, P, Gupta J, Deheri G. On the Shape of the Lubricant Film for the Optimum Performance of a Longitudinal Rough Slider Bearing. *Industrial Lubrication and Tribology 2000*, Vol. 52, No. 6, pp 273-276.
- [36] Bha N, Barrans S, Kumar A. Performance Analysis of Pareto Optimal Bearings Subject to Surface Error Variations. *Tribology International* 2010, Vol. 43, No. 11, pp 2240-2249.
- [37] Buscaglia G, Ciuperca I, Jai M. The Effect of Periodic Textures on the Static Characteristics of Thrust Bearings. *ASME Journal of Tribology* 2005, Vol. 127, pp 899-902.
- [38] Cheng K, Rowe W. A Selection Strategy for the Design of Externally Pressurized Journal Bearings. *Tribology International* 1995, Vol. 28, No. 7, pp 465-474.
- [39] Chen X, He X.. The Effect of Recess Shape on Performance Analysis of the Gas-Lubricated Bearing in Optical Lithography. *Tribology International* 2006, Vol. 39, pp 1336-1341.
- [40] Dobrica M, Fillon M.. About the Validity of Reynolds Equation and Inertia Effects in Textured Sliders of Infinite Width. *Proceedings of the Institution of Mechanical Engineers, Part J: Journal of Engineering Tribology* 2009, Vol. 223, No. 1, pp 69-78.
- [41] Kwan Y, Post J.. A Tolerancing Procedure for Inherently Compensated, Rectangular Aerostatic Thrust Bearings. *Tribology International* 2000, Vol. 33, pp 581-585.
- [42] Li Y, Ding H. Influences of the Geometrical Parameters of Aerostatic Thrust Bearing with Pocketed Orifice-Type Restrictor on its Performance. *Tribology International* 2007, Vol. 40, No.7, pp 1120-1126.
- [43] Ozalp A, Umur H. Optimum Surface Profile Design and Performance Evaluation of Inclined Slider Bearings. *Current Science* 2006, Vol. 90, No. 11, pp 1480-1491.
- [44] Papadopoulos C, Nikolakopoulos P, Kaiktsis L. Evolutionary Optimization of Micro- Thrust Bearings with Periodic Partial Trapezoidal Surface Texturing. *Journal of Engineering for Gas Turbines and Power* 2011, Vol. 133, pp 1-10.
- [45] Papadopoulos C, Efstathiou E, Nikolakopoulos P, Kaiktsis L. Geometry Optimization of Textured 3-D Micro- Thrust Bearings. *Journal of Tribology* 2011, Vol. 133(4), pp 1-14.
- [46] Puri V, Patel C, Bhat, M. The Analysis of a Pivoted Porous Slider Bearing with a Convex Pad Surface. *Wear* 1983, Vol. 88, pp 127-131.
- [47] Ramanaiah G, Sundarammal A. Effect of Bearing Deformation on the Characteristics of a Slider Bearing. *Wear* 1982, Vol. 78, No. 3, pp 273-278.
- [48] Stout K, Pink E. Orifice Compensated EP Gas Bearings: the Significance of Errors of Manufacture. *Tribology International* 1980, Vol.13, No. 3, pp 105-111.

- [49] Yang H, Ratchev S, Turitto M, Segal J. Rapid Manufacturing of Non-Assembly Complex Micro-Devices by Stereolithography. *Tsinghua Science and Technology* 2009, Vol. 14, pp 164-167.